MODELING THE CLIMATE IMPACT OF VOLCANIC ERUPTIONS

by

BRIAN ZAMBRI

A dissertation submitted to the

School of Graduate Studies

Rutgers, The State University of New Jersey

In partial fulfillment of the requirements

For the degree of

Doctor of Philosophy

Graduate Program in Atmospheric Science

Written under the direction of

Alan Robock

And approved by

____

____

____

____

New Brunswick, New Jersey

JANUARY, 2018

ABSTRACT OF THE DISSERTATION

Modeling the Climate Impact of Volcanic Eruptions

By BRIAN ZAMBRI

Dissertation Director:

Alan Robock

Volcanic eruptions can have global climate impacts lasting several years. Large explosive eruptions can inject sulfur gases into the stratosphere, which are converted to sulfate aerosols. These large masses of stratospheric aerosols decrease incoming shortwave solar radiation, resulting in the cooling of the Earth's surface. Sulfate aerosols injected into the tropical stratosphere are transported poleward with a global e-folding lifetime of about one year, meaning climate impacts of large volcanic eruptions can last up to several years. Because of the lack of observations, climate models are heavily relied upon to analyze the climate impact of large, explosive volcanic eruptions.

While current climate models can reasonably reproduce many of the typical climate responses to volcanic eruptions—suppressed precipitation and droughts and surface cooling lasting two to three years—there are other observed responses that are not as well reproduced in climate models. For example, the Northern Hemisphere (NH) winter warming response in the first 1–2 winters after tropical volcanic eruptions, which is well observed, is not captured in most model simulations. The surface winter warming response over NH landmasses is caused by a strengthened polar vortex due to the heating of volcanic aerosols in the tropical stratosphere. A strengthened polar vortex has been

associated with a positive phase of the North Atlantic Oscillation and the Arctic Oscillation, both indices of the wintertime variability of NH sea level pressure. In this thesis, I explore the model response to volcanic eruptions, focusing in particular on the apparent lack of a winter warming response in current climate model simulations. My first step is to examine the winter warming response to tropical volcanic eruptions in the Coupled Model Intercomparison Project 5 (CMIP5) historical simulations. Previous studies have analyzed the response in the historical simulations, but looked at only 13 CMIP5 models and averaged the first two winters, finding little to no response. Here, I analyze all 24 CMIP5 models, include only the two largest eruptions (1883 Krakatau and 1991 Pinatubo), and look at only the first winter after the eruptions.

The CMIP5 historical ensemble has the advantage of a large number of models and a large number of ensemble members for each model. On the other hand, the drawback of analyzing the historical ensemble is that there are only two very large eruptions over the 1850–2005 historical period. Therefore, as a second step, I analyze the winter warming response in the CMIP5/Paleoclimate Model Intercomparison Project 3 past1000 ensemble and the Community Earth System Model (CESM) Last Millennium Ensemble. These experiments, which span 850–1850, are longer than the historical experiment, and therefore have fewer participating models and fewer ensemble members for each model. However, there were many more large volcanic eruptions over the 850–1850 period than in the historical period, which will provide a better look at the winter warming response to large volcanic eruptions.

In contrast to the general winter warming response to tropical volcanic eruptions, I also focus on a specific eruption to which the response has not been well resolved by climate models. The Laki eruption in Iceland, which began in June 1783, was followed by many of the typical climate responses to volcanic eruptions: suppressed precipitation and droughts, crop failure, and surface cooling lasting two to three years. In contrast to the observed cooling in 1784–1786, the summer of 1783 was anomalously warm in western Europe, with July temperatures reaching more than 3 K above the mean in some areas. While climate models can generally reproduce the surface cooling and decreased rainfall associated with volcanic eruptions, model studies have failed to reproduce the extreme warming in western Europe that followed the Laki eruption. As a result of the inability to reproduce the anomalous warming, the question remains as to whether this phenomenon was a response to the eruption, or merely an example of internal climate variability. Using CESM from the National Center for Atmospheric Research, I investigate the role of the aerosol indirect effect of the "Laki haze," and propose a mechanism for its effect on Europe's summer climate. Understanding the cause of this anomaly is important not only for historical purposes, but also for understanding and predicting possible climate responses to future high-latitude volcanic eruptions.

MY CONTRIBUTION TO THE WORK

I wrote three journal articles based on this dissertation work (two published, one in preparation). *Zambri and Robock* [2016] and *Zambri et al.* [2017] focused on the simulated winter warming response and summer monsoon reduction after large tropical volcanic eruptions in state-of-the-art climate models, and *Zambri et al.* [in prep] modeled the climate impacts of the 1783–1784 Laki fissure eruption in Iceland.

Zambri and Robock [2016] analyzed climate model output from the Coupled Model Intercomparison Project 5 (CMIP5) historical ensemble, a model experiment spanning 1850–2005, specifically looking at the simulated winter warming response and summer monsoon reduction after the two largest tropical volcanic eruptions in the historical period. This project was inspired by the consensus that current climate models are in general unable to produce the winter warming response that has been observed after large tropical volcanic eruptions in the real world [*Charlton-Perez et al.*, 2013; *Driscoll et al.*, 2012; *Robock and Mao*, 1992]. I analyzed the results, produced all of the graphics and conclusions, and wrote my first paper [*Zambri and Robock*, 2016]. Dr. Robock was involved in discussing results during the whole project and contributed to editing the manuscript.

My second project was motivated by my first, after noting that there were only two large volcanic eruptions in the 1850–2005 historical period. In contrast, the PMIP3/CMIP5 past1000 ensemble, spanning 850–1850, included many more large volcanic eruptions. Therefore, I did the same type of analysis of winter warming and summer monsoon response as in *Zambri and Robock* [2016] for this model ensemble. I analyzed the results, produced all of the graphics and conclusions, and wrote the manuscript for *Zambri et al.* [2017]. The output analyzed in *Zambri et al.* [2017] included six simulations from the National Aeronautics and Space Administration Goddard Institute for Space Studies E2-R climate model run by physical research scientist Dr. Allegra N. LeGrande. Dr. LeGrande and Dr. Robock also contributed to discussions during the project and to editing the manuscript. Dr. Joanna Slawinska provided post-processed output from the Community Earth System Model Last Millennium Ensemble (CESM-LME) simulations.

The third paper was built on a mutual interest between Dr. Robock and Dr. Anja Schmidt, an interdisciplinary lecturer in climate modeling at the University of Cambridge, in the climate impacts of the 1783–1784 Laki eruption in Iceland. Dr. Schmidt's Ph.D. dissertation focused on the climate impacts of the Laki eruption, including aerosol indirect effects on clouds from the Laki aerosols. However, several phenomena after the Laki eruption still remain unexplained, namely the warm summer in Europe and extremely cold winter in North America. In the summer of 2016, I went to NCAR to learn how to run the CESM. While there, I met with Dr. Schmidt and Dr. Michael Mills, a project scientist at NCAR, to discuss what type of Laki simulations I wanted to do. Dr. Schmidt and Dr. Mills agreed to help me with troubleshooting the model, as they were both experienced using this model. I performed an ensemble of climate model simulations of the Laki eruption, analyzed the output, and wrote the manuscript for *Zambri et al.* [in prep.]. Dr. Mills, Dr. Robock, and Dr. Schmidt, engaged with me in discussion about the results, and contributed to editing the manuscript.

ACKNOWLEDGEMENTS

There are many people at Rutgers to whom I owe thanks for their support and guidance during the past 2+ years. I would first like to thank Alan Robock for teaching me how to be a scientist, and for all of the opportunities that I have been afforded in the process; I am so grateful for having been able to travel to so many new and wonderful places to learn and to present our research over the last few years. I would like to thank him for always being available to answer a question or discuss results, even at times when I had not been as prompt as he would have liked.

I also want to thank the rest of my committee. At Rutgers, Ben Lintner and Tony Broccoli have done more than just advise my research for the dissertation. In our seminar class, Ben taught me how to explain my science to different audiences. In Physical Climatology, Tony taught my classmates and me—several times—about latent and sensible heat. In Boulder, Mike Mills helped me learn to run the model that I used for the last part if my dissertation. Over the last 17 months, Mike has always been available to answer questions about the many problems that I have had running the model.

I cannot forget the rest of our research group at Rutgers. Corey Gabriel showed me how to be a graduate student, specifically at Rutgers and as a part of Alan's group. Lili Xi, the veteran of the group, also helped me run the model when I had trouble. The weekly group meetings helped in so many ways. I learned so much from Corey and Lili, both from their own research and from the conversations that their thoughtful questions about my research so often provoked.

Thanks to my family, for supporting me every step of the way to this PhD. From New York to Los Angeles, back to New York and once more to Los Angeles, and finally

back east (for now), my family has been there through all the bumps—and the jumps—on the way to figuring out what I want to do with my life.

Finally, for my wife Jill, to say thank you would never be enough. She not only supported me during my coast-to-coast search for my calling, but she was by my side the entire way.

This work was supported by National Science Foundation grant AGS-1430051.

TABLE OF CONTENTS

LIST OF TABLES

LIST OF FIGURES

CHAPTER 1: INTRODUCTION

This dissertation consists of three studies with the objective of understanding how large explosive volcanic eruptions affect the climate system, and improving our understanding of the abilities and limitations of current climate models to simulate these effects. The first two studies assess the ability of current climate models to simulate the wintertime dynamical response to large volcanic eruptions; the third study investigates the peculiar climate phenomena surrounding the 1783-1784 Laki volcanic eruption in Iceland. Specifically, this work intends to address the following scientific questions:

1. Can current climate models simulate the observed Northern Hemisphere (NH) warming response in the first winter after large tropical volcanic eruptions?
2. What roles do model resolution and choice of volcanic forcing data set play in the simulated NH winter warming and NH summer monsoon responses?
3. Were the climate changes in Europe in the summer of 1783 and the winter of 1783-84 caused by the Laki eruption, or are they examples of natural climate variability?

1.1 Volcanic eruptions and climate

Volcanic eruptions can have global climate impacts lasting several years. Indeed, large explosive eruptions can inject sulfur gases into the stratosphere, which are then converted to sulfate aerosols over a period of weeks [*Pinto et al.*, 1989; *Zhao et al.*, 1995; *Robock*, 2000]. These large masses of stratospheric aerosols impact both shortwave (SW) and longwave (LW) radiation. The volcanic aerosol cloud decreases direct radiation and increases diffuse radiation as the aerosols scatter incoming SW radiation, with a net decrease in incoming SW radiation resulting in a cooling of Earth's surface [*Robock and*

Mao, 1995; *Robock*, 2000]. Sulfate aerosols created by sulfur injected into the tropical stratosphere, from where they are transported poleward, are more likely to have a long-lasting global climate impact than those originating from high-latitude eruptions, which tend to remain at high- and mid-latitudes [*Kravitz and Robock*, 2011; *Timmreck*, 2012; *Toohey et al.*, 2016]. Other factors that have an influence on the climate response to volcanic eruptions include season of eruption and injection height [*Toohey et al.*, 2011, 2013, 2016].

Because of the changing composition of the stratosphere due to increased anthropogenic emissions of greenhouse gases, aerosols, and ozone-depleting halogens, volcanic aerosols also serve as surfaces for chlorine-liberating chemical reactions that destroy stratospheric ozone [*Solomon*, 1999; *Muthers et al.*, 2014]. This stratospheric ozone depletion also affects the atmospheric dynamic response to volcanic eruptions [*Robock*, 2000; *Stenchikov et al.*, 2002; *Muthers et al.*, 2004]. In the past, when stratospheric chlorine levels were lower, the heterogeneous deactivation reactions of nitrogen oxides (NOx) on sulfate aerosols surfaces had the opposite effect, instead slowing down NOx-induced ozone depletion [*Tie and Brasseur*, 1995; *Solomon et al.*, 1996]. Sulfate aerosols act as a component to facilitate heterogeneous reactions, which deactivate nitrogen oxides, but in turn activate halogens, leading to a significant reduction of the ozone concentrations [*Solomon*, 1999; *Rozanov et al.*, 2002].

There are a number of reasons why a better understanding of the impacts of volcanic eruptions is so important. Accurate assessment of the cooling effect of volcanic eruptions over the past century is important for the attribution of the warming of the past century to anthropogenic greenhouse gases [*Robock*, 2000]. Understanding the indirect impacts of volcanic eruptions on atmospheric and oceanic circulation will help to make better seasonal forecasts after the next large eruption. The impacts of volcanic eruptions serve as analogs to nuclear winter and geoengineering [*Robock et al.*, 2008].

1.2 Indices of past volcanism

To evaluate the causes of climate change during the past century and a half of instrumental records or during the past 1000 years, a reliable record of the volcanic aerosol loading of the atmosphere is necessary. Many indices have been compiled, based on different data sources and criteria. Here, I summarize the different indices that were used as model input for the CMIP5/PMIP3 simulations [*Taylor et al.*, 2012]. Combinations of surface, aircraft, balloon, and satellite measurements have helped to quantify the optical properties, distribution, and transport of the aerosols from the 1982 El Chichón [*Robock*, 1983] and 1991 Pinatubo [*Stenchikov et al.*, 1998] eruptions [*Robock*, 2000]. Even observations of the most recent large eruptions, though, are imperfect [*Stenchikov et al.*, 1998]. For example, *Stenchikov et al.* [1998] reported that observations at latitudes 20°S-20°N, the latitudes of maximum concentration for the Pinatubo aerosol cloud, were limited due to sparse lidar data at these latitudes and saturation of SAGE II measurements in the first months after the eruption.

For the CMIP5 historical experiment of the last 150 years, modeling groups—who commonly represent aerosols in four latitude bands [*Marshall et al.*, 2009]—used volcanic input data from *Sato et al.* [1993], *Stenchikov et al.* [1998], *Ammann et al.* [2003], and *Ammann et al.* [2007]. *Sato et al.* [1993] derived a data set of aerosol optical depths (AOD) for the period 1850-1990 based on different types of data from four different periods. Due to a lack of measurements of optical extinction for 1850-1882, *Sato et al.* [1993] made estimates of AOD for this period based on a scaling of the volume of ejecta from *Mitchell* [1970], and assumed a globally uniform AOD for this period. For the period 1883-1978, the data are based on measurements of atmospheric optical extinction. Because all of the measurements before 1960 are from the NH, Southern Hemisphere (SH) optical depths are inferred based on the latitudes of the volcanoes for 1883-1959. For example, the 1883 Krakatau eruption occurred near the equator, so equal AODs were assumed for both the NH and SH. With the launch of instruments like Stratospheric Aerosol Monitor (SAM) II in 1978 [*McCormick et al.*, 1979] and Stratospheric Aerosol and Gas Experiment (SAGE) I and II in 1979, *Sato et al.* [1993] were able to use satellite data to provide more accurate estimates for El Chichón and Pinatubo.

Stenchikov et al. [1998], pointing out that microphysical parameters like aerosol size distribution and composition define aerosol spectral optical properties, developed a more detailed set of aerosol parameters for the 1991 Pinatubo eruption. Using as input retrievals of optical depth and effective radius from SAGE II and Upper Atmosphere Research Satellite [UARS; *Lambert et al.*, 1997], respectively, they calculated a spectral-, space-, and time-dependent data set including aerosol extinction, single-scatter albedo, and asymmetry parameter. While *Stenchikov et al.* [1998] focused on the microphysical properties of the aerosols, *Ammann et al.* [2003, 2007] instead fixed the particle size distribution and used the Department of Energy Parallel Climate Model [*Washington et al.*, 2000] to model the spread of volcanic aerosols, taking into account the seasonal changes in stratospheric transport. This resulted in a monthly-varying data set with 64 latitude bands, a much higher meridional resolution than in *Sato et al.* [1993].

Another issue with all the indices is missing volcanoes, which is increasingly important further back in time [*Robock*, 2000]. Volcanoes only appear in most of the indices if the eruption is identified by a report from the ground. For this reason, all the indices may miss some SH eruptions. As recently as December 1981, the eruption of Nyamuragira was observed with lidar but the aerosol cloud was reported as the "mystery cloud" until the source was identified several years later [*Krueger et al*., 1996; *Robock*, 2000]. Before the beginning of satellite and lidar records in 1978, there may be important missing eruptions. This problem does not exist for individual ice core records, because they are objective measures of volcanic sulfuric acid. The problem, however, with ice cores is that fewer records exist for periods farther back in time, and each ice core record is extremely noisy and may have other problems [*Robock*, 2000].

Robock and Free [1995] discussed a number of issues in using ice cores as measures of volcanic aerosol loading. Ice core records are sometimes base on acidity, yet not all acidity maxima are necessarily volcanic signals. Anthropogenic emission of sulfate can lead to a higher background sulfate concentration in some cores, adding noise and making the signal extraction process more difficult. Several issues arise with regard to the timing of the deposit, including accuracy of dating and duration of eruption. Eruptions close to the ice sheet that deposit sulfate through transport in the troposphere can be sources of false volcanic signals. The irregularity of aerosol transport in the stratosphere related to the timing, latitude, and injection height of the eruption will change how much sulfate is deposited for a given sulfur mass erupted. The stochastic nature of snowfall and dry deposition, the processes by which sulfate aerosols reach the surface, can lead to low correlation between ice cores in nearby regions. Mixing due to blowing snow is yet another source of noise in the ice cores. Testing for acidity in ice cores using the electrical conductivity method is sensitive to temperature, which is another potential source of measurement error.

Still, ice core reconstructions have been vital tools for recording volcanism in the distant past [*Gao et al.*, 2008; *Crowley et al.*, 2008; *Sigl et al.*, 2015]. The two ice core reconstructions used for the CMIP5/PMIP3 past1000 [*Braconnot et al.*, 2012] and CESM-LME [*Otto-Bliesner et al.*, 2016] experiments were *Gao et al.* [2008] and *Crowley et al.* [2008]. *Gao et al.* [2008] constructed the Ice-core Volcanic Index 2 (IVI2) using 36 ice cores from Greenland and Antarctica. To convert from ice core deposition to stratospheric sulfate loading, *Gao et al.* [2008] used calibration factors that were calculated from radioactive deposition from nuclear bomb tests, satellite observations of Pinatubo aerosol loading, and model simulations of volcanic sulfate transport and deposit from various large eruptions [*Gao et al.*, 2007]. Then, stratospheric sulfate injections were converted to a volcanic forcing index using a modified stratospheric transport parameterization [*Grieser and Shönwiese*, 1999] combined with a function to describe the sedimentation and formation of aerosols [*Gao et al.*, 2008]. Vertical aerosol distributions were interpolated based on lidar measurements after the 1991 Pinatubo eruption [*Antuña et al.*, 2002]. The time evolution of the volcanic aerosols begins with a linear buildup of the total aerosol mass for 4 months after an eruption, followed by an exponential decrease of the stratospheric aerosol mass with a global mean e-folding time of 12 months [*Gao et* *al.*, 2008]. The IVI2 forcing assumes a linear relationship between total stratospheric aerosol load and global AOD.

Crowley et al. [2008] based their reconstruction on 13 cores from both Greenland and Antarctica, and their methods are described in *Crowley and Unterman* [2013]. They calibrated mean sulfate deposition values by scaling against AOD measurements after the Pinatubo eruption [*Sato et al.*, 1993]. Using a method similar to *Gao et al.* [2008], *Crowley et al.* [2008] assume a linear increase in AOD for five months, plateau for three months, and decrease with an e-folding lifetime of 1 year for tropical eruptions. *Crowley et al.* [2008] provide an estimate of AOD from a 2/3-power scaling for eruptions larger than the 1991 Pinatubo eruption, which leads to larger eruptions having smaller climate impacts in this data set than in *Gao et al.* [2008] [*Crowley and Unterman,* 2013; *Metzner et al.*, 2014].

1.3 Winter warming after tropical volcanic eruptions

In addition to reflecting incoming solar radiation, sulfate aerosols absorb solar near-infrared and terrestrial infrared radiation, warming the stratosphere [e.g., *Lacis et al.*, 1992; *Stenchikov et al.*, 1998]. In the 2 years after the 1982 El Chichón and 1991 Pinatubo eruption the globally averaged stratospheric temperature rose by about 1 K and 2 K, respectively [*Robock*, 2000]. For tropical volcanic eruptions, this infrared forcing leads to an anomalously warm equatorial lower stratosphere, increasing the equator-to-pole temperature gradient. Volcanic aerosols are also associated with polar stratospheric ozone loss by activation of halogens, which results in a cooling of the polar stratosphere, further increasing the gradient [*Solomon*, 1999; *Stenchikov et al.*, 2002; *Muthers et al.*, 2014; *Barnes et al.*, 2016]. By the thermal wind relation, the anomalous temperature gradient results in stronger westerly winds in the stratosphere.

It is unclear, however, what contribution the enhanced temperature gradient from heating by volcanic aerosols makes to the strengthened stratospheric polar vortex at 60°N [*Stenchikov et al.*, 2002; *Toohey et al.*, 2014; *Bittner et al.*, 2016b]. *Stenchikov et al.* [2002] turned off direct heating of volcanic aerosols in a climate model simulation using the Geophysical Fluid Dynamics Laboratory (GFDL) SKYHI model [*Fels et al.*, 1980]. They found that, with volcanic aerosols cooling the surface but not heating the stratosphere, SKYHI still simulated winter warming over Eurasia and North America. They instead proposed that maximum surface cooling in the tropics weakens the meridional temperature gradient in the troposphere, leading to a decrease in upward planetary wave flux and causing a strengthened polar vortex. In contrast to this theory, though, observations of the 1963 Agung, 1982 El Chichón, and 1991 Pinatubo eruptions show an increased wave flux after large volcanic eruptions [*Graf et al.*, 2007]. Consistent with *Graf et al.* [2007], using the Max Planck Institute Earth System Model [MPI-ESM; *Giorgetta et al.*, 2013] *Toohey et al.* [2014] found increased upward planetary wave activity in the mid and high latitudes, which weakens the polar vortex. Recently, modeling studies have resulted in newly proposed mechanisms for the strengthened polar vortex, including increased stratospheric residual circulation and southward deflection of planetary waves [*Toohey et al.*, 2014, *Bittner et al.*, 2016b].

Despite the uncertainty with regard to the mechanism, the strengthened polar vortex leads to positive temperature anomalies over northern Eurasia and sometimes parts of North America, a response known as “winter warming” [*Robock and Mao*, 1992;

Perlwitz and Graf, 1995]. Significant cooling has also been observed in the Middle East [*Robock*, 2000]. Though *Groisman* [1985] identified winter warming in Russia after large volcanic eruptions, *Robock and Mao* [1992] were the first to examine the full NH winter surface temperature patterns. They averaged the first or second winter—depending on the latitude of the eruption—of the 12 largest volcanoes since 1883, and found significant surface warming over Eurasia and parts of North America, with significant cooling in the Middle East [*Robock and Mao*, 1992].

Perlwitz and Graf [1995] and *Kodera et al.* [1996], among others, have associated a strong polar vortex with a positive phase of the North Atlantic Oscillation—an index of the wintertime variability of north-south Northern Hemisphere sea-level pressure gradients between 110°W and 70°E [*Hurrell*, 1995; *Christiansen*, 2008]—or the Arctic Oscillation (AO), the first empirical orthogonal function of NH winter monthly sea level pressure anomalies [*Thompson and Wallace*, 1998]. A positive AO corresponds to anomalously low pressure over the pole, and anomalously high pressure at midlatitudes, with the anomalies changing signs in the negative phase. After large volcanic eruptions a positive phase of the AO has been observed for the following 1 to 2 winters [*Robock and Mao*, 1992; *Stenchikov et al.*, 2002; *Shindell et al.*, 2004].

1.4 Modeling the winter warming response

Multiple early modeling studies reported moderate success in simulating the atmospheric dynamical response to volcanic eruptions [*Graf et al.*, 1993; *Kirchner et al.*, 1999; *Kirchner and Graf,* 1995; *Rozanov*, 2002; *Shindell et al.*, 2001; *Stenchikov et al.*, 2002]. *Graf et al.* [1993] and *Kirchner and Graf* [1995] used the MPI ECHAM2 model in a perpetual-January experiment, and reported a strengthened polar vortex and surface warming similar in structure to the observed response to the 1991 Pinatubo eruption. *Kirchner et al.* [1999] used the updated ECHAM4 with a data ocean, based on climatological, El Niño, and La Niña SSTs, and found a surface winter warming pattern very similar, both in pattern and magnitude, to observations and reanalysis after the Pinatubo eruption, with significant warming over North America and Eurasia and significant cooling over the Middle East. *Stenchikov et al.* [2002] found a strengthened polar vortex and surface warming with the GFDL SKYHI model, and even found a winter warming response to volcanic surface cooling without stratospheric heating.

In contrast to these early results, *Stenchikov et al.* [2006], *Driscoll et al.* [2012], and *Charlton-Perez et al.* [2013] showed that CMIP3 and CMIP5 models produced imperfect simulations of the surface winter warming response to large volcanic eruptions when examining an average of the first two NH winters following tropical volcanic eruptions. *Stenchikov et al.* [2006] analyzed the AO response to the nine largest volcanic eruptions from 1880 to 2000 between 40°S and 40°N in seven CMIP3 models. Only two of seven models simulated significant warming over Eurasia, and while five of the seven models simulated a stronger-than-normal polar vortex, the anomalies were much smaller than those observed. *Driscoll et al.* [2012] performed a similar analysis, this time with output from 13 CMIP5 models, and using the same nine volcanic eruptions. Results were similar, with the CMIP5 models producing only a slightly strengthened stratospheric vortex, and failing to reproduce observed NH winter temperature responses following volcanic eruptions.

The perceived inability of climate models to produce this dynamical response in past studies has been attributed to several weaknesses in the models, including a simplified treatment of volcanic aerosols and deficiencies in model implementation of the Brewer-Dobson circulation [*Stenchikov et al.*, 2006; *Marshall et al.*, 2009; *Thomas et al.*, 2009; *Driscoll et al.*, 2012]. It has been suggested that the stratosphere must be reasonably well-resolved in order for a model to respond to volcanic forcing in a realistic manner, but *Charlton-Perez et al.* [2013] also showed that results in CMIP5 models remained largely unchanged whether considering low-top or high-top models. A lack of ozone chemistry in the models has also been thought to contribute to the lack of a dynamical response, though some debate exists with respect to the importance of ozone depletion for the surface winter warming response [*Stenchikov et al.*, 2002; *Marshall et al.*, 2009]. Still, others have suggested that the models are unable to produce an AO response to large-scale forcing [*Otterå*, 2008; *Driscoll et al.*, 2012], though *Stenchikov et al.* [2004], *Shindell et al.* [2004] and *Bittner et al.* [2016a] showed that this might not be the case.

In contrast to *Driscoll et al.* [2012], through analysis of zonal wind anomalies *Barnes et al.* [2016] and *Bittner et al.* [2016a] found a strengthened polar vortex in the first winter after the largest eruptions in the CMIP5 historical simulations. In addition, previous studies have suggested that the simulated response does not depend on the chosen volcanic forcing data set [*Driscoll et al.*, 2012; *Maher et al.*, 2015]. On the other hand, others argue that the choice of volcanic forcing can significantly impact model responses [*Schmidt et al.,* 2011; *Toohey et al.*, 2014].

1.5 Summer monsoon reduction after tropical volcanic eruptions

In addition to the surface warming response caused by changes in stratospheric temperature and density gradients, circulation changes caused by atmospheric injection of sulfate aerosols by large volcanic eruptions are thought to reduce summer precipitation in Northern Africa and Asia [e.g., *Rotstayn and Lohmann*, 2002; *Oman et al.*, 2006; *Iles and Hegerl*, 2015; *Colose et al.*, 2016; *Liu et al.*, 2016]. This is caused by a weakening of the Indian and African monsoon due to inhomogeneous cooling of the land and ocean, which decreases the temperature gradient between Europe and Asia and the Pacific and Indian Oceans [*Colose et al.*, 2016; *Iles and Hegerl*, 2015; *Liu et al.*, 2011; *Man et al.*, 2012, 2014; *Man and Zhou*, 2014; *Oman et al.*, 2006].

After a large, explosive volcanic eruption, the decrease in radiation at the surface cools land preferentially to the ocean. This causes a reduction in land-ocean temperature gradients between Europe and Asia and the Pacific and Indian Oceans, thereby decreasing monsoon circulation. Historical accounts and previous studies support the idea that large tropical eruptions reduce summer precipitation in northern Africa and Asia and may tend to strengthen droughts in the region [*Oman et al.*, 2006; *Iles and Hegerl*, 2014; *Liu et al.*, 2016]. For example, the lowest rainfall in the Sahel region of Africa over 1940-1990 occurred in the summers directly following the 1982 El Chichón eruption, suggesting that large tropical eruptions may tend to strengthen droughts in the region [*Robock and Liu,* 1994]. Similar drought conditions were reported across India in the summer after the 1783-1784 Laki eruption in Iceland [*Mooley and Pant*, 1981].

Several modeling studies concluded that tropical volcanic eruptions reduce precipitation in NH summer, specifically in the African and Asian monsoon regions

[*Colose et al.*, 2016; *Iles and Hegerl*, 2015; *Liu et al.*, 2011; *Man et al.*, 2012, 2014; *Man and Zhou*, 2014]. *Liu et al.* [2011] found reductions in both subtropical and extratropical East Asian summer monsoon (EASM) rainfall in response to volcanic forcing. This response is distinct from the natural, unforced state, in which the subtropical and extratropical rains vary with opposite signs. *Man et al.* [2012] found a stronger EASM during the Little Ice Age (LIA) than during the Medieval Warm Period in MPI-ESM simulations. They attributed the weaker monsoon during the LIA to the land-sea thermal contrast change, which was forced by volcanic cooling. Similar results were found in *Man et al.* [2014] for the Agung, El Chichón and Pinatubo eruptions, and by *Man and Zhou* [2014] using output from a FGOALS-gl model simulation of the last millennium. In addition, *Colose et al.* [2016] showed that the Goddard Institute for Space Studies Model E2-R (GISS-E2-R) past1000 and CESM-LME ensembles show a general decrease in tropical precipitation after tropical volcanic eruptions.

1.6 Climate impacts of the 1783-1784 Laki eruption in Iceland

High latitude eruptions have a more limited impact on global climate than tropical eruptions of the same size, because the atmospheric circulation causes the aerosol plume to remain in the hemisphere in which the eruption occurs [e.g., *Kravitz and Robock*, 2011]. One high-latitude eruption that is often studied is the 1783-1784 Laki eruption in Iceland, which was unique in that it injected sulfur gas into the lower troposphere as well as into the lower stratosphere [*Highwood and Stevenson*, 2003; *Oman et al.*, 2005, 2006; *Kravitz and Robock*, 2011; *Schmidt et al.*, 2012; *Pausata et al.*, 2015a, 2015b, 2016]. In addition to a constant effusing of gas in the troposphere from June 8, 1783 to February 7, 1784, Laki was characterized by 10 approximately El Chichón-sized eruptions which injected sulfur gas into the lower stratosphere from 9-13 km [*Thordarson and Self*, 2003].

In addition to its unique eruption type, Laki was followed by abrupt and unique regional climate change in the years following. The eruption was followed by an extremely warm summer in Europe, an extremely cold winter in most of the Northern Hemisphere [*Luterbacher et al.*, 2004; *Schmidt et al.*, 2012; *Thordarson and Self*, 2003], and extreme drought, crop failure, and famine in Africa and Asia for several years [*Finnsson*, 1796; *Oman et al.*, 2006; *Wood*, 1992]. While surface cooling and reductions of tropical precipitation are expected impacts of a volcanic eruption and have been reproduced by model studies in the past [e.g., *Oman et al.*, 2006; *Schmidt et al.*, 2012], the European heat wave in July 1783 and the cold winter of 1783-1784 have yet to be explained or reproduced. Discussion remains as to whether the anomalously warm temperatures were due to greenhouse warming by sulfur gases in the troposphere that made their way to Europe from Iceland, or if the warming was merely an example of climate variability [*Thordarson and Self*, 2003]. In addition, *D'Arrigo et al.* [2011] argue that natural variability in the form of a concurrent El Niño and negative phase of the North Atlantic Oscillation (NAO), and not the Laki eruption, was responsible for the extremely cold winter of 1783. However, *Pausata et al.* [2015a, 2016] demonstrated that large, high-latitude eruptions can increase the likelihood of an El Niño in the first year after the eruption.

1.7 Do volcanic eruptions cause El Niños?

The impact of volcanic eruptions on the El Niño-Southern Oscillation (ENSO) has been investigated at length, with mixed results. Some studies found a connection between volcanic eruptions and ENSO events [e.g., *Adams et al.*, 2003; *Mann et al.*, 2005; *McGregor and Timmerman*, 2011; *Wahl et al.*, 2014], while others found little to no correlation [*Robock et al.*, 1995; *Self et al.*, 1997; *Ding et al.*, 2014]. *Adams et al.* [2003] found a preferred multi-year El Niño-like response in the first 3 years after tropical eruptions, with a reversal to La Niña-like conditions in years 4-6, with the El Niño response the stronger of the two. *Mann et al.* [2005] used the Zebiak-Cane model of the coupled tropical Pacific and found that occurrence of an El Niño after a large tropical volcanic eruption is approximately twice as likely as with normal conditions. On the other hand, *McGregor and Timmerman* [2011] used the NCAR Community Climate System Model, version 3 (CCSM3) and found a significant increase in the likelihood of a La Niña event in the year after an eruption. *Wahl et al.* [2014] found an increase in the likelihood of both positive and negative ENSO events in the first year after a volcanic eruption, depending on the set of eruptions chosen. In contrast to these results, *Robock et al.* [2015] used a modified version of NCAR Community Climate Model 1 to conclude that the El Niño after the 1982 El Chichón was not forced by the eruption, and that the concurrence of the two was rather coincidence. Similarly, *Self et al.* [1997] asserted that the timing of the Krakatau, El Chichón, and Pinatubo eruptions and the concurrent El Niños implies at most an amplification response to volcanic aerosols, but not a direct cause-and-effect relationship. *Ding et al.* [2014] found no link between volcanic forcing and ENSO amplitude in CMIP5 models.

More recently, studies have demonstrated more conclusive results. *Maher et al.* [2015] found in CMIP5 models an increased likelihood of an El Niño event in the first

NH winter after an eruption with a corresponding increase in the probability of a La Niña event in the third post-eruption winter. *Predybaylo et al.* [2017] also found an increased probability of an El Niño in the first year after the eruption with a dependence on the initial condition of ENSO. Specifically, they found a strengthening of El Niño in neutral conditions, a lengthening of central Pacific El Niños, a weakening of Eastern Pacific El Niños, and no effect on La Niña conditions. *Stevenson et al.* [2016] found a tendency toward El Niño in the second winter after tropical eruptions, with a dependence on seasonality of the eruption [*Stevenson et al.*, 2017]. On the other hand, *Le* [2017] found a negative ENSO response after volcanic eruptions in simulations of the last millennium. *Khodri et al.* [2017] showed that tropical volcanic eruptions trigger El Niños through a weakening of the West African monsoon and the resulting atmospheric Kelvin wave, which drive equatorial westerly wind anomalies in the western Pacific.

Pausata et al. [2015a, 2016], using the Norwegian Earth System Model 1 [NorESM1-M; *Bentsen et al.*, 2013], found that NH high-latitude eruptions increase the likelihood of an El Niño. They hypothesized that the southward shift of the Inter-Tropical Convergence Zone (ITCZ) due to preferential cooling in the NH [*Colose et al.*, 2016] generates anomalous westerly winds at the surface of the central and western equatorial Pacific and equatorial northerlies in the eastern pacific, priming the Pacific Ocean for an El Niño-like perturbation [*Pausata et al.*, 2015a]. *Pausata et al.* [2016] examined the role of initial conditions, and found that the largest anomalies are simulated after an eruption that occurs during a developing La Niña or ENSO-neutral conditions. They attribute this result to the fact that the ITCZ is farther north and the equatorial trade winds stronger in La Niña and neutral conditions than in El Niño conditions.

1.8 Summary of dissertation work

To evaluate the winter warming response in the first winter after large tropical volcanic eruptions in current climate models, I examined model output from the CMIP5 historical experiment. I analyzed anomalies in surface air temperature, sea level pressure, and 50 hPa geopotential height in the NH winter (December-January-February, DJF) after the two largest tropical eruptions in the 1850-2005 historical period: Krakatau in 1883 and Pinatubo in 1991. This work has already been completed and reported in *Zambri and Robock* [2016], and I summarize it here. I found that climate models in the CMIP5 ensemble are capable of producing circulation changes consistent with a positive AO and winter warming temperature responses for large enough eruptions. I also found that the models are capable of reproducing the weakening of the summer monsoon that has been observed after large tropical volcanic eruptions. Not all of the CMIP5 models produced a good winter warming or summer monsoon response following the 1883 Krakatau and 1991 Pinatubo eruptions, but 16 of them did. Including seven other, smaller tropical eruptions, I found a similar but dampened response.

There are only two large eruptions in the historical period. Therefore, I also analyzed model simulations from 850-1850 CE, a period that contains 10 eruptions as large or larger than Pinatubo. This work has also been completed and reported in *Zambri et al.* [2017], and I summarize it here. I analyzed reflected SW radiation, 50 hPa heating anomalies, surface temperature, zonal-mean zonal wind, sea level pressure, and geopotential height in the NH winter after the eruptions, and precipitation in the NH summer after the eruptions for the CMIP5/PMIP3 past1000 experiment and for the

CESM-LME. I found here again that most models do produce a significant winter warming response, and that the response depends on the choice of volcanic forcing data set.

Finally, I conducted an ensemble of simulations with the CESM Whole Atmosphere Community Climate Model (WACCM), in order to assess the role of the Laki eruption in the anomalous European summer and winter of 1783. WACCM includes fully interactive stratospheric chemistry and includes aerosol indirect effects. By choosing initial conditions similar to synoptic observations in June 1783, I conducted a 40-member ensemble of model simulations with and without the Laki eruption, in order to determine whether the warm summer of 1783 and extremely cold winter of 1783-1784 was an effect of the Laki eruption or just an example of natural climate variability. Results indicate that the warm summer was, in fact, climate variability, rather than a Laki impact. Simulations with the eruption show significant cooling over Europe, while most of the eruptions without the eruption do show significant positive temperature anomalies over Europe. Some ensemble members with the eruption even show a warm-but-cooled anomaly, in very good agreement with observations. Results from the winter after Laki are less conclusive. It has been proposed that the cold winter was caused by a concurrent negative phase of the NAO and El Niño. The model simulations do show that the volcanic eruption increases the probability of an El Niño in the winter after the eruption. On the other hand, it is not apparent that the eruption has any significant effect on the winter circulation in the NH high latitudes.

CHAPTER 2: WINTER WARMING AND SUMMER MONSOON REDUCTION IN THE CMIP5 HISTORICAL ENSEMBLE

2.1 Methods

The model runs analyzed here are from the historical simulations (1850-2005) of CMIP5. Unlike some of the other external forcings (e.g., solar, greenhouse gases), which were standardized for the experiments, one of five volcanic forcing data sets—*Ammann et al.* [2003, 2007], *Sato et al.* [1993], *Stenchikov et al.* [1998], or *Andres and Kasgnoc* [1998]—was used by each modeling group. The volcanic forcing data set used by each model is given in Table 2.1.

I chose to restrict analysis to those CMIP5 models that have at least two ensemble members for the historical experiment, and which had a realistic treatment of volcanic aerosols, that is, I excluded models which reduced the solar constant to achieve the radiative forcing associated with the eruption. Of the 22 models satisfying these requirements, I also discarded the 2 models (~10% of the set) with the lowest wintertime variability in 50 hPa geopotential height and zonal wind, as these models would not be expected to be able to produce an adequate response to the volcanic forcing. All available ensemble members were used for each model, with a total of 20 models and 122 ensemble members. Individual model means were calculated before the multi-model mean, so that all models were given equal weight. Table 1 lists the models and some details regarding each model.

In previous studies, the nine largest volcanic eruptions between 40°N and 40°S over 1883 to 2005 were analyzed [*Stenchikov et al.*, 2006; *Driscoll et al.*, 2012]; here I restricted my analysis to the two largest eruptions over that same latitude band and time frame, similarly to *Bittner et al.* [2016a]. I analyze surface air temperature, zonal mean zonal wind, geopotential height, and mean sea level pressure for the first NH winter (DJF) and precipitation for the first NH summer (June-July-August; JJA) after the two largest eruptions between 40°S and 40°N in the 1850-2005 CE historical period. I have therefore analyzed the first winters and summers after the 1883 Krakatau and 1991 Pinatubo eruptions, with the exception of geopotential height, for which I have analyzed the 1982 El Chichón eruption in place of the Krakatau eruption. This distinction is made because of the choice of reanalysis data sets discussed below. See Table 2 for a brief description of the three volcanic eruptions considered.

In addition to the low number of observed volcanic eruptions considered here, high variability during NH winter and influence by other natural factors such as El Niño and the Quasi-Biennial Oscillation (QBO) all contribute to a highly noisy volcanic signal with regard to the observations. However, the point of restricting the analysis to the two strongest volcanic eruptions, as was done by *Bittner et al.* [2016a], is to examine whether including smaller eruptions in past studies has had the effect of masking the ability of CMIP5 models to reproduce this NH winter dynamical response to tropical volcanic eruptions. In addition, previous studies have examined the role of El Niño in the winter warming response as well as including observations of several more eruptions [*Robock and Mao*, 1992; *Stenchikov et al.*, 2006; *Driscoll et al.*, 2012]; while including more eruptions helps to average out some of the climate variability—resulting in an average response that is lower in amplitude—the spatial pattern of the response remains largely unchanged. Therefore, for the sake of consistency with the model analysis, I present the observations for the same two volcanic eruptions in each case.

For surface air temperature, mean sea level pressure, and precipitation, the reanalysis of the 20th Century version 2 (20CRv2) [*Compo et al.*, 2011] is used for comparison with observations. In addition, and because of the high uncertainty in the 20CRv2 reconstructions of upper air fields [*Compo et al.*, 2011], the ERA40 [*Uppala et al.*, 2005] reanalysis fields are used to compare with lower stratosphere circulation changes during the winter season after the El Chichón and Pinatubo eruptions, as in *Driscoll et al.* [2012].

Previous studies have averaged the first two post-volcanic winters and have used different lengths of reference periods for each eruption [*Stenchikov et al.*, 2006; *Driscoll et al.*, 2012]. Here, post-volcanic seasonal anomalies are calculated by subtracting the first NH winter (DJF) and summer (JJA) after each eruption from the same seasonal mean of the five years before the eruption. The statistical significance of anomalies for individual model means and observations is evaluated with a bootstrapping method. Specifically, for each model, and for the reanalysis data, I computed 5000 synthetic anomalies for each ensemble member. I calculated the ensemble mean of each of the 5000 synthetic data sets, and the 90% confidence interval for each model response is given by the 5% to 95% range of the 5000 synthetic means. Of course, statistical significance does not imply physical significance, i.e., high variability at high latitudes could cause a large anomaly to be considered insignificant, while low variability in the tropics could result in a small anomaly being significant there. For multi-model means, I quantify the level of model agreement in the sign of the response. Assessing the multi-model mean response in this manner may prevent one from discarding a small magnitude response that is robust in that all of the simulations agree on the sign of the response, as well as highlighting large responses that may be dominated by only a few models [*Barnes et al.*, 2016]. I define a significant response as one where at least 15 of the 20 models agree on the sign of the response. If the data were purely random, agreement in the sign of the response by least 15 of the 20 would be expected 4.1% of the time, similar to a 95% confidence limit.

2.2 Results

2.2.1 Surface Temperature

Figure 1 shows the composite of DJF surface temperature anomalies after the eruptions. The reanalysis (Figure 2.1a) shows the well-documented significant surface warming signal over northern Europe and Asia, where anomalies are almost everywhere above 2 K. Significant cooling is also observed over Northern Africa and the Middle East. The results here are based on only two post-volcanic winters and so natural climate variability will contribute to the observed response. However, previous observational studies including more eruptions have shown that this response is typical for large tropical eruptions [e.g., *Robock and Mao*, 1992]. Consistent with *Stenchikov et al.* [2006] and *Driscoll et al.* [2012], there is a warming signal in the Eastern Pacific. This, along with at least some of the warming over North America, can be attributed to the fact that both eruptions were at the same time as an El Niño, and the models should therefore in general not be expected to show the same pattern in these regions. The positive anomaly in the Arctic region appears unusually large, but the reliability of temperature at high latitudes is low, so the anomaly in this region might not be considered highly significant [*Compo et al.*, 2011].

Though lower in magnitude and not reaching as far south, the multi-model mean of surface temperature does show significant warming over northern Eurasia, in agreement with observations (Figure 2.1b). This, in addition to the significant cooling over northern Africa and the Middle East, can be seen as a robust dynamical response to a large tropical volcanic eruption. Figure 2.1b shows the average response over all models, and Figure 2.2 shows the composites of surface temperature for the first post-volcanic winter for the individual models. As should be expected, there is plenty of variability between the models in their NH response. However, the observed warming in northern Eurasia is simulated by most of the models, though it is in general weaker and over smaller areas than in the observations. Some of the models, on the other hand (ACCESS1-3, CESM1-FASTCHEM, NorESM1-M) show warming only in a small region, with a general cooling in the Asian-European area. Most of the models show significant cooling in the tropical latitudes, and all models but CESM1-CAM5 show significant cooling in both Northern Africa and the Middle East, in agreement with the observations.

The analysis of surface temperature in the CMIP5 ensemble shows a better correspondence with observations during the first NH winter following large tropical eruptions than has been found previously by including smaller eruptions and averaging two winters [*Stenchikov et al.*, 2006; *Driscoll et al.*, 2012]. Figure 2.3 shows that there is good model agreement in the tropics (cooling) and over Northern Eurasia (warming). A significant improvement is seen–in comparison to the findings of *Stenchikov et al.* [2006] and *Driscoll et al.* [2012]—in the models' ability to produce surface warming over Eurasia and cooling over the Middle East. These improvements can be attributed to the difference in how the analysis was done, especially since *Driscoll et al.* [2012] used the same CMIP5 historical runs and many of the same participating models.

2.2.2 Mean Sea-Level Pressure

The reanalysis shows significant negative anomalies in the mean sea-level pressure over the Arctic region and significant positive anomalies over the North Atlantic (Figure 2.4a). This pattern suggests that the observed surface temperature anomalies are related to changes in the winter circulation caused by the volcanic eruptions. These sea-level pressure anomalies are consistent with a positive phase of the NAO, and are in agreement with previous studies [*Stenchikov et al.*, 2006, *Driscoll et al.*, 2012].

The multi-model composite of mean sea-level pressure (Figure 2.4b) shows a similar pattern to the observations, with somewhat significant negative anomalies over the Arctic and more positive anomalies equatorward. On the other hand, the anomalies are of lesser magnitude, and the strong positive anomaly seen over the North Atlantic is not captured in the model mean. Instead, the maximum positive anomaly in the multi-model mean is shifted over Europe. While some models are able to produce the observed positive NAO-like pattern (CanESM2, GFDL-CM3, HadCM3, GISS-E2-H, NorESM1-M), Figure 2.3 shows much disagreement in the sign of the anomalies, and Figure 2.5 shows large differences in sea-level pressure patterns between models. Indeed, many of the models do produce a dipole, though several (e.g., bcc-csm1-1, MPI-ESM-MR, CNRM-CM5), have the maximum positive anomaly shifted over Europe, as shown in the multi-model mean. Still, others show anomaly patterns of opposite sign to the observations (CCSM4, CESM1-FASTCHEM).

2.2.3 Geopotential Height

Geopotential height anomalies in the stratosphere help define circulation changes during winters following large volcanic eruptions. Due to the high uncertainty in the 20CRv2 reconstructions of upper air fields for the pre-radiosonde era, I analyze here the El Chichón and Pinatubo eruptions using the ERA40 data set. In observations the anomaly pattern in the stratosphere shows a cold and deep polar night vortex, as observed in the 50 hPa geopotential height anomalies (Figure 2.6a) showing a large statistically significant decrease in geopotential height over the pole and over Northern Europe, with positive anomalies observed at lower latitudes. This has previously been attributed to the direct heating of the lower tropical stratosphere by the volcanic aerosols [*Stenchikov et al.*, 1998; *Ramachandran et al.*, 2000]. The observed negative anomaly in 50 hPa geopotential height at high latitudes points to a colder lower stratosphere near the pole, which suggests a stronger and persistent polar vortex [*Driscoll et al.*, 2012]. Previous studies also suggest that this might be a characteristic of the early stage of the post-volcanic winter season [*Graf et al.*, 2007; *Mitchell et al.*, 2011].

The multi-model mean 50 hPa geopotential height anomalies (Figure 2.6b) show a similar strengthening of the polar vortex, with a significant positive anomaly moving equatorward, though the magnitude of these anomalies is in some areas different from those in the observations. Most of the models show the same general pattern observed in the stratosphere (see Figure 2.7) as in the reanalysis, though the magnitude of the responses varies considerably. In particular, the maximum observed increase in geopotential height is over North America (Figure 2.6a), while the maximum positive anomalies are shifted toward the Pacific Ocean in many of the models (Figures 2.6b, 2.7).

In addition, while most models show the positive change in geopotential height in the tropics and midlatitudes, some models fail to reproduce the strong negative anomalies in the lower polar stratosphere. ACCESS1-3, CESM1-CAM5, CESM1-FASTCHEM, bcc-csm1-1, MPI-ESM-MR show good spatial agreement with the reanalysis, with anomalies in ACCESS1-3 and the CESM1 models reaching above 100 m in the tropics and midlatitudes and below -100 m at the pole. NorESM1-M also shows similar patterns, though the vortex is centered over Northern Europe and North America/Greenland, respectively. GFDL-CM3 shows almost no change in circulation with regard to the 50 hPa geopotential height, and both IPSL models, which were excluded because of not using aerosol forcing, show the opposite pattern, with positive anomalies near the pole and negative anomalies equatorward. However, the GFDL-CM3 and IPSL-CM5A-MR did produce strong winter warming patterns (Figure 2.2), showing that it is possible to get that pattern without stratospheric forcing, as was found for an older GFDL model [*Stenchikov et al.*, 2002]. The relative strength of these different mechanisms will be studied in Tier 1 simulations of the upcoming Volcanic Model Intercomparison Project [VolMIP; *Zanchettin et al.*, 2016], but is beyond the scope of the present work.

2.2.4. Summer Monsoon Reduction

Circulation changes and indirect effects of sulfate aerosols due to large volcanic eruptions are thought to reduce summer precipitation in Northern Africa and Asia [*Rotstayn and Lohmann*, 2002; *Oman et al.*, 2006; *Iles and Hegerl*, 2014]. *Robock and Liu* [1994] pointed out that the Sahel region had its lowest rainfall over 1940-1990 in the summers directly following the 1982 El Chichón eruption, suggesting that large tropical eruptions may tend to strengthen droughts in the region. Observations of summer precipitation after the 1883 Krakatau and 1991 Pinatubo eruptions are consistent with these findings, showing a significant reduction in summer precipitation over the Sahel region and over the Maritime Continent, with anomalies below -2 mm/day in some areas (Figure 2.8a). On the other hand, observations show a significant increase in precipitation over parts of India, though historical accounts and previous studies show that volcanic eruptions have been associated with droughts in the region [*Mooley and Pant*, 1981; *Oman et al.*, 2006]. The multi-model mean (Figure 2.8b) shows drying in all three regions mentioned, agreeing with previous studies and not the observations with regard to changes in rainfall over India. Negative anomalies are significant over India and in some areas over the Maritime Continent and the Sahel.

Over the period 1851-2012, the mean tropical (30°S-30°N) JJA precipitation in the 20CRv2 reanalysis is 3.6 mm/day with a standard deviation of 2.0 mm/day, about 56% of the mean. Due to this high variance in precipitation, high variability between models is shown in Figures 2.3d and 2.9. Most of the models show significant drying over the Sahel region, though GISS-E2-H, NorESM1-M, CESM1-CAM5, and CESM1-FASTCHEM show more positive anomalies than negative there. MPI-ESM-MR and GISS-E2-H are the only models that do not show significant drying over India; MPI-ESM-MR has India wetter during the post-volcanic summers, while GISS-E2-H shows no change in precipitation.

2.3 Discussion and conclusions

Previous studies have concluded that current global climate models do a poor job of reproducing circulation changes and the associated NH warming response during winters after large tropical volcanic eruptions [*Stenchikov et al.*, 2006, *Driscoll et al.*, 2012; *Charlton-Perez et al.*, 2013]. These studies, however, calculated anomalies by calculating the average of the first two post-volcanic winters while—on the average—one would expect winter warming to last only the first winter after the eruption for large tropical eruptions [*Robock and Mao*, 1992]. More recently, however, *Bittner et al.* [2016a] obtained more positive results by using different methods of analysis than those shared by the previous studies. By considering only the first winter after the eruptions, and by considering only the two largest eruptions, I have shown that climate models in the CMIP5 ensemble are capable of producing these circulation changes and temperature responses for large enough eruptions, in agreement with *Bittner et al.* [2016a], who found that the mean of 15 CMIP5 models did simulate a positive AO in the first NH winter after the 1883 Krakatau and 1991 Pinatubo eruptions. I also did my analysis with all nine larger tropical eruptions over the historical period and found similar, but damped responses (see Figure 2.10). Consistent with the results of *Bittner et al.* [2016a], the volcanic signal is somewhat lost when smaller eruptions are considered.

CanESM2 simulates the climate that is most comparable to the observed winter warming response, doing a fairly good job of reproducing changes in surface temperature, sea-level pressure, and circulation. bcc-csm1-1 and CESM1-FASTCHEM both show a realistic warming pattern and a strong polar vortex through 50 hPa geopotential height changes, but fail to produce the positive phase of the NAO as illustrated by changes in sea-level pressure. GFDL-CM3 is in good agreement with observations in both temperature and sea-level pressure, but shows very little change in 50 hPa geopotential height.

Not all of the CMIP5 models produced a good winter warming or summer monsoon response following the 1883 Krakatau and 1991 Pinatubo eruptions, but 16 of them did. They are indicated in Table 2.1, and the patterns they produced, which are stronger than those shown here, are shown in Fig. 2.11. As has been pointed out in previous studies [*Driscoll et al.*, 2012; *Maher et al.*, 2015], in addition to different forcing data sets, some of the models differ in their implementation of volcanic forcing. However, these differences do not have an impact on the overall results. Indeed, I examined the differences in forcing, model resolution, model top, and their ability to simulate AO, and could not find any criteria that would allow us to determine a priori which models did a good simulation. Of course, it may have been by chance because of the small number of ensemble members.

CHAPTER 3: WINTER WARMING AND SUMMER MONSOON REDUCTION IN THE PMIP3/CMIP5 PAST1000 ENSEMBLE

3.1 Methods

Bittner et al. [2016a] and *Zambri and Robock* [2016] were able to isolate the surface winter warming and summer monsoon signals by looking at only large (at least as large as 1991 Pinatubo) tropical volcanic eruptions. However, since 1850 there have only been two such eruptions, 1883 Krakatau and 1991 Pinatubo. Here I look at the previous 1000 years and were able to use 10 large volcanic eruptions, so as to extract a clearer signal of the volcanic response for the first winter and summer after large eruptions. I restrict my analysis to eruptions between 40°S and 40°N. I examine the PMIP3 last millennium (past1000) simulations and the CESM-LME for 850 to 1850. The past1000 simulations include six simulations of the GISS-E2-R climate model and single simulations from eight additional modeling groups (Table 3.1). For the LME I consider a 14-member ensemble, including five runs with volcanic forcing only. Here I will describe the methods used to address this research question, which is answered in *Zambri et al.* [2017].

After excluding one additional available model simulation which reduced the solar constant to achieve the radiative forcing associated with volcanic eruptions, I analyzed a total of 28 simulations of the period 850-1850 CE. This includes 14 simulations from the PMIP3 past1000 experiment and 14 from the LME. Six of the 14 past1000 simulations come from the same model, GISS-E2-R, and so I analyze these runs separately. Furthermore, I separate simulations by the volcanic data set by which they were forced. Specifically, of the eight non-GISS past1000 simulations, four used the *Gao* *et al.* [2008] (GRA) forcing data set, while the other four used the *Crowley et al.* [2008] (CEA) forcing. Of the six GISS-E2-R simulations, three were forced with about twice the prescribed forcing from the GRA data and three with the CEA forcing. Aside from the GRA forcing being doubled in the GISS-E2-R simulations, the two volcanic forcing data sets also differ in their conversion from sulfate ice core concentrations to aerosol optical depth. The GRA forcing assumes a linear relationship between total stratospheric aerosol load and global AOD, while CEA provide an estimate of AOD from a 2/3-power scaling for eruptions larger than the 1991 Pinatubo eruption [*Crowley and Unterman,* 2013; *Metzner et al.*, 2014]. The GISS simulations also presume the same relationship between AOD and effective radius as in *Sato et al.* [1993], making the aerosol particle sizes proportionally larger for the larger eruptions. In addition, MRI-CGCM3 interactively computes the conversion from SO_2 injection to stratospheric aerosols; this is the only model of the set that uses an interactive scheme. Different events are captured in the two data sets, and common events often have different amplitudes based on the different methods of conversion [*Sigl et al.*, 2014]. Thus, I analyze the GRA-forced and CEA-forced simulations separately. All 14 of the CESM-LME simulations used the GRA forcing. Nine of the simulations included all forcings, while the remaining five included only volcanic forcing. I analyze the all-forcing and the volcano-only runs separately. Although five of the six ensembles include all forcings, while the last includes volcanic forcing only, other forcings (e.g., greenhouse gases, ozone, tropospheric aerosols) were set to pre-industrial levels, and therefore should not have an impact on the results. Therefore, it is valid to compare the volcano-only simulations with those simulations that have all forcings implemented. Only MIROC-ESM includes an internally-generated

QBO. More information about the individual models can be found in Table 3.1.

I analyze surface air temperature, zonal mean zonal wind, geopotential height, and mean sea level pressure for the first NH winter (DJF) and precipitation for the first NH summer (JJA) after the ten largest eruptions between 40°S and 40°N in the 850-1850 C.E. period. While there are common events, there are some events that are captured in one forcing data set but not in the other. Therefore, the 10 volcanic eruptions analyzed are not the same for each set of simulations. The eruptions, the years and latitudes of eruption, the stratospheric sulfate aerosol mass [*Gao et al.*, 2008], and the forcing data set where each eruption appears are listed in Table 3.2. The choice of restricting analysis to eruptions in the 40°S-40°N band is made because high-latitude eruptions should not in general be expected to produce a positive AO and the associated NH surface warming response [e.g., *Oman et al.*, 2005]. Anomalies are calculated by subtracting the average of the five winters (for surface temperature, zonal mean zonal wind, sea level pressure, and geopotential height) or summers (for precipitation) before each eruption from the first winter or summer after the eruption. Because of the close proximity of the 1809 and 1815 eruptions, I use the same reference period (1804-1808) for these two eruptions. I assess the statistical significance of anomalies at the 95% level using a local two-tailed Student's t-test, assuming for the multi-model means that each volcano and each model realization represent independent samples.

In addition, I test whether looking at the principal modes of variability yields a response similar to those delivered from the aforementioned analyses. Specifically, the AO index is computed for each ensemble member of each model, and model responses are compared using a superposed epoch analysis of the winter AO for the 10 volcanic eruptions listed in Table 3.2.

3.2 Results

3.2.1 Radiative Effects

I follow the convention of previous studies of using the time series of the anomalies in the top-of-atmosphere (TOA) reflected SW radiation (Figure 3.1) as a rough proxy for the global radiative effect of the volcanic aerosols [*Stenchikov et al.*, 2006; *Driscoll et al.*, 2012]. All of the models perform reasonably consistently with each other and reveal an increase in the reflected SW radiation corresponding to the explosive volcanic eruptions, though some noticeable differences do exist. Differences in reflected SW radiation are more dependent on model choice than on the choice of volcanic forcing. Specifically, the GISS-CEA ensemble simulates larger anomalies in reflected SW radiation than the PMIP-CEA ensemble, and the CESM-LME ensemble simulates larger anomalies than the PMIP-GRA ensemble. On the other hand, for most of the common events (e.g., 1260, 1284, 1809, 1815) the GRA and CEA forcings elicit similar responses in the CESM-LME and GISS-CEA ensembles. As should be expected, the largest anomalies overall are produced by the 2xGRA GISS-E2-R ensemble. Reflected SW radiation anomalies for this ensemble are approximately 4 times larger than the anomalies in the other single-model ensembles, and these anomalies are scaled by a factor of 0.25 in Figure 3.1 for comparison with the other ensembles.

In contrast to the radiative cooling demonstrated by anomalies in TOA reflected SW radiation, I measured the anomalous heating forced by the volcanic aerosols in the lower stratosphere by analyzing the anomalies in the de-trended 30°S-30°N, 50 hPa temperature. Figure 3.2 shows that unlike the radiative cooling, which exhibited higher dependence on the model, the variability in stratospheric temperature due to volcanic eruptions is more strongly influenced by the forcing data set chosen. Specifically, the GRA-forced ensembles show significantly larger heating anomalies than the CEA-forced ensembles, including for common events. In this case, the CESM-LME ensembles simulate the largest heating anomalies of the singly-forced ensembles. The 2xGRA GISS-E2-R temperature anomalies are approximately one to two times as large as the other GRA-forced ensembles, depending on the eruption, and anomalies for this ensemble are scaled by a factor of 0.5 in Figure 3.2. The results in this section indicate that one might expect the weakest surface winter warming response from the CEA-forced ensembles, as the magnitude of lower stratospheric heating in these simulations is affected by the aforementioned 2/3-power scaling.

3.2.2 Surface Temperature

Figure 3.3 illustrates the surface air temperature anomalies for the first DJF winter after the 10 volcanic eruptions. The CEA-forced PMIP multi-model average (Figure 3.3a) shows very little warming over northern Eurasia, with anomalies below 0.5 K. On the other hand, the GRA-forced PMIP multi-model average does simulate significant warming in this region (Figure 3.3b). In this case, the maximum anomaly is above 1.5 K in northern Europe. The CEA-forced GISS-E2-R runs (Figure 3.3c) simulate mostly cooling in the NH, with some warming (anomalies less than 1 K and not statistically significant) over northern Europe and Asia. The 2xGRA forcing runs (Figure 3.3d) simulate significant warming over most of northern Eurasia and northeastern North

America, with anomalies almost uniformly above 2 K and reaching above 4 K. All of the models show cooling over northern Africa, the Middle East, and the tropics, with anomalies generally being greater in magnitude in the GRA-forced runs. The all-forcing CESM runs reveal significant warming over almost all of northern Europe and Asia, with the maximum anomaly above 2 K (Figure 3.3e); similar results are seen in the volcano-only runs (Figure 3.3f). One feature that is unique to the CESM ensemble is warming in the Weddell Sea.

Figure 3.4 illustrates the individual PMIP model mean responses in the first winter after the eruption. HadCM3 shows warming over eastern Eurasia, although there is also warming over Greenland, which should not in general be expected. MIROC-ESM reveals no warming over Europe, and only a small patch of warming in southeast Asia. BCC-CSM1-1, MPI-ESM-P, CCSM4, FGOALS-s2, and MRI-CGCM3 all simulate surface winter warming, though only anomalies in MRI-CGCM3 are significant. The lack of statistical significance is due to a combination of a low number of years averaged for each model (10) and the high variability of NH winter [*Bittner et al.*, 2016a]. Still, most of the models do simulate surface winter warming over Europe, with several models simulating anomalies above 2 K. Figures 3.5 and 3.6 show surface temperature anomalies for the second winter after the eruptions. While surface cooling from the eruptions is still evident, only the doubly-forced GISS-E2-R runs (Figure 3.6d) and MRI-CGCM3 (Figure 3.7, bottom right), which uses an interactive aerosol scheme, displays significant surface winter warming for two years after the eruption.

In addition to the warming response over NH landmasses, the impact of volcanic eruptions on the El Niño Southern Oscillation (ENSO) has been investigated at length, with mixed results. Some studies found a connection between volcanic eruptions and ENSO events [*Mann et al.*, 2005; *McGregor and Timmerman*, 2011; *Wahl et al.*, 2014; *Maher et al.*, 2015; *Stevenson et al.*, 2016, 2017; *Le*, 2017; *Predybaylo et al.*, 2017], while others found little or no correlation [*Robock et al.*, 1995; *Self et al.*, 1997; *Ding et al.*, 2014]. Figure 3.3 and the first four panels in Figure 3.4 show very little ENSO activity in the first two post-volcanic winters, with very little, mostly insignificant, temperature changes in the tropical Pacific. Only in Figures 3.5e-f does significant warming over the tropical Pacific Ocean indicate an increased likelihood of the formation of an El Niño after a volcanic eruption. However, this El Niño-like signal is observed only in the second winter and only in the CESM-LME ensembles, in agreement with *Stevenson et al.* [2016]. These results are evidence of the model dependence of this phenomenon, which is further supported by the aforementioned studies, each of which used a different set of models.

3.2.3 Zonal Wind

Strengthened zonal winds in the midlatitude stratosphere result in a stronger polar vortex, a dynamical response that has been observed after volcanic eruptions in the past [e.g., *Graf et al.*, 2007]. This strengthened polar vortex drives the surface winter warming response, and for this reason I first analyze the zonal wind anomalies in the different sets of experiments, as one may not expect a response at the surface if the zonal winds are not significantly strengthened. Figure 3.7 shows the winter zonal mean zonal wind responses to the selected 10 large volcanic eruptions.

Though all ensembles exhibit significantly strengthened westerlies at 60°N, the anomalies vary considerably in magnitude and spatial extent. Specifically, the PMIP

CEA-forced multi-model mean (Figure 3.7a) and the CEA-forced GISS-E2-R ensemble (Figure 3.7c) simulate the weakest anomalies, with a maximum strengthening of less than 5 m/s in Figure 3.7a and less than 3 m/s in Figure 3.c. On the other hand, all of the other analyses (Figures 3.7b, 3.7d-f) show stronger anomalies similar to those simulated in previous studies [e.g., *Bittner et al.*, 2016a], that is, these simulations reveal significantly strengthened westerlies in the polar lower stratosphere, with the anomalies changing signs at lower latitudes and altitudes. The PMIP GRA-forced runs (Figure 3.7b) reach a maximum strengthening above 5 m/s around 60°N in the polar stratosphere, and significant westerly wind anomalies extend down to about 200 hPa. Anomalies in the polar region reach a maximum of 17 m/s and extend to the surface in the 2xGRA-forced GISS simulations (Figure 3.7d). This extreme case may be expected because of the doubled forcing, but the contrast between Figures 3.7a and 3.7b and between Figures 3.7c and 3.7d show that the choice of forcing data set can significantly impact the ability of a model to produce a strengthened polar vortex in response to a low-latitude volcanic eruption, in agreement with past studies [*Toohey et al.*, 2014; *Bittner et al.*, 2016b]. The ensemble means of the CESM simulations produce almost identical results, both in spatial pattern and magnitude of anomalies. The maximum anomaly is 7 m/s in the polar stratosphere, and the westerly wind anomalies reach about 300 hPa for the all-forcing average (Figure 3.7e) and 500 hPa for the volcano-only average (Figure 3.7f).

Of course, variability between models also plays a role in the differences seen in Figures 3.7a and 3.7b. For this reason, I present in Figure 3.8 the results for the individual models that make up the two PMIP ensembles. Of the eight models, all but CSIRO-Mk3L-1-2 and BCC-CSM1-1 display significantly strengthened zonal winds in the stratosphere near 60°N. CSIRO-Mk3L-1-2 is the coarsest model, with only 18 vertical levels, which surely contributes to the lack of a response. However, BCC-CSM1-1 has a vertical and horizontal resolution similar to many of the models that do simulate strengthened westerly winds after the eruption. MIROC-ESM and MRI-CGCM3 models, which have the highest vertical resolutions, simulate the largest anomalies in zonal wind. MPI-ESM-P, CCSM4, HadCM3, and FGOALS-s2 also produce strengthened westerlies. Figure 3.8 illustrates that, on the average, the two ensembles simulate similar responses; the difference in magnitude of response in Figures 3.7a-b is due to the exceedingly strong response from MRI-CGCM3. In addition, while the models with the highest resolutions do simulate the strongest responses, models with similar resolutions yield markedly different responses. Similar to the surface response, MRI-CGCM3, which handles aerosols interactively, shows the strongest response.

Uncertainty in the model results is due to several sources: forcing uncertainty, differences in forcing and model physics, model uncertainty, and internal variability [*Toohey et al.*, 2014; *Bittner et al.*, 2016a]. The different responses between Figures 3.7a and 16b and between Figures 3.7c and 3.7d are examples of several of these uncertainties. Specifically, Figures 3.7c and 3.7d are results from different forcings in the same model, while Figures 3.7a and 3.7b are results from different forcings in different models. To further explore model dependence, Figure 3.9 shows the DJF zonal mean zonal wind for the period 850-1850 for the CEA-forced PMIP models, the GRA-forced PMIP models, GISS-E2-R, and CESM. Comparison of the zonal winds from the different models illustrates that the CEA-forced PMIP models (Figure 3.9a) and GISS-E2-R (Figure 3.9c) exhibit weaker mean zonal winds north of 60°N in the stratosphere than do the other models. Results from the individual models (Figure 3.10) are consistent with this analysis in that the CEA-forced models tend to have weaker zonal wind climatologies than the GRA-forced models. This can to some extent explain why two of the ensembles are unable to sufficiently represent zonal wind anomalies in response to stratospheric heating due to volcanic aerosols, and why GISS-E2-R requires a very strong forcing to simulate a significant response. However, two of the CEA-forced PMIP models, MIROC-ESM, MPI-ESM-P, which simulate zonal wind climatologies closest to the reanalysis, do simulate substantial changes in zonal wind in response to the volcanic eruptions, as illustrated in Figure 3.8. In addition, BCC-CSM1-1, which simulates one of the strongest NH winter zonal wind climatologies, exhibits no changes in the polar stratosphere in response to volcanic eruptions. Therefore, the extent to which weaker mean winds can explain the discrepancy in the response between models is limited.

3.2.4 Geopotential Height

Several mechanisms have been proposed for the dynamical response that causes a stronger polar vortex after low-latitude volcanic eruptions [*Stenchikov et al.*, 2002; *Driscoll et al.*, 2012; *Toohey et al.*, 2014; *Bittner et al.*, 2016b]. This strengthened and persisting polar vortex can be observed in the 50 hPa geopotential height field, and is characterized by negative anomalies near the pole and positive anomalies toward the equator. Figure 3.11 depicts the 50 hPa geopotential height anomalies for the first winter after the 10 largest eruptions in the six ensembles. Similarly to the results in section 3.2.3, all ensembles reveal a strengthened polar vortex, but with anomalies of varying magnitudes. The CEA-forced PMIP runs simulate a strengthened polar vortex with significant negative anomalies near the pole (Figure 3.11a). The maximum positive and negative anomalies are above 80 m and below -80 m, respectively. The individual PMIP model results (Figure 3.12) demonstrate that this apparently insignificant anomaly is affected by a disproportionately weak response from a single model (CSIRO-Mk3L-1-2). Indeed, three of the four CEA-forced PMIP models do produce a significantly strengthened polar vortex. The CEA-forced GISS ensemble (Figure 3.11c) exhibits significant positive anomalies associated with warming by sulfate aerosols. On the other hand, the negative anomalies at the pole are not significant and are almost everywhere above -30 m. The GRA-forced ensembles simulate a much stronger polar vortex, with anomalies exceeding 100 m in the absolute value covering most of the NH (Figure 3.11b, 3.11d-f). Individual model results for the GRA-forced PMIP runs (Figure 3.12) are similar to those for the CEA-forced models; three of the four models (CCSM4, FGOALS-s2, MRI-CGCM3) simulate a significantly strengthened polar vortex, while only one model (BCC-CSM1-1) reveals no significant changes. The significant negative anomalies at the pole are in contrast with previous studies, which showed that models could simulate the increase in geopotential height at lower latitudes but largely failed to simulate the deep polar vortex after large tropical volcanic eruptions [*Stenchikov et al.*, 2006; *Driscoll et al.*, 2012; *Charlton-Perez et al.*, 2013; *Toohey et al.*, 2014; *Zambri and Robock*, 2016].

3.2.5 Sea Level Pressure

A strengthened polar vortex has been associated with a positive phase of the AO [*Baldwin and Dunkerton*, 2001; *Gerber et al.*, 2012], the first empirical orthogonal function (EOF) of NH winter monthly sea level pressure anomalies, and a positive phase of the AO has been observed for 1 to 2 winters following large tropical volcanic eruptions [*Robock and Mao*, 1992; *Thompson and Wallace*, 1998; *Stenchikov et al.*, 2002; *Christiansen*, 2008]. Consistent with observations of recent large tropical volcanic eruptions, all six data sets simulate low pressure over the pole and high pressure at midlatitudes, though only the 2xGRA GISS and the two CESM-LME ensembles simulate a statistically significant positive phase of the AO. The CEA-forced PMIP runs show small changes in sea level pressure consistent with a positive phase of the AO, with a maximum high-pressure anomaly of 2 hPa in the north Pacific and minimum low-pressure anomaly of -2 hPa over the pole (Figure 3.13a). However, the weak anomalies are not statistically significant, and therefore do not indicate a robust tendency toward a positive AO in these models. The individual model responses (Figure 3.14) further illustrate the difference in responses in the stratosphere and at the surface. Specifically, in contrast to zonal mean zonal wind and geopotential height anomalies, only one of the four CEA-forced PMIP models (MPI-ESM-P) simulates a pattern of sea level pressure anomalies in line with a positive AO, with anomalies above 2 hPa in the absolute value.

The GRA-forced PMIP runs exhibit a more well-defined AO pattern, with positive anomalies spanning the mid-latitudes, and significant negative anomalies below -2 hPa near the pole (Figure 3.13b). Figure 3.14 further illustrates that three of the four GRA-forced PMIP models (CCSM4, FGOALS-s2, MRI-CGCM3) do show a tendency toward a positive AO in the winter after a large eruption, though only CCSM4 and MRI-CGCM3 simulate a strong enough response for anomalies to be considered statistically significant and overcome the high variability of the winter season. The CEA-forced GISS runs (Figure 3.13c) show a tendency toward a positive AO, with significant positive anomalies over Eurasia and the North Atlantic, but the low-pressure anomalies over the pole are weak and not significant, and high pressure is not simulated over North America. The 2xGRA forcing GISS runs (Figure 3.13d) simulate a strong positive AO the first winter after the eruptions, with significant negative pressure anomalies below -6 hPa over the pole, and anomalously high pressure at mid-latitudes, especially over the North Atlantic region. The CESM ensembles exhibit similar patterns, with significant anomalies below -2 hPa at the pole and above 2 hPa at mid-latitudes, specifically over the north Pacific (Figures 3.13e-f). One notable difference between these results is that the anomalies over the north Atlantic in the all-forcing ensemble are comparatively weaker than those in the volcano-only ensemble.

I also computed the AO index, whose signature over the Atlantic is similar to that of the NAO [*Hurrell*, 1995]. The AO index is computed for each ensemble member of each model. I first compute the first EOF of the monthly winter (DJF) mean sea level pressure anomalies north of 20°N for the period 850-1850. Each data point is weighted by the square root of the grid area it represents, consistent with *Christiansen* [2008] and *Driscoll et al.* [2012]. The seasonal winter (DJF) AO index is computed from the monthly indices, defined as the principal component of the monthly anomalies of sea level pressure projected onto the first EOF and normalized to unit variance. The EOF pattern for each model is shown in Figure 3.15.

I compare the model responses using a superposed epoch analysis of the winter AO for the 10 volcanic eruptions listed in Table 3.2. I take the winters in the ten years neighboring the first winter before each eruption (five years before and five years after) as defined in Table 3.2 and generate an "eruption matrix" whose rows represent each eruption event. The rows are then averaged to obtain the epoch composite of 11 years, from winter in year -5 to winter in year +5 with year 1 the first winter after an eruption. The statistical significance of the epoch analysis is estimated using a bootstrap method, by which I generate a "random eruption matrix" by reshuffling with replacement the elements of each row and average the rows into a new epoch composite. The procedure is repeated 5,000 times obtaining a distribution of AO values for each lag of the epoch composite. I compare the level of the AO index for each year of the composite with the 5%– 95% and 1%– 99% percentile levels of the bootstrap distribution.

Figure 3.16 illustrates the results of the superposed epoch analysis. Among the 6 ensembles analyzed in this study, a positive AO signal at lag 1 is observed for all ensembles but the CEA-forced GISS-E2-R ensemble (Figure 3.16c). However, only PMIP-GRA (Figure 3.16b), GISS-E2-R 2xGRA (Figure 3.16d), and CESM-LME (Figure 3.16e) reveal a statistically significant positive AO at lag 1. Indeed, the observed positive AO at lag 1 in Figures 3.16a and 3.16f may be spurious, since the CEA-forced PMIP runs produce a significant positive AO at lag -2 (Figure 3.16a) and the CESM-LME Volc ensemble yields a significant positive AO at lag 4. In fact, three of the six ensembles show a statistically significant positive AO at lag 4; this, too, appears to be deceptive since none of the eruptions were separated by fewer than 6 years.

3.2.6 Summer Monsoon

After a large, explosive volcanic eruption, the decrease in radiation at the surface cools land preferentially to the ocean. This causes a reduction in land-ocean temperature gradients, thereby decreasing monsoon circulation [e.g., *Man et al.*, 2012, 2014; *Man and Zhou*, 2014]. Most of these models were evaluated by *Tilmes et al.* [2013], who found that they do a good job of simulating the current regional monsoon systems. Historical accounts and previous studies support the idea that large tropical eruptions reduce summer precipitation in northern Africa and Asia and may tend to strengthen droughts in the region [*Oman et al.*, 2006; *Iles and Hegerl*, 2014]. In addition, *Colose et al.* [2016] showed that the GRA-forced GISS-E2-R and CESM ensembles simulate a significant decrease in tropical precipitation after tropical volcanic eruptions.

Figure 3.17 illustrates the global precipitation responses in the first summer (JJA) after the selected volcanic eruptions. The CEA-forced PMIP runs simulate reductions below -0.5 mm/d over Africa, but the response over Asia is less homogeneous, with both positive and negative anomalies occurring there (Figure 3.17a). In contrast, there are significant reductions in precipitation below -1 mm/d over much of Asia in the GRA-forced PMIP ensemble (Figure 3.17b). In agreement with Figure 3.17a, the GRA-forced runs reveal a similar reduction of precipitation over the Sahel region of Africa, though anomalies in this case are significant and generally larger in magnitude. The CEA forced GISS-E2-R runs (Figure 3.17c) exhibit reductions in precipitation the Sahel and monsoon Asia, but the anomalies tend to be non-uniform and less than 0.5 mm/day in these regions. On the other hand, the 2xGRA forced GISS-E2-R runs (Figure 3.17d) simulate significant reductions of rainfall over the Sahel region, India, and most of the Western Pacific Ocean—including much of the maritime continent—with anomalies below -2 mm/day in all three regions. The CESM ensembles (Figures 3.17e, f) indicate reductions in tropical precipitation similar to those in the GRA-forced PMIP ensemble. Specifically, both Figure 3.17e and 3.17f exhibit significant reductions in precipitation over much of South and East Asia. Significant reductions are also simulated in the Sahel region of Africa, with reductions below -1 mm/d in much of the region.

Five of the eight PMIP model means (Figure 3.18) exhibit significant reductions in precipitation over the Sahel region; MIROC-ESM, CSIRO-Mk3L-1-2, and BCC-CSM1-1 do not reveal significant changes, with anomalies both positive and negative there. Responses in Asia are less homogeneous, though all models but MIROC-ESM and CSIRO-Mk3L-1-2 simulate significant reductions in precipitation over parts of India and China.

The results presented here are consistent with previous studies that show reductions in tropical precipitation for the first two boreal summers after large volcanic eruptions [*Iles and Hegerl*, 2014, 2015; *Colose et al.*, 2016; *Liu et al.*, 2016] and, more specifically, reductions in precipitation in the East Asian monsoon region after large volcanic eruptions [*Liu et al.*, 2011; *Man et al.*, 2012, 2014; *Man and Zhou*, 2014]. Composite results for the second post-eruption summer (not shown) are similar to Figure 3.17, except that several of the ensembles show a change in the sign of precipitation anomalies over the Sahel.

3.3 Discussion and conclusions

The CESM-LME runs clearly simulate a significantly strengthened polar vortex and a positive AO, both in the all-forcing runs and the volcano-only runs. The GISS-E2-R model produces intense and significant surface winter warming and summer monsoon reduction after volcanic eruptions with the 2xGRA forcing, but produces a much weaker and mostly insignificant signal with the CEA forcing. While a large response might be expected due to the large forcing, this analysis demonstrates that differences between forcing data sets play a large role in the model response to volcanic eruptions, which is in agreement with past studies [*Toohey et al.*, 2014; *Bittner et al.*, 2016b]. Similarly to the

GISS-E2-R ensembles, the model responses vary greatly between the CEA-forced and GRA-forced PMIP3 ensembles. While this can certainly be attributed in part to the different forcing data sets used, analysis of the individual model results illustrate that differences between models also have a large influence. For example, the weakest response in all fields was simulated by CSIRO-Mk3L-1-2, a CEA-forced model. However, this is also the model with the lowest horizontal and vertical resolution of all models analyzed (Table 3.1). On the other hand, the largest response was simulated by MRI-CGCM3, a GRA-forced model. MRI-CGCM3 has the highest horizontal resolution and second-highest vertical resolution of the set, and handles volcanic aerosols interactively. Therefore, it should be expected that CSIRO-Mk3L-1-2 would simulate a weak response even to a strong volcanic forcing, and MRI-CGCM3 a strong response to a weaker forcing. Comparison of the MPI-ESM-P response (higher resolution, CEA forcing) with the BCC-CSM1-1 response (lower resolution, stronger GRA forcing) is further evidence of the primary importance of model resolution.

Similarly to the results shown by *Toohey et al.* [2014] and *Bittner et al.*, [2016b] with the MPI-ESM, I have found that climate models can produce a strengthened polar vortex and surface warming in the first Northern Hemisphere winter after large volcanic eruptions, provided that a sufficiently strong volcanic forcing is considered. While I would not expect climate models on average to exactly simulate the observed response, which includes random variability, these results reaffirm that state-of-the-art climate models in general can simulate realistic responses to large volcanic eruptions. Furthermore, these last millennium ensembles have provided a clearer look at the role of model and forcing dependence on the simulated climate response. These results are important for diagnosing problems with and improving model simulations of volcanic eruptions, as well as for prescribing a single, standard volcanic forcing data set in the future. The upcoming VolMIP [*Zanchettin et al.*, 2016] will use the 1815 Tambora eruption as a standard experiment to force new climate models as part of CMIP6, to continue to improve the simulation of the climate response to volcanic eruptions.

CHAPTER 4: MODELING THE CLIMATE IMPACT OF THE 1783-1784 LAKI ERUPTION IN ICELAND

4.1 Introduction

The 1783-1784 Laki eruption in Iceland was unique in that it injected sulfur gas into the lower troposphere as well as into the lower stratosphere. In addition to a constant effusing of gas in the troposphere from June 8, 1783 to February 7, 1784, Laki was characterized by 10 approximately El Chichón-sized eruptions (see Table 4.1 for a list of the eruption episodes) which injected sulfur gas into the lower stratosphere from 9–13 km [*Thordarson and Self*, 2003]. In addition to its unique eruption type, Laki was followed by abrupt and unique regional climate change in the years following. The eruption was followed by an extremely warm summer in Europe, an extremely cold winter in most of the Northern Hemisphere (NH), and extreme drought, crop failure, and famine in Africa and Asia for several years.

While surface cooling and reductions of tropical precipitation are expected impacts of a volcanic eruption and have been reproduced by model studies in the past [e.g., *Oman et al.*, 2006a], the European heat wave in summer 1783 has yet to be explained or reproduced. Discussion remains as to whether the anomalously warm temperatures were due to greenhouse warming by sulfur gases in the troposphere that made their way to Europe from Iceland, or if the warming was merely an example of climate variability. Here, using the National Center for Atmospheric Research (NCAR) Community Earth System Model, version 1 (CESM1) [*Hurrell et al.,* 2013], an ensemble of simulations of the Laki eruption in Iceland is conducted in order to attempt to answer this question.

4.2 Model Description and Experiment Setup

CESM1 is composed of interactive atmosphere, ocean, land, and sea-ice components. The atmospheric component of CESM1 is the Community Atmosphere Model (CAM). For these experiments, I used the Whole Atmosphere Community Climate Model (WACCM) [*Marsh et al.*, 2013], the high-top version of CAM. WACCM has 70 vertical levels, a model top of 5.1 x 10^{-6} hPa and 0.9° latitude x 1.25° longitude horizontal resolution, with interactive atmospheric chemistry, radiation, and dynamics. The version of WACCM used here has been modified to include more realistic physics, as introduced in CAM, version 5 [*Neale et al.*, 2010]; this configuration includes more realistic formulations of radiation, cloud microphysics, and aerosols, as described in *Mills et al.* [2016]. Specifically, direct effects of aerosols are included in the radiation code, indirect effects of sulfur are included in the cloud microphysics [*Morrison and Gettelman*, 2008; *Gettelman et al.*, 2010], and aerosols are represented in a prognostic modal aerosol model (MAM) [*Liu et al.*, 2012], which has been modified to simulate the evolution of stratospheric sulfate aerosol from volcanic emissions.

The model employs the three-mode version of the Modal Aerosol Model (MAM3) [*Liu et al.*, 2012], which represents the aerosol as Aitken, accumulation, or coarse mode. MAM3 is capable of representing aerosol microphysical processes, such as nucleation, condensation, coagulation, and sedimentation, and calculates new particle formation using a parameterization of sulfuric acid-water homogeneous nucleation [*Vehkamäki et al.,* 2002; *Mills et al.*, 2016]. MAM3 has been modified to include prognostic stratospheric aerosols [Appendix B, *Mills et al.*, 2016].

The 1783-1784 Laki flood lava eruption began on June 8th, 1783 and lasted for 8 months, injecting a total of 122 Tg of SO_2 into the atmosphere. About 94 Tg of SO_2 were injected into the upper troposphere/lower stratosphere between 9 and 13 km, with another 28 Tg of SO_2 emitted at the surface from lava degassing. About 95% of the total SO_2 emission took place in the first 4 months of activity; the emissions in the last 4 months were due to the quiet emission of lava and gas. [see Figure 2 in *Thordarson and Self*, 2003]. I simulate the eruption by injecting 94 Tg of SO_2 over ten eruptions from June 8th to October 25th; the individual explosive eruption episodes range from injections of 2.9 to 18.7 Tg of SO_2 (Table 4.1). For each explosive episode, the emissions occur over a 6-hour period from 1200 to 1800 universal time. The SO_2 gas from the explosive episodes are evenly distributed within 5 vertical layers from 9-13 km. I simulate SO_2 emitted by lava degassing by injecting an additional 28 Tg of SO_2 in the lower troposphere from June 8th, 1783 to February 7th, 1784; the surface emissions were injected constantly over the 8-month period.

To initialize the model runs, I choose initial conditions that resemble the synoptic conditions reported over Europe around the time of the Laki eruption [*Kington*, 1988; *Thordarson and Self*, 2003]. I choose four sets of initial conditions from a 25-year control run based on this criterion (Figure 4.1). However, the background state of the global circulation is different for each set of initial conditions. In this way, it is possible to investigate the role of the background initial state in the impact of volcanic eruptions on climate. For example, I choose initial conditions with different El Niño/Southern Oscillation (ENSO) phases in order to investigate the ENSO response to high-latitude eruptions.

For each set of initial conditions, I generate 10 ensemble members by perturbing the temperature field. I run one ensemble member with the Laki eruption and one without, so that I have in the end a 40-member ensemble with the Laki eruption (Laki) and a 40-member ensemble without the eruption (noLaki). All ensemble members are initialized on June 8th, the first day of the Laki eruption. The year 1819 of the control simulation was selected as one of the ensemble initial conditions, and features a strong El Niño event, similar to the winter of 1783–1784 during the Laki eruption [*Cook and Krusic*, 2004; *D'Arrigo et al.*, 2011].

Unless otherwise noted, anomalies are calculated by subtracting the mean of the 5 years before the eruption. I analyze monthly means of model outputs, and all differences discussed in this study are assessed using the Student's *t*-test. Significance is reported at the 95% confidence level unless otherwise noted. I compare temperature responses to the average of 30 ensemble members from the latest reanalysis, the 400-year Ensemble Kalman Filter reanalysis [EKF400; *Franke et al.* 2017]. EKF400 uses instrumental data series, reconstructed sea-ice and temperature indices derived from documentary records, and proxy temperature reconstructions from Greenland ice cores and tree rings from Scandinavia and Siberia.

4.3 Evolution and Radiative effects of the Laki Aerosol Cloud

Figure 4.2 shows the zonal-mean and NH-mean sulfate aerosol optical depth (AOD) for the Laki ensemble from June 1783 to May 1784. The maximum optical depth perturbations in the ensemble mean occur near the pole and are above 1.3 in August. The peak NH-average AOD of 0.45 also occurs in August. Most of the aerosols have been removed by May 1783, with a NH-average AOD well below 0.1. The magnitude of the

AOD perturbations is in better agreement with *Oman et al.* [2006b] than other, more recent modeling studies of Laki-style volcanic eruptions. *Pausata et al.* [2015b] found much larger maximums in the optical depth, with a NH-average AOD anomaly above 1.4 in August; they attributed this discrepancy to the fact that aerosols do not grow by self-coagulation in their simulations.

Figure 4.3 shows the zonally averaged top-of-atmosphere radiative forcing from the Laki eruption. Figure 4.3a indicates a maximum reduction of insolation—approximately one month after the eruption onset—of about 27 W/m^2 between 60°N and 70°N. The spatial and temporal location of this maximum is consistent with the latitude of the eruption (64°N) and the timescale (weeks) for conversion of SO_2 to sulfate aerosols, the dominant driver of radiative effects from volcanic eruptions [*Robock*, 2000]. The radiative effects are strongly dependent on both time and latitude, with the shortwave anomalies below -1 W/m^2 at most latitudes by the following May, and anomalies near the equator much weaker than at high latitudes and lasting only a few months. A steep temporal gradient is also seen at high latitudes, but this is mostly due to a lack of insolation during boreal winter months, and is less dependent of the volcanic forcing.

Longwave forcing from the volcanic aerosols shows a similar spatial and temporal pattern (Figure 4.3a) to the shortwave forcing though, as expected, the anomalies are weaker and more transient. The maximum decrease of 7 W/m^2 in outgoing LW radiation occurs at high latitudes in mid-late July and persists into August. In contrast to the shortwave anomalies, the longwave forcing at high latitudes persists into the winter months. Still, by January LW anomalies are everywhere below 1 W/m^2.

Figure 4.3c shows the net radiative forcing due to the volcanic eruption, which is simply the linear combination of Figures 4.3a and 4.3b. With the exception of a small positive anomaly north of 70°N during NH fall months, the net forcing from Laki is negative; this is consistent with the well-documented cooling of the Earth after large volcanic eruptions [e.g., *Robock*, 2000]. The spatial and temporal patterns in Figure 4.3 are in agreement with past modeling studies of the Laki eruption [e.g., *Oman et al.*, 2006b]. However, the anomalies in this study are found to be lower in magnitude than those in *Oman, et al.* [2006b]. This is most likely due to different treatments of volcanic aerosols in the models. In Figure 4.4, the NH-average radiative forcing and near-surface air temperature anomalies are plotted. The NH-average net radiative forcing peaks with a value of -9 W/m^2 in July 1873 (Figure 4.4a). This large negative forcing is accompanied by cooling reaching below -2 K in the NH-average in October (Figure 4.4b). While the radiative forcing anomaly is approximately 2.5 times smaller than found by *Pausata et al.* [2015b], the peak cooling found there is more comparable (maximum cooling of -2.8 K in September), implying a nonlinear and/or dynamical response.

4.4 Summer 1783

Figure 4.5 shows the JJA 1783 surface temperature anomalies for the EKF400 reanalysis and the Laki ensemble. The cooling in the EKF400 reanalysis (Figure 4.5a) is concentrated mostly over Northern Eurasia, Northeastern North America, and Alaska, and is below -3 K in some areas. Tree ring maximum latewood density data show that the summer of 1783 was the coldest of the last 400 years in northwestern Alaska [*Jacoby et al.*, 1999]. In addition, tree ring width in the Polar Urals and Yamal Peninsula in northwest Siberia was the smallest in about 500-600 years [*Hantemirov et al.*, 2004].

These proxies, which are used to force the reanalysis, can help explain why the cooling in Figure 4.5a is strongest in these areas. In contrast to the cooling, Western Europe shows significant warming, most likely related to the exceedingly warm conditions in July 1783 [*Thordarson and Self*, 2003]. The Laki ensemble (Figure 4.5a) simulates strong, significant cooling over the entire extratropics and NH high latitudes, with anomalies almost uniformly below -2 K for the summer, and reaching below -3 K. The magnitude and spatial pattern of cooling in Figure 4.5b is very similar to that found in *Oman et al.* [2006b], and the cooling is about half as intense as in *Pausata et al.* [2015b], who simulated cooling below -7 K in parts of the NH.

In July 1783 northern, western and part of central Europe experienced an unusual heat wave [Figure 4.6a, *Franke et al.*, 2017]. July 1783 was among the warmest July on record in England [*Kington*, 1978; *Manley*, 1974; *Parker et al.*, 1992]. It was also very warm in Scandinavia [*Hólm*, 1784]. The occurrence of this extreme heat coincides with the maximum longwave radiative forcing in Figure 4.3b, and is also when the intensity of the Laki haze was the greatest in Western Europe. The EKF400 reanalysis shows that in the western part of Europe the 1783 July surface temperatures are up to 1.5 K higher than the 1778-1782 mean (Figure 4.6a). Figure 4.6a also shows July temperatures were near or below the norm in the rest of Europe. No model has been able to reproduce the observed warming, and it has therefore been challenging to attribute the warm July of 1783 in Europe to a specific response to the Laki eruption. It has been suggested that the July heat wave resulted from greenhouse warming caused by high SO_2 concentrations in the lower troposphere, emissions from Laki that did not convert to sulfate aerosols [*Wood*, 1992; *Rampino et al.*, 1995; *Grattan and Saddler*, 1999]. An alternative explanation is that the unusually warm weather may have been caused by anomalous atmospheric circulation over Europe in July 1783, resulting in anomalous southerly winds [*Thordarson and Self*, 2003]. That is, the warm spell in the summer after Laki happened by chance, and was simply an example of internal climate variability. Similar heat waves have occurred recently in Europe without volcanic eruptions as precursors; the summer of 2003 was extremely warm and cause many heat-related deaths [*Stott et al.*, 2004].

The Laki ensemble mean (Figure 4.6b) shows significant cooling over all of Western Europe, with anomalies reaching below -2.5 K in some areas of Europe. This response is consistent with the results in previous studies [e.g., *Oman et al.*, 2006a; *Pausata et al.*, 2015b], and is the expected response to a large, explosive volcanic eruption. On the other hand, the noLaki ensemble mean (Figure 4.6c) suggests that the warm July may have been, in fact, due to random variability. Figure 4.6c indicates significant warming over Europe, similar both in magnitude and spatial pattern to the EKF400 reanalysis shown in Figure 4.6a. Of course, the observed “response” to the Laki eruption in Europe in July 1783 represents only one possible response to the volcanic forcing [*Kay et al.*, 2015]. Therefore, it is important to look at the individual simulated responses, and not just the mean response, which averages out internal climate variability and may never actually be realized. For this reason, Figure 4.7 shows the July 1783 surface temperature anomalies for each of the 40 simulations from the Laki ensemble. Several simulations (e.g., 1, 12, 15, 21) show large warming above 3 K over Northern and Western Europe in spite of the eruption. These individual simulations highlight the importance of the background climate state on the volcanic effects.

The fact that this response is not always simulated does not preclude the Laki eruption as the cause of the response. However, Figure 4.8 shows that this type of anomaly over Europe occurs even more frequently in the noLaki ensemble (e.g., 1-14, 16-20). The high frequency observed in Figure 4.8 does imply that the anomaly might be a result of circulation, and not specifically caused by the Laki eruption. To further investigate this, I analyzed the sea-level pressure and near-surface wind patterns associated with this type of anomaly. In doing so, I find that the warm anomaly over Europe is associated with low pressure in the North Atlantic, resulting in cyclonic activity there, which carries warm maritime air from over the tropical Atlantic ocean northeast and over Europe. In Figure 4.9 I show the correlation between North Atlantic cyclonic activity and European surface air temperature in the simulations. The noLaki simulations with low pressure over the North Atlantic (Figure 4.9, top row) exhibit positive temperature anomalies originating in the Atlantic at around 30°N and extending northeast over Western and Northern Europe. The noLaki simulations without the low pressure over the Atlantic (Figure 4.89, row two) still do show positive anomalies over Europe, but they are more concentrated over Northern and Eastern Europe. The Laki simulations show similar patterns, where the ensemble members that simulate low pressure over the North Atlantic (Figure 4.9, row three) show reduced cooling over Western Europe when compared to the temperature response in the other Laki runs (Figure 4.9, bottom row). Therefore, I conclude that the warm July of 1783 in Europe was an example of natural variability, and was not a consequence of the Laki eruption. Furthermore, Europe may have experienced even more extreme heat in the absence of the eruption.

Other regions of the Northern Hemisphere also experienced unusual weather conditions in summer 1783. Severe drought was reported from India, the Yangtze region in China, and Egypt [*Mooley and Pant*, 1981; *Pant et al.*, 1992; *Volney*, 1788; *Wang and Zhao*, 1981; *Xu*, 1988]. Large reductions in precipitation are simulated in the Laki ensemble, with reductions in excess of -3 mm/d over the African Sahel and parts of India (Figure 4.10). Precipitation reductions are also seen in China, though to a lesser extent. The simulations show a southward shift of the Inter-Tropical Convergence Zone, a response that is consistent with the expected response to the asymmetric cooling of the NH by aerosol injected at high latitudes [*Colose et al.*, 2016].

4.5 Winter 1783-1784

In contrast to the warm summer of 1783, records show that winter 1783-1784 was cold and harsh [*D'Arrigo et al.*, 2011; *Luterbacher et al.*, 2004; *Thordarson and Self*, 2003 and references therein]. Benjamin Franklin wrote "perhaps the winter of 1783-4, was more severe, than any that had happened for many years" [*Franklin*, 1784]. *Thordarson and Self* [2003] wrote about historical accounts of "1-m thick snow" in April in the Jutland Peninsula.

Similarly to the anomalous summer, there is discussion as to whether the extremely cold of winter 1783-1784 was due to the Laki eruption, or just another example of climate variability. *D'Arrigo et al.* [2011] attributed the cold season to a combination of a negative phase of the North Atlantic Oscillation (NAO) and a positive phase of the El Niño Southern Oscillation (ENSO). However, they argued the case that this coincidence of a negative NAO and positive ENSO was in fact random, and that there was no reason to believe that volcanic aerosols from the Laki eruption forced either of these phenomena. On the other hand, [*Pausata et al.*, 2015a, 2016] showed that high-latitude eruptions *can* increase the likelihood of an El Niño in the winter following the eruption.

Figure 4.11 shows the DJF 1783-1784 surface temperature anomalies for the reanalysis and the Laki ensemble. The EKF400 reanalysis shows significant cooling over parts of Europe and North America, though the anomalies are below 1 K in most places. On the other hand, the Laki ensemble (Figure 4.11b) shows extreme cooling over most of the NH continents, cooling which is not observed in the no-Laki ensemble (not shown). The EKF400 reconstruction shows extreme cooling over most of Europe, and anomalies below -3 K covering a large area of Central Europe (Figure 4.12a). Western to Central Europe is the only NH land mass that does not see significant cooling in the Laki ensemble (Figure 4.8b). In contrast to the rest of the NH, the Laki and noLaki ensembles show similar mild conditions over Europe (Figure 4.12b-c).

Figure 4.13 shows the sea level pressure anomalies for the winter after the Laki Eruption for the two ensembles. The EKF400 reanalysis (Figure 4.13a) shows a negative phase of the NAO, with low pressure over much of the Atlantic Ocean and Western Europe and high pressure over Greenland and poleward. This pattern is not seen in the either the Laki or noLaki ensemble (Figure 4.6b-c). Furthermore, a positive phase of the NAO is observed in both ensembles. Therefore, I do not find that the Laki aerosol cloud forced a negative phase of the NAO, in partial agreement with the conclusions of *D'Arrigo et al.* [2011].

I also analyzed the effect of the volcanic eruption on ENSO. To characterize ENSO in the simulations, I use monthly SST anomalies averaged over the Niño3.4 region

(5°N to 5°S, 170°W to 120°W). I applied a 5-month running mean and divide the Laki and noLaki ensemble members into three groups according to the incipient ENSO state. I follow the convention of *Pausata et al.* [2016] in defining the ENSO state by the September through February average Niño3.4 index in the no-volcano control simulation: El Niño (Niño3.4 index > 0.6 K), La Niña (Niño3.4 index < –0.6 K), and Neutral (–0.6 K < Niño3.4 index < 0.6 K) case. Figure 4.14 shows the Niño 3.4 indices for the two ensembles for the year after the Laki eruption. In all three cases (La Niña, neutral, and El Niño incipient state), the Laki ensemble simulates a positive anomaly in the ENSO state when compared with the noLaki ensemble. This result is in agreement with *Pausata et al.* [2016], who found that the southward-shifted ITCZ after a high-latitude volcanic eruption can trigger a positive ENSO anomaly.

4.6 Summary and Discussion

I have conducted an ensemble of model simulations of the 1783-1784 Laki volcanic eruption in Iceland, in order to analyze its effect on regional and NH climate in the year following the eruption. Results indicate that the abnormally warm summer in Europe in 1783 was in fact due to variability of the climate system. Low pressure over the North Atlantic brought air to Europe from the warm Atlantic Ocean, and Europe may have been even warmer had the eruption not occurred. In addition to the warming in Europe, much of Africa and Asia was struck by crop failure and extreme famine as a result of severe reductions of precipitation after the eruption. These precipitation reductions are captured in the model runs. It has been hypothesized that the anomalously cold winter in 1783-1784 was caused by a negative phase of the NAO in combination with a positive phase of ENSO. I find a robust increase in the ENSO phase as a result of the Laki eruption; however, I find no dynamic wintertime NAO response to the eruption.

CHAPTER 5: SUMMARY AND DISCUSSION

The work presented in this dissertation examined the effects of volcanic eruptions on the climate system. Chapters 2 and 3 were motivated by studies suggesting that current climate models cannot produce the dynamical winter warming response that has been observed after large tropical volcanic eruptions [*Driscoll et al.*, 2012]. Chapter 4 is motivated by the uncharacteristic climate anomalies that followed the Laki eruption in Iceland.

In Chapter 2, I assessed the winter warming response in the CMIP5 historical ensemble. The results showed that most models can simulate a surface winter warming response in the first winter after a large tropical volcanic eruption. On the other hand, many models have difficulty simulating the strengthening of the polar vortex as identified in the 50 hPa geopotential height field. In Chapter 3 I assessed the winter warming response in the PMIP3 past1000 simulations. Most models produced a significant winter warming response to the past1000 forcing, which includes many more large eruptions than the historical period.

In Chapter 4 I used a state-of-the-art climate model to analyze the climate impacts of the 1783-1784 Laki eruption in Iceland. I showed that the warm July in Europe was due to natural variability and was not a Laki effect. I also showed that the harsh winter of 1783-1784 was caused partially by the eruption, which forced a positive phase of ENSO. On the other hand, the Laki eruption did not force a negative phase of the NAO.

References

Adams, J. B., M. E. Mann, and C. M. Ammann (2003), Proxy evidence for an El Nino-like response to volcanic forcing, *Nature*, *426*, 274-278.

Ammann, C. M., G. A. Meehl, W. M. Washington, and C. S. Zender (2003), A monthly and latitudinally varying volcanic forcing dataset in simulations of 20th century climate, *Geophys. Res. Lett., 30*(12), 1657, doi:10.1029/2003GL016875.

Ammann, C. M., F. Joos, D. S. Schimel, B. L. Otto-Bliesner, and R. A. Tomas (2007), Solar influence on climate during the past millennium: Results from transient simulations with the NCAR Climate System Model, *Proc. Natl. Acad. Sci. U.S.A., 104*, 3713–3718.

Andres, R. J., and A. D. Kasgnoc (1998), A time averaged inventory of subaerial volcanic sulphur emissions, *J. Geophys. Res., 103*(D19), 25,251–25, 261.

Antuña, J. C., A. Robock, G. L. Stenchikov, L. W. Thomason, and J. E. Barnes (2002), Lidar validation of SAGE II aerosol measurements after the 1991 Mount Pinatubo eruption, *J. Geophys. Res.*, *107*(D14), 4194, doi:10.1029/2001JD001441.

Baldwin, M. P., and T. J. Dunkerton (2001), Stratospheric harbingers of anomalous weather regimes, *Science*, *294*(5542), 581–584, doi:10.1126/science.1063315.

Barnes, E., S. Solomon, and L. Polvani (2016), Robust wind and precipitation responses to the Mount Pinatubo eruption, as simulated in the CMIP5 models. *J. Climate*, *29*, 4763–4778, doi:10.1175/JCLI-D-15-0658.1.

Bentsen, M., et al. (2013), The Norwegian Earth System Model, NorESM1-M – Part 1: Description and basic evaluation, *Geosci. Model Dev. Discuss.*, *5*(3), 2843–2931, doi:10.5194/gmdd-5-2843-2012.

Bi, D., et al. (2013), The ACCESS Coupled Model: Description, Control Climate and Evaluation, *Aust. Met. Oceanogr. J.*, *63*(1):41-64.

Bittner, M., H. Schmidt, C. Timmreck, and F. Sienz (2016a), Using a large ensemble of simulations to assess the Northern Hemisphere stratospheric dynamical response to tropical volcanic eruptions and its uncertainty, *Geophys. Res. Lett.*, *43*, doi:10.1002/2016GL070587.

Bittner, M., C. Timmreck, H. Schmidt, M. Toohey, and K Krüger (2016b), The impact of wave-mean flow interaction on the Northern Hemisphere polar vortex after tropical volcanic eruptions, *J. Geophys. Res. Atmos.*, *121*, 5281–5297, doi:10.1002/2015JD024603.

Braconnot, P., et al. (2012), Evaluation of climate models using palaeoclimatic data, *Nature Climate Change*, *2*, 417-424, doi:10.1038/nclimate1456.

Charlton-Perez, A. J., et al. (2013), On the lack of stratospheric dynamical variability in low-top versions of the CMIP5 models, *J. Geophys. Res. Atmos.*, *118*, 2494–2505, doi:10.1002/jgrd.50125.

Christiansen, B. (2008), Volcanic eruptions, large-scale modes in the Northern Hemisphere, and the El Niño–Southern Oscillation, *J. Climate*, *21*, 910–922.

Chylek, P., J. Li, M. K. Dubey, M. Wang, and G. Lesins (2011), Observed and model simulated 20th century Arctic temperature variability: Canadian Earth System Model CanESM2, *Atmos. Chem. Phys. Discuss.*, *11*(8), 22893–22907, doi:10.5194/acpd-11-22893-2011.

Collins, W. et al. (2011), Development and evaluation of an Earth-System model – HadGEM2, *Geosci. Model Dev.*, *4*, 1051–1075, doi:10.5194/gmd-4-1051-2011.

Colose, C. M., A. N. LeGrande, and M. Vuille, (2016), Hemispherically asymmetric volcanic forcing of tropical hydroclimate during the last millennium. *Earth Syst.*

Dyn., *7*, 681-696, doi:10.5194/esd-7-681-2016.

Compo, G. P., et al. (2011), The twentieth century reanalysis project, *Q. J. R. Meteorol. Soc.*, *137*(654), 1–28, doi:10.1002/qj.776.

Crowley, T. J., G. Zielinski, B. Vinther, R. Udisti, K. Kreutz, J. Cole-Dai, and E. Castellano (2008), Volcanism and the Little Ice Age, *Pages News*, *16*, 22–23.

Crowley, T. J. and M. B. Unterman (2013): Technical details concerning development of a 1200 yr proxy index for global volcanism, *Earth Syst. Sci. Data*, *5*, 187-197, doi:10.5194/essd-5-187-2013.

D'Arrigo, R., R. Seager, J. E. Smerdon, A. N. LeGrande, and E. R. Cook (2011), The anomalous winter of 1783–1784: Was the Laki eruption or an analog of the 2009–2010 winter to blame?, *Geophys. Res. Lett., 38*, L05706, doi:10.1029/2011GL046696.

de Lamanon, R. P. C. (1799), Observations on the nature of the fog of 1783, *A. Tilloch's Phil. Mag. London*, 80–89.

Delworth, T.D., et al. (2006), GFDL's CM2 global coupled climate models-Part I: Formulation and simulation characteristics, *J. Climate*, *19*, 643-674.

Ding, Y., J. A. Carton, G. A. Chepurin, G. Stenchikov, A. Robock, L. T. Sentman, and J. P. Krasting (2014), Ocean response to volcanic eruptions in Coupled Model Intercomparison Project 5 simulations, *J. Geophys. Res. Oceans*, *119*, 5622–5637, doi:10.1002/2013JC009780.

Donner, L. J. et al. (2011), The Dynamical Core, Physical Parameterizations, and Basic Simulation Characteristics of the Atmospheric Component AM3 of the GFDL Global Coupled Model CM3, *J. Climate*, *24*(13), 3484–3519, doi:10.1175/2011JCLI3955.1.

Driscoll, S., A. Bozzo, L. J. Gray, A. Robock, and G. Stenchikov (2012), Coupled Model Intercomparison Project 5 (CMIP5) simulations of climate following volcanic eruptions, *J. Geophys. Res., 117*, D17105, doi:10.1029/2012JD017607.

Dufresne, J., Foujols, M., Denvil, S. et al. (2013), Climate change projections using the IPSL-CM5 Earth System Model: from CMIP3 to CMIP5, *Clim Dyn*, *40*(9), 2123-2165, doi:10.1007/s00382-012-1636-1.

Fels, S. B., J. D. Mahlman, M. D. Schwarzkopf, and R. W. Sinclair, Stratospheric sensitivity to perturbations in ozone and carbon dioxide: Radiative and dynamical responses*, J. Atmos. Sci.*, *37*, 2265 – 2297, 1980.

Fischer, E. M., J. Luterbacher, E. Zorita, S. F. B. Tett, C. Casty, and H. Wanner (2007), European climate response to tropical volcanic eruptions over the last half millennium, *Geophys. Res. Lett.*, *34*, L05707, doi:10.1029/2006GL027992.

Franke, J., S. Brönnimann, J. Bhend, and Y. Brugnara (2017), A monthly global paleo-reanalysis of the atmosphere from 1600 to 2005 for studying past climatic variations, *Scientific Data*, *4*, 170076, doi:10.1038/sdata.2017.76.

Franklin, B. (1784), Meteorological imaginations and conjectures, *Manchester Lit. Philos. Soc. Mem. Proc., 2*, 122.

Gao, C., L. Oman, A. Robock, and G. L. Stenchikov (2007), Atmospheric volcanic loading derived from bipolar ice cores: Accounting for the spatial distribution of volcanic deposition, *J. Geophys. Res.*, *112*, D09109, doi:10.1029/2006JD007461.

Gao, C., A. Robock, and C. Ammann, (2008), Volcanic forcing of climate over the last 1500 years: An improved ice core-based index for climate models. *J. Geophys. Res.*, *113*, D23111, doi:10.1029/2008JD010239.

Gent, P. R. et al. (2011), The Community Climate System Model Version 4, *J. Climate*, *24*(19), 4973–4991, doi:10.1175/2011JCLI4083.1.

Gerber, E. P., et al. (2012), Assessing and understanding the impact of stratospheric dynamics and variability on the Earth system, *Bull. Am. Meteorol. Soc.*, *93*(6), 845–859, doi:10.1175/BAMS-D-11-00145.1.

Gettelman, A., X. Liu, S. J. Ghan, H. Morrison, S. Park, A. J. Conley, S. A. Klein, J. Boyle, D. L. Mitchell, and J. L. F. Li (2010), Global simulations of ice nucleation and ice supersaturation with an improved cloud scheme in the Community Atmosphere Model, *J. Geophys. Res.*, *115*, D18216, doi:10.1029/2009JD013797.

Giorgetta, M. A. et al. (2013), Climate and carbon cycle changes from 1850 to 2100 in MPI-ESM simulations for the coupled model intercomparison project phase 5, *J. Adv. Model. Earth Syst.*, *5*, 572–597, doi:10.1002/jame.20038.

Graf, H.-F., Q. Li, and M. A. Giorgetta (2007), Volcanic effects on climate: revisiting the mechanisms, *Atmos. Chem. Phys.*, *7*(17), 4503–4511, doi:10.5194/acp-7-4503-2007.

Grattan, J. P., and J. Sadler (1999), Regional warming of the lower atmosphere in wake of volcanic eruptions: The role of the Laki fissure eruption in the hot summer of 1783, *Geol. Soc. London, Spec. Publ., 16*, 161 – 172.

Grieser, J., and C. D. Schönwiese (1999), Parameterization of spatiotemporal patterns of volcanic aerosol induced stratospheric optical depth and its climate radiative forcing, *Atmosfera*, *12*(2), 111–133.

Groisman, P. Y. (1985), Regional climate consequences of volcanic eruptions (in Russian), *Meteorol. Hydrol.*, No. 4, 39–45.

Hantemirov, R. M., L. A. Gorlanova, and S. G. Shiyatov (2004), Extreme temperature events in summer in northwest Siberia since AD 742 inferred from tree rings, *Palaeogeogr. Palaeoclimatol. Palaeoecol.*, *209*(1–4), 155–164. doi:10.1016/ j.palaeo.2003.12.023.

Hólm, S. M. (1784), About the Earth Fire in Iceland in the Year 1783, 83 pp., Peder Horrebow, Copenhagen.

Hurrell, J. W. (1995), Decadal trends in the North Atlantic Oscillation: Regional temperatures and precipitation, *Science*, *269*, 676–679.

Hurrell, J. W. et al. (2013), The Community Earth System Model: A Framework for Collaborative Research, *Bull. Am. Meteorol. Soc.*, *94*(9), 1339–1360, doi:10.1175/BAMS-D-12-00121.1.

Iles, C. E., and G. C. Hegerl (2014), The global precipitation response to volcanic eruptions in the CMIP5 models. *Environ. Res. Lett.*, *9*, doi:10.1088/1748-9326/9/10/104012.

Iles, C. E., and G. C. Hegerl (2015), Systematic change in global patterns of streamflow following volcanic eruptions, *Nature Geoscience*, *8*, 838–842, doi:10.1038/ngeo2545.

Jacoby, G. C., K. W. Workman, and R. D. D'Arrigo (1999), Laki eruption of 1783, tree rings, and disaster for northwest Alaska Inuit, *Quat. Sci. Rev.*, *18*(12), 1365-1371, doi:10.1016/S0277-3791(98)00112-7.

Johns, T.C., et al. (2003), Anthropogenic climate change for 1860 to 2100 simulated with the HadCM3 model under updated emissions scenarios. *Climate Dynamics*, *20*, 583-612.

Kay, J. E., et al. (2015), The Community Earth System Model (CESM) Large Ensemble Project: A Community Resource for Studying Climate Change in the Presence of Internal Climate Variability, *Bulletin of the American Meteorological Society*, *96*, 1333-1349, doi: 10.1175/BAMS-D-13-00255.1.

Khodri, M., T. Izumo, J. Vialard, S. Janicot, C. Cassou, M. Lengaigne, J. Mignot, G. Gastineau, E. Guilyardi, N. Lebas, A. Robock, and M. J. McPhaden, (2017), Tropical explosive volcanic eruptions can trigger El Niño by cooling tropical Africa, *Nature Communications*, *8*, 778, doi:10.1038/s41467-017-00755-6.

Kington, J. A. (1978), Historical daily synoptic weather maps from the 1780's, *J. Meteorol., 3*, 65–70.

Kington, J. A. (1978), *The Weather of the 1780's Over Europe*, 164 pp., Cambridge Univ. Press, New York.

Kirchner, I., and H.-F. Graf (1995), Volcanos and El Niño: Signal separation in Northern Hemisphere winter, *Clim. Dyn.*, *11*, 341-358.

Kirchner, I., G. L. Stenchikov, H.-F. Graf, A. Robock, and J. C. Antuña (1999), Climate model simulation of winter warming and summer cooling following the 1991 Mount Pinatubo volcanic eruption, *J. Geophys. Res*., *104*, 19,039–19,055.

Kodera, K., M. Chiba, H. Koide, A. Kitoh, and Y. Nikaidou (1996), Interannual variability of the winter stratosphere and troposphere in the Northern Hemisphere, *J. Meteorol. Soc. Japan*, *74*, 365–382.

Kravitz, B., and A. Robock (2011), Climate effects of high-latitude volcanic eruptions: Role of the time of year, *J. Geophys. Res.*, *116*, D01105, doi:10.1029/2010JD014448.

Krueger, A. J., C. C. Schnetzler, and L. S. Walter (1996), The December 1981 eruption of Nyamuragira Volcano (Zaire) and the origin of the "mystery cloud" of early 1982, *J. Geophys. Res.*, *101*, 15,191–15,196.

Lacis, A., J. Hansen, and M. Sato (1992), Climate forcing by stratospheric aerosols. *Geophys. Res. Lett.*, *19*, 1607-1610, doi:10.1029/92GL01620.

Lamb, H. H. (1970), Volcanic dust in the atmosphere, with a chronology and assessment of its meteorological significance, *Philos. Trans. R. Soc. London*, *Ser. A*, *266*, 425–533.

Lambert, A., R. G. Grainger, C. D. Rogers, F. W. Taylor, L. L. Mergenthaler, J. B. Kumer, and S. T. Massie (1997), Global evolution of the Mount Pinatubo volcanic aerosols observed by the infrared limb-sounding instruments CLAES and ISAMS on the Upper Atmosphere Research Satellite, *J. Geophys. Res.*, *102*, 1495-1512.

Le, T. (2017), ENSO response to external forcing in CMIP5 simulations of the last millennium, *Glob. Plan. Change*, *148*, 105-112.

Liu, F., J. Chai, B. Wang, J. Liu, X. Zhang, and Z. Wang (2016), Global monsoon precipitation responses to large volcanic eruptions, *Sci. Rep.*, *6*, 24331, doi:10.1038/srep24331.

Liu, J., B. Wang, H. Wang, X. Kuang, and R. Ti (2011), Forced response of the East Asian summer rainfall over the past millennium: results from a coupled model simulation, *Clim. Dyn.*, *36*, 323–336, doi:10.1007/s00382-009-0693-6.

Liu, X., et al. (2012), Toward a minimal representation of aerosols in climate models: Description and evaluation in the Community Atmosphere Model CAM5, *Geosci. Model Dev.*, *5*(3), 709–739, doi:10.5194/gmd-5-709-2012.

Luterbacher, J., Dietrich, D., Xoplaki, E., Grosjean, M., and Wanner, H., (2004), European seasonal and annual temperature variability, trends, and extremes since 1500, *Science*, *303*, 1499-1503.

Maher, N., S. McGregor, M. H. England, and A. Sen Gupta (2015), Effects of volcanism on tropical variability, *Geophys. Res. Lett.*, *42*, 6024–6033, doi:10.1002/2015GL064751.

Man, W. and T. Zhou (2014), Response of the East Asian summer monsoon to large volcanic eruptions during the last millennium, *Chin. Sci. Bull.*, *59*(31), 4123-4129, doi:10.1007/s11434-014-0404-5.

Man W., T. Zhou, and J. Jungclaus (2012), Simulation of the East Asian Summer Monsoon during the Last Millennium with the MPI Earth System Model, *J. Clim.*, *25*(22), 7852-7866, doi:10.1175/JCLI-D-11-00462.1.

Man W., T. Zhou, and J. Jungclaus (2014), Effects of Large Volcanic Eruptions on Global Summer Climate and East Asian Monsoon Changes during the Last Millennium: Analysis of MPI-ESM Simulations, *J. Clim.*, *27*, 7394-7409, doi:10.1175/JCLI-D-13-00739.1.

Manley, G. (1974), Central England temperatures: Monthly means 1659 –1973, *Q. J. R. Meteorol. Soc., 100*, 389– 405.

Mann, M. E., M. A. Cane, S. E. Zebiak, and A. Clement (2005), Volcanic and solar forcing of the tropical Pacific over the past 1000 years, *J. Clim.*, *18*(3), 447–456.

Marsh, D., M. Mills, D. E. Kinnison, and J. -F. Lamarque, (2013), Climate change from 1850 to 2005 simulated in CESM1(WACCM). *Journal of Climate*, *26*, 7372-7391, doi:10.1175/JCLI-D-12-00558.1.

Marshall, A. G., A. A. Scaife, and S. Ineson (2009), Enhanced seasonal prediction of European winter warming following volcanic eruptions, *J. Clim.*, *22*(23), 6168–6180, doi:10.1175/2009JCLI3145.1.

McCormick, M.P., P. Hamill, T. J. Pepin, W. P. Chu, T. J. Swissler, and L. R. McMaster (1979), Satellite studies of the stratospheric aerosol, *Bull. Am. Meteorol. Soc.*, *60*, 1038-1046.

McGregor, S., and A. Timmermann (2011), The effect of explosive tropical volcanism on ENSO, *J. Clim.*, *24*(8), 2178–2191.

Metzner, D., S. Kutterolf, M. Toohey, C. Timmreck, U. Neimeier, A. Freundt, and K. Krüger (2014), Radiative forcing and climate impact resulting from SO2 injections based on a 200,000-year record of Plinian eruptions along the Central American Volcanic Arc, *Int. J. Earth Sci.*, *103*, 2063-2079, doi:10.1007/s00531-012-0814-z.

Mills, M. J., et al. (2016), Global volcanic aerosol properties derived from emissions, 1990–2014, using CESM1(WACCM), *J. Geophys. Res. Atmos.*, *121*, 2332–2348, doi:10.1002/2015JD024290.

Minnis, P., E. Harrison, L. Stowe, G. Gibson, F. Denn, D. Doelling, and W. Smith (1993), Radiative climate forcing by the Mount Pinatubo eruption, *Science*, *259*, 1411–1415.

Mitchell, J. M., Jr. (1970), A preliminary evaluation of atmospheric pollution as a cause of the global temperature fluctuation of the past century, in *Global Effects of Environmental Pollution*, edited by S. F. Singer, pp. 139–155, D. Reidel, Norwell, Mass.

Mitchell, D. M., L. J. Gray, and A. J. Charlton-Perez (2011), The structure and evolution of the stratospheric vortex in response to natural forcings, *J. Geophys. Res.*, *116*, D15110, doi:10.1029/2011JD015788.

Mooley, D. A., and G. B. Pant (1981), Droughts in India over the last 200 years, their socio-economic impacts and remedial measures for them, in *Climate and History: Studies in Past Climates and Their Impact on Man*, edited by T. M. L. Wigley, M. J. Ingram, and G. Farmer, pp. 465–478, Cambridge Univ. Press, New York.

Morrison, H., and A. Gettelman (2008), A new two-moment bulk stratiform cloud microphysics scheme in the Community Atmosphere Model, Version 3 (CAM3). Part I: Description and numerical tests, *J. Clim.*, *21*, 3642, doi:10.1175/2008JCLI2105.1.

Neale, R. B., et al. (2010), Description of the NCAR Community Atmosphere Model (CAM 5.0), *NCAR Tech. Rep. NCAR/TN-4861STR*.

Oman, L., A. Robock, G. L. Stenchikov, G. A. Schmidt, and R. Ruedy (2005), Climatic response to high-latitude volcanic eruptions, *J. Geophys. Res.*, *110*, D13103, doi:10.1029/2004JD005487.

Oman, L., A. Robock, G. L. Stenchikov, and T. Thordarson (2006a), High-latitude eruptions cast shadow over the African monsoon and the flow of the Nile, *Geophys. Res. Lett.*, *33*, L18711, doi:10.1029/2006GL027665.

Oman, L., A. Robock, G. L. Stenchikov, T. Thordarson, D. Koch, D. T. Shindell, and C. Gao (2006b), Modeling the distribution of the volcanic aerosol cloud from the 1783–1784 Laki eruption, *J. Geophys. Res.*, *111*, D12209, doi:10.1029/2005JD006899.

Otterå, O. (2008), Simulating the effects of the 1991 Mount Pinatubo volcanic eruption using the ARPEGE atmosphere general circulation model, *Adv. Atmos. Sci.*, *25*, 213–226, doi:10.1007/s00376-008-0213-3.

Otto-Bliesner, B.L., E.C. Brady, J. Fasullo, A. Jahn, L. Landrum, S. Stevenson, N. Rosenbloom, A. Mai, G. Strand (2016), Climate Variability and Change since 850 C.E.: An Ensemble Approach with the Community Earth System Model (CESM), *Bull. Amer. Met. Soc., 97,* 735–754, doi: 10.1175/BAMS-D-14-00233.1.

Pant, G. B., B. Parthasarathy, and N. A. Sontakke (1992). Climate over India during the first quarter of the nineteenth century, in *The Year Without a Summer?*, edited by C. R. Harrington, pp. 429–435, Can. Mus. of Nature, Ottawa.

Parker, D. E., T. P. Legg, and C. K. Folland (1992), A new daily Central England Temperature series, 1772–1991, *Int. J. Climatol., 12*, 317– 342.

Pausata, F. S. R., L. Chafik, R. Caballero, and D. S. Battisti (2015a), Impacts of a high-latitude volcanic eruption on ENSO and AMOC, *Proc. Natl. Acad. Sci., 112*(45), 13784–13788.

Pausata, F. S. R., A. Grini, R. Caballero, A. Hannachi and Ø. Seland (2015b), High-latitude volcanic eruptions in the Norwegian Earth System Model: the effect of different initial conditions and of the ensemble size, *Tellus B: Chemical and Physical Meteorology*, *67*:1, 26728, DOI: 10.3402/tellusb.v67.26728.

Pausata, F. S. R., C. Karamperidou, R. Caballero, and D. S. Battisti (2016), ENSO response to high-latitude volcanic eruptions in the Northern Hemisphere: the role of the initial conditions, *Geophys. Res. Lett., 43*(16), 8694-8702.

Perlwitz, J., and H.-F. Graf (1995), The statistical connection between tropospheric and stratospheric circulation of the Northern Hemisphere in winter, *J. Climate, 8*, 2281–

2295.

Pinto, J. P., R. P. Turco, and O. B. Toon (1989), Self-limiting physical and chemical effects in volcanic eruption clouds, *J. Geophys. Res.*, *94*, 11,165–11,174.

Predybaylo, E., G. L. Stenchikov, A. T. Wittenberg, and F. Zeng (2017), Impacts of a Pinatubo-Size Volcanic Eruption on ENSO, *J. Geophys. Res. Atmos.*, *122*, doi:10.1002/2016JD025796.

Ramachandran, S., V. Ramaswamy, G. L. Stenchikov, and A. Robock (2000), Radiative impact of the Mount Pinatubo volcanic eruption: Lower stratospheric response, *J. Geophys. Res.*, *105*(D19), 24,409–24,429.

Rampino, M. R., T. Thordarson, and S. Self (1995), A new volcanism/climate connection: Tropospheric SO2 greenhouse effect from the Laki (Iceland) 1783 fissure eruption, in *IUGG XXI General Assembly*, p. 278.

Robock, A. (1983), The dust cloud of the century, *Nature*, *301*, 373–374.

Robock, A., and J. Mao, (1992), Winter warming from large volcanic eruptions. *Geophys. Res. Lett.*, *19*, 2405-2408.

Robock, A., and Y. Liu (1994), The volcanic signal in Goddard Institute for Space Studies three-dimensional model simulations, *J. Climate*, *7*, 44-55.

Robock, A., and J. Mao (1995), The volcanic signal in surface temperature observations, *J. Clim.*, *8*, 1086–1103.

Robock, A., K. Taylor, G. Stenchikov, and Y. Liu, (1995), GCM evaluation of a mechanism for El Niño triggering by the El Chichón ash cloud, *Geophys. Res. Lett.*, *22*(17), 2369–2372.

Robock, A. (2000), Volcanic eruptions and climate. *Rev. Geophys.*, *38*, 191-219.

Robock, A., T. Adams, M. Moore, L. Oman, and G. Stenchikov (2007), Southern Hemisphere atmospheric circulation effects of the 1991 Mount Pinatubo eruption, *Geophys. Res. Lett.*, *34*, L23710, doi:10.1029/2007GL031403.

Robock, A., L. Oman, and G. L. Stenchikov (2008), Regional climate responses to geoengineering with tropical and Arctic SO2 injections, *J. Geophys. Res.*, *113*, D16101, doi:10.1029/2008JD010050.

Rotstayn, L. D., and U. Lohmann (2002), Tropical rainfall trends and the indirect aerosol effect, *J. Climate*, *15*, 2103-2116.

Rotstayn, L. D., M. A. Collier, M. R. Dix, Y. Feng, H. B. Gordon, S. P. O'Farrell, I. N. Smith, and J. Syktus (2010), Improved simulation of Australian climate and ENSO-related rainfall variability in a global climate model with an interactive aerosol treatment, *Int. J. Climatol.*, *30*(7), 1067–1088, doi:10.1002/joc.1952.

Rozanov, E. V., M. E. Schlesinger, N. G. Andronova, F. Yang, S. L. Malyshev, V. A. Zubov, T. A. Egorova, and B. Li (2002), Climate/chemistry effects of the Pinatubo volcanic eruption simulated by the UIUC stratosphere/troposphere GCM with interactive photochemistry, *J. Geophys. Res.*, *107*(D21), 4594, doi:10.1029/2001JD000974.

Sato, M., J. E. Hansen, M. P. McCormick, and J. B. Pollack (1993), Stratospheric aerosol optical depths, 1850–1990, *J. Geophys. Res.*, *98*(D12), 22,987–22,994.

Schmidt, G. A., et al. (2011), Climate forcing reconstructions for use in PMIP simulations of the last millennium (v1.0). *Geosci. Model Dev.*, *4*, 33-45, doi:10.5194/gmd-4-33-2011.

Schmidt, G. A., et al. (2014), Configuration and assessment of the GISS ModelE2 contributions to the CMIP5 archive, *J. Adv. Model. Earth Syst.*, *6*(1), 141–184, doi:10.1002/2013MS000265.

Self, S., M. R. Rampino, J. Zhao, and M. G. Katz (1997), Volcanic aerosol perturbations and strong El Nino events: No general correlation, *Geophys. Res. Lett.*, *24*(10), 1247–1250.

Shindell, D. T., Schmidt, G. A., Miller, R. L., and Rind, D. (2001), Northern Hemisphere winter climate response to greenhouse gas, ozone, solar, and volcanic forcing, *J. Geophys. Res.*, *106*, D07193, doi:10.1029/2000JD900547.

Shindell, D. T., G. A. Schmidt, M. E. Mann, and G. Faluvegi (2004), Dynamic winter climate response to large tropical volcanic eruptions since 1600, *J. Geophys. Res.*, *109*, D05104, doi:10.1029/2003JD004151.

Sigl, M. et al. (2014), Insights from Antarctica on volcanic forcing during the Common Era, *Nature Climate Change*, *4*, 693-697, doi: 10.1038/NCLIMATE2293.

Sigl, M. et al. (2015), Timing and climate forcing of volcanic eruptions for the past 2,500 years, *Nature*, *523*, 543–549, doi:10.1038/nature14565.

Solomon, S., R. W. Portmann, R. R. Garcia, L. W. Thomason, L. R. Poole, and M. P. McCormick (1996), The role of aerosol variations in anthropogenic ozone depletion at northern midlatitudes, *J. Geophys. Res.*, *101*, 6713-6727.

Solomon, S. (1998), Stratospheric ozone depletion: A review of concepts and history, *Rev. Geophys.*, *37*(3), 275-316.

Stenchikov, G. L., I. Kirchner, A. Robock, H. –F. Graf, J. C. Antuña, R. Grainger, A. Lambert, and L. Thomason (1998), Radiative forcing from the 1991 Mount Pinatubo volcanic eruption, *J. Geophys. Res.*, *103*, 13,837–13,857.

Stenchikov, G., A. Robock, V. Ramaswamy, M. D. Schwarzkopf, K. Hamilton, and S. Ramachandran (2002), Arctic Oscillation response to the 1991 Mount Pinatubo eruption: Effects of volcanic aerosols and ozone depletion, *J. Geophys. Res.*, *107*(D24), 4803, doi:10.1029/2002JD002090.

Stenchikov, G., K. Hamilton, A. Robock, V. Ramaswamy, and M. D. Schwarzkopf (2004), Arctic Oscillation response to the 1991 Pinatubo eruption in the SKYHI GCM with a realistic Quasi-Biennial Oscillation, *J. Geophys. Res.*, *109*, D03112, doi:10.1029/2003JD003699.

Stenchikov, G., K. Hamilton, R. J. Stouffer, A. Robock, V. Ramaswamy, B. Santer, and H.-F. Graf (2006), Arctic Oscillation response to volcanic eruptions in the IPCC AR4 climate models, *J. Geophys. Res.*, *111*, D07107, doi:10.1029/2005JD006286.

Stevenson, S., B. Otto-Bliesner, J. Fasullo, and E. Brady, (2016) El Niño-like hydroclimate responses to Last Millennium volcanic eruptions, *J. Clim.*, *29*, 2907-2921, doi:10.1175/JCLI-D-15-0239.1.

Stevenson, S., J. T. Fasullo, B. L. Otto-Bliesner, R. A. Tomas, and C. Gao (2017), Role of eruption season in reconciling model and proxy responses to tropical volcanism, *Proc. Nat. Acad. Sci.*, *114*(8), 1822–1826, doi: 10.1073/pnas.1612505114.

Stott, P. A., D. A. Stone, and M. R. Allen (2004), Human contribution to the European heatwave of 2003, *Nature, 432*, 610– 614.

Taylor, K. E., R. J. Stouffer, and G. A. Meehl (2012), An overview of CMIP5 and the experiment design, *Bull. Amer. Meteor. Soc.*, *93*, 485-498, doi:10.1175/BAMS-D-11-00094.1.

Thomas, M.A., C. Timmreck, M.A. Giorgetta, H.-F. Graf, and G. Stenchikov (2009), Simulation of the climate impact of Mt. Pinatubo eruption using ECHAM5 – Part 1: Sensitivity to the modes of atmospheric circulation and boundary conditions, *Atmos. Chem. Phys.*, *9*, 757-769.

Thompson, D. W. J., and J. M. Wallace (1998), The Arctic Oscillation signature in the wintertime geopotential height and temperature fields, *Geophys. Res. Lett.*, *25*(9), 1297–1300, doi:10.1029/98GL00950.

Thordarson, Th., and S. Self (2003), Atmospheric and environmental effects of the 1783–1784 Laki eruption: A review and reassessment, *J. Geophys. Res.*, *108*(D1), 4011, doi:10.1029/2001JD002042.

Tie, X., and G. Brasseur (1995), The response of stratospheric ozone to volcanic eruptions: Sensitivity to atmospheric chlorine loading, *Geophys. Res. Lett.*, *22*(22), 3035–3038.

Tilmes, S., et al. (2013), The hydrological impact of geoengineering in the Geoengineering Model Intercomparison Project (GeoMIP). *J. Geophys. Res. Atmos.*, *118*, 11,036-11,058, doi:10.1002/jgrd.50868.

Timmreck, C. (2012), Modeling the climatic effects of large explosive volcanic eruptions, *Wiley Interdiscip. Rev. Clim. Change*, *3*, 545–564, doi:10.1002/wcc.192.

Toohey, M., K. Krüger, U. Niemeier, and C. Timmreck (2011), The influence of eruption season on the global aerosol evolution and radiative impact of tropical volcanic eruptions, *Atmos. Chem. Phys.*, *11*, 12351-12367, doi: 10.5194/acp-11-12351-2011.

Toohey, M. K. Krüger, and C. Timmreck (2013), Volcanic sulfate deposition to

Greenland and Antarctica: A modeling sensitivity study, *J. Geophys. Res. Atmos.*, *118*, 4788-4800, doi: 10.1002/jgrd.50428.

Toohey, M., K. Krüger, M. Bittner, C. Timmreck, and H. Schmidt (2014), The impact of volcanic aerosol on the Northern Hemisphere stratospheric polar vortex: mechanisms and sensitivity to forcing structure, *Atmos. Chem. Phys.*, *14*(11), 13063–13079, doi:10.5194/acp-14-13063-2014.

Toohey, M., K. Krüger, M. Sigl, F. Stordal, and H. Svensen (2016), Climatic and societal impacts of a volcanic double event at the dawn of the Middle Ages, *Climatic Change*, *136*, 401–412, doi:10.1007/s10584-016-1648-7.

Uppala, S. M., et al. (2005), The ERA-40 re-analysis, *Q. J. R. Meteorol. Soc., 131*(612), 2961–3012, doi:10.1256/qj.04.176.

Vehkamaki, H., M. Kulmala, I. Napari, K. Lehtinen, C. Timmreck, M. Noppel, and A. Laaksonen (2002), An improved parameterization for sulfuric acid-water nucleation rates for tropospheric and stratospheric conditions, *J. Geophys. Res.*, *107*(D22), 4622, doi:10.1029/2002JD002184.

Voldoire, A. et al. (2012), The CNRM-CM5.1 global climate model: description and basic evaluation, *Climate Dynamics*, *40*(9-10), 2091–2121, doi:10.1007/s00382-011-1259-y.

Volney, M. C.-F. (1788), *Travels Through Syria and Egypt, in the Years 1783, 1784, and 1785*, vol. 1, 258 pp., Burnet, White, Byrne, W. Porter, Moore and Dornin, Dublin.

Wahl, E. R., H. F. Diaz, J. E. Smerdon, and C. M. Ammann (2014), Late winter temperature response to large tropical volcanic eruptions in temperate western North America: Relationship to ENSO phases, *Global Planet. Change*, *122*, 238–250.

Wang, S.-W., and Z.-C. Zhao (1981), Droughts and floods in China, 1470–1979, in *Climate and History: Studies in Past Climates and Their Impact on Man*, edited by T. M. L. Wigley, M. J. Ingram, and G. Farmer, pp. 271–288, Cambridge Univ. Press, New York.

Washington, W. M., J. W. Weatherly, G. A. Meehl, A. J. Semtner, T. W. Bettge, A. P. Craig, W. G. Strand, J. M. Arblaster, V. B. Wayland, R. James, and J. Zhang (2000), Parallel climate model (PCM) control and transient simulations, *Clim. Dyn.*, *16*, 755–774.

Watanabe, S. et al. (2010), Improved climate simulation by MIROC5: mean states, variability, and climate sensitivity, *J. Climate*, *23*, 6312-6335, doi: 10.1175/2010JCLI3679.1.

Watanabe, S. et al. (2011), MIROC-ESM 2010: model description and basic results of CMIP5-20c3m experiments, *Geosci. Model Dev.*, *4*(4), 845–872, doi:10.5194/gmd-4-845-2011.

Wood, C. A. (1992), Climatic effects of the 1783 Laki eruption, in *The Year Without a Summer?*, edited by C. R. Harington, pp. 58–77, Can. Mus. of Nature, Ottawa.

Wu, T. et al. (2013), Global carbon budgets simulated by the Beijing Climate Center Climate System Model for the last century, *J. Geophys. Res. Atmos.*, *118*(10), 4326–4347, doi:10.1002/jgrd.50320.

Xu, Q. (1988), The abnormally cold summers of central China and their relation to volcanic eruptions, in *Aerosols and Climate*, edited by P. V. Hobbs and M. McCormick, pp. 223–231, A. Deepak, Hampton, Va.

Yue, G. K., R. E. Veiga, and P.-H. Wang (1994), SAGE II observa- tions of a previously unreported stratospheric volcanic aerosol cloud in the northern polar summer of 1980, *Geophys. Res. Lett.*, *21*, 429–432.

Yukimoto, S. et al. (2012), A New Global Climate Model of the Meteorological Research Institute: MRI-CGCM3 Model Description and Basic Performance, *J. Meteorol. Soc. Japan*, *90A*, 23–64, doi:10.2151/jmsj.2012-A02.

Zambri, B., and A. Robock (2016), Winter warming and summer monsoon reduction after volcanic eruptions in Coupled Model Intercomparison Project 5 (CMIP5) simulations. *Geophys. Res. Lett., 43*, 10,920-10,928, doi:10.1002/2016GL070460.

Zambri, B., A. N. LeGrande, A. Robock, and J. Slawinska (2017), Northern Hemisphere Winter Warming and Summer Monsoon Reduction after Volcanic Eruptions over the Last Millennium, *J. Geophys. Res. Atmos.*, *122*, doi:10.1002/2017JD026728.

Zanchettin, D. et al. (2016), The Model Intercomparison Project on the climatic response to Volcanic forcing (VolMIP): Experimental design and forcing input data for CMIP6, *Geosci. Model Dev.*, *9*, 2701–2719, doi:10.5194/gmd-9-2701-2016.

Zhao, J., R. P. Turco, and O. B. Toon (1995), A model simulation of Pinatubo volcanic aerosols in the stratosphere, *J. Geophys. Res.*, *100*, 7315–7328.

Zuo, J.-Q., W.-J. Li, and H.-L. Ren (2013), Representation of the Arctic Oscillation in the CMIP5 models, *Adv. Clim. Change Res.*, *4*(4), doi:10.3724/SP.J.1248.2013.242.

Table 2.1 CMIP5 models used.

Model	**Resolution (°) (lat x lon)**	**Vertical Levels**	**Forcing Data Set**	**Number of Ensemble Members**
ACCESS1-3[A]	1.25 x 1.875	38	*Sato et al.* [1993]	3
bcc-csm1-1[B]	2.8 x 2.8	26	*Ammann et al.* [2003]	3
bcc-csm1-1-m[B]	1.11 x 1.125	26	*Ammann et al.* [2003]	3
CanESM2[C]	2.8 x 2.8	35	*Sato et al.* [1993]	5
CESM1-CAM5[D]	0.94 x 1.25	26	*Amman et al.* [2007]	3
CESM1-FASTCHEM[D]	0.94 x 1.25	26	*Amman et al.* [2007]	3
CCSM4[E]	0.94 x 1.25	26	*Amman et al.* [2007]	8
CNRM-CM5[F]	1.4 x 1.4	31	*Amman et al.* [2007]	10
CSIRO-Mk3-6-0[G+]	1.865 x 1.875	18	*Sato et al.* [1993]	10
GFDL-CM2p1[H]	2 x 2.5	24	*Sato et al.* [1993] and *Stenchikov et al.* [1998]	10
GFDL-CM3[I]	2 x 2.5	48	*Sato et al.* [1993] and *Stenchikov et al.* [1998]	5
GISS-E2-H[J]	2 x 2.5	40	*Sato et al.* [1993]	18
GISS-E2-R[J]	2 x 2.5	40	*Sato et al.* [1993]	18
HadCM3[K]	2.5 x 3.75	19	*Sato et al.* [1993]	10
HadGEM2-ES[L]*	1.25 x 1.875	38	*Sato et al.* [1993]	4
IPSL-CM5A-LR[M&]	1.9 x 3.75	39	*Sato et al.* [1993]	6
IPSL-CM5A-MR[M&]	1.27 x 2.5	39	*Sato et al.* [1993]	3
MIROC-ESM[N]*	2.8 x 2.8125	80	*Sato et al.* [1993]	3
MIROC5[O+]	1.4 x 1.4	40	*Sato et al.* [1993]	5
MPI-ESM-LR[P]*	1.865 x 1.875	47	*Stenchikov et al.* [1998]	3
MPI-ESM-MR[P]	1.865 x 1.875	95	*Stenchikov et al.* [1998]	3
MPI-ESM-P[P*]	1.865 x 1.875	47	*Stenchikov et al.* [1998]	2
MRI-CGCM3[Q]	1.12 x 1.125	48	Interactive	5
NorESM1-M[R]	1.9 x 2.5	26	*Amman et al.* [2007]	3

*Models excluded from 16-model analysis.

[&]Models excluded because they used insolation reduction rather than aerosols for volcanic forcing.

[+]Models excluded due to low variability in wintertime 50 hPa geopotential height and zonal wind fields.

[A]*Bi et al.* [2013]

[B]*Wu et al.* [2013]

[C]*Chylek et al.* [2011]

[D]*Hurrell et al.* [2013]

[E]*Gent et al.* [2011]

[F]*Voldoire et al.* [2012]

[G]*Rotstayn et al.* [2010]

[H]*Delworth et al.* [2006]

[I] *Donner et al.* [2011]
[J] *Schmidt et al.* [2014]
[K] *Johns et al.* [2003]
[L] *Collins et al.* [2011]
[M] *Dufresne et al.* [2013]
[N] *Watanabe et al.* [2011]
[O] *Watanabe et al.* [2010]
[P] *Giorgetta et al.* [2013]
[Q] *Yukimoto et al.* [2012]
[R] *Bentsen et al.* [2012]

Table 2.2 Volcanic eruptions analyzed. Aerosol mass is from *Gao et al.* [2008].

Volcano	**Eruption Date**	**Latitude**	**Stratospheric Sulfate Aerosol Mass (Tg)**
Krakatau	August 27,1883	6.1°S	21.9
El Chichón	April 4, 1982	17.4°N	14.0
Pinatubo	June 15, 1991	15.1°N	30.1

Table 3.1 Last millennium ensemble models, volcanic forcing data set used*, and number of ensemble members.

Model	Volcanic Forcing	Model Resolution (Lat x Lon x Lev)	Number of Ensemble Members
BCC-CSM1-1	GRA	128x64x26	1
CESM1-CAM5	GRA	144x90x26	9 all forcing, 5 volcanic only
CCSM4	GRA	288x192x26	1
CSIRO-Mk3L-1-2	CEA	64x56x18	1
FGOALS-s2	GRA	128x108x26	1
GISS-E2-R	CEA, 2xGRA	144x90x40	3 CEA, 3 2xGRA
HadCM3	CEA	96x73x19	1
MIROC-ESM	CEA	128x64x80	1
MPI-ESM-P	CEA	196x98x47	1
MRI-CGCM3	GRA, interactive	320x160x48	1

*GRA = *Gao et al.* [2008], CEA = *Crowley et al.* [2008]

Table 3.2 Volcanic eruptions analyzed from the CMIP5/PMIP3 past1000 ensemble. Aerosol mass is from *Gao et al.* [2008]. Aerosol flux is from *Crowley et al.* (2008).

Eruption Year (C.E)	Volcano	Latitude	Stratospheric Sulfate Aerosol Mass (Tg)	Total Sulfate Aerosol Flux (kg km^{-2})
1167[G]	Kirishima	31°N	52.12	10.9
1227	Zaozan	38°N	67.52	51.2
1258	Samalas	8°S	257.91	196.9
1275[G]	Quilotoa	1°S	63.72	10
1284	Unidentified	?	54.69	15.1
1452	Kuwae	17°S	137.50	59.1
1600	Huaynaputina	17°S	56.59	45.7
1641[G]	Parker	6°N	51.60	17.6
1673[C]	Gamkonora	1°N	16.13	20.1
1694[C]	Unidentified	?	27.1	28.3
1809	Unidentified	?	53.74	40.6
1815	Tambora	8°S	109.72	84.8
1835[C]	Cosigüina	13°N	40.16	22.7

[C]Volcano was used only in CEA-forced runs.
[G]Volcano was used only in GRA-forced runs.
Eruptions in years without a superscript were analyzed for all runs.

Table 4.1 Date of eruptions and SO_2 emissions for the ten stratospheric eruption episodes of Laki [*Thordarson and Self*, 2003].

Date	SO_2 (Tg)
June 8, 1783	8.3
June 11, 1783	13.5
June 14, 1783	18.7
June 27, 1783	10.8
July 9, 1783	8.9
July 29, 1783	13.2
August 31, 1783	7.7
September 9, 1783	5.9
September 26, 1783	4.4
October 25, 1783	2.9

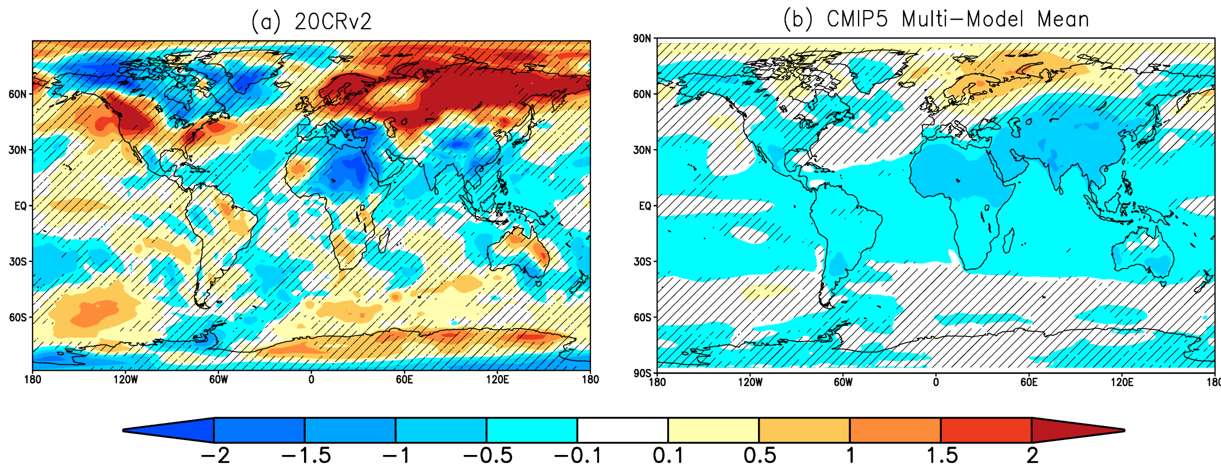

Figure 2.1 Surface temperature anomalies with respect to the five years preceding each eruption (K) for the first winter (DJF) after the 1883 Krakatau and 1991 Pinatubo eruptions for (a) 20CRv2 reanalysis and (b) CMIP5 model mean. Hatching displays (a) areas below 90% significance and (b) areas where fewer than 15 of 20 models agree on the sign of the anomaly.

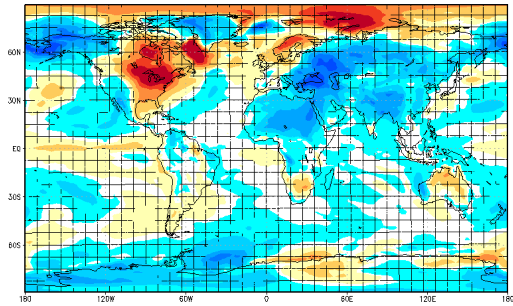

ACCESS1-3

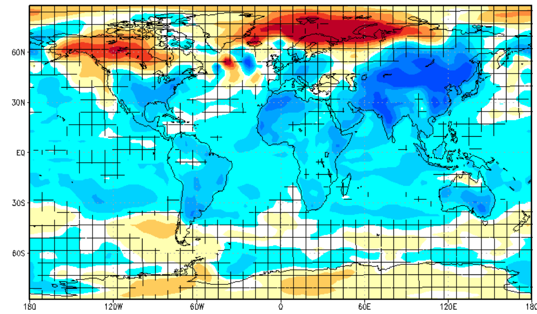

bcc-csm1-1

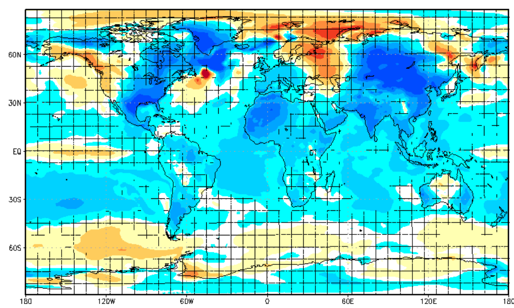

bcc-csm1-1-m

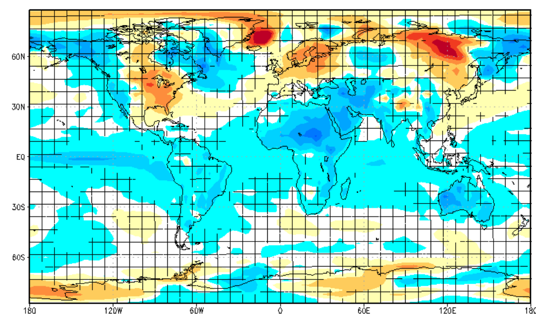

CanESM2

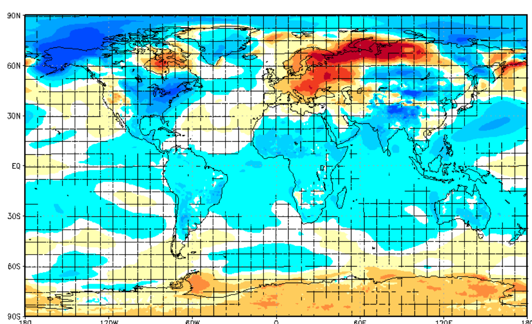

CESM1-CAM5

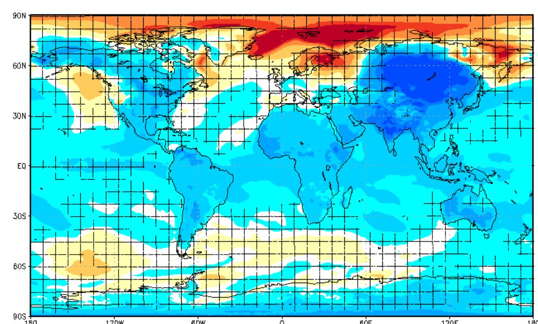

CESM1-FASTCHEM

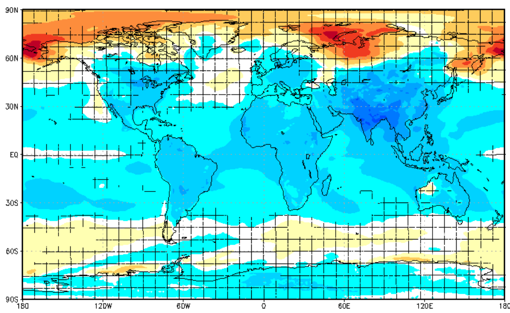

CCSM4

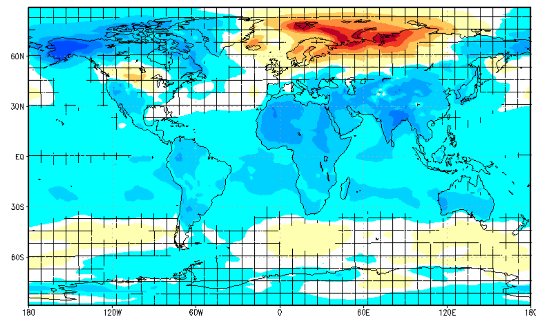

CNRM-CM5

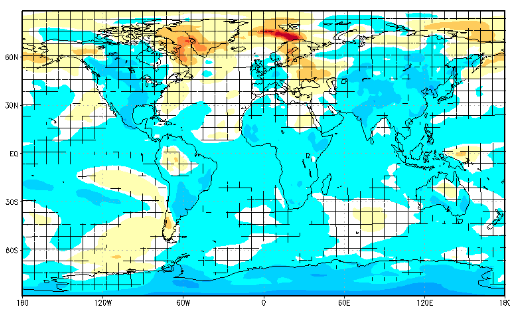

CSIRO-Mk3-6-0

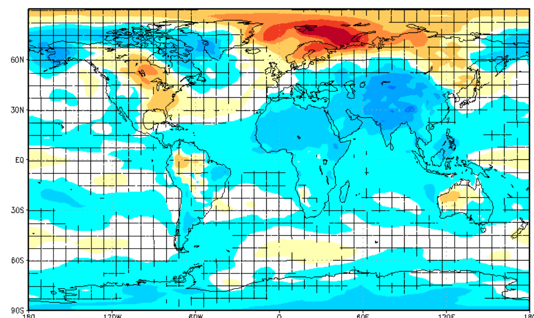

GFDL-CM2p1

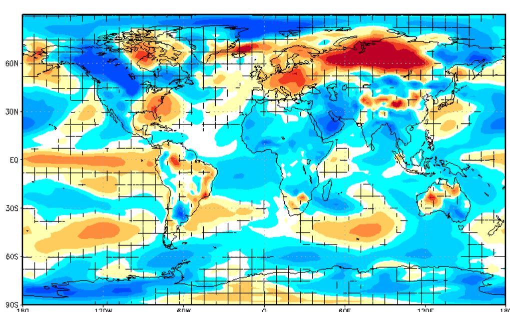

GFDL-CM3

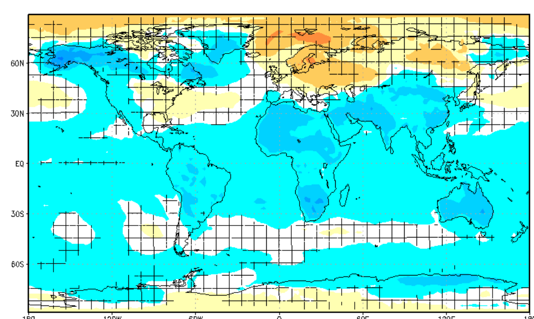

GISS-E2-H

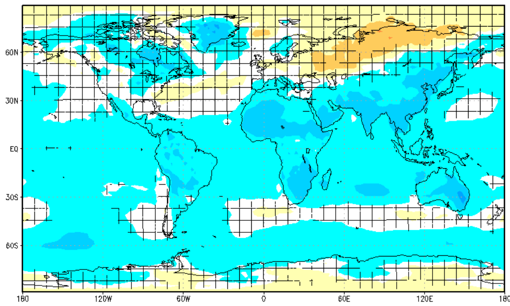

GISS-E2-R

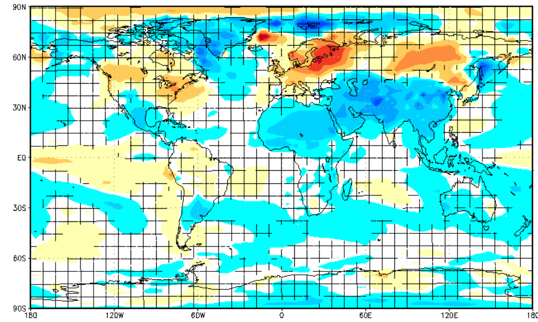

HadCM3

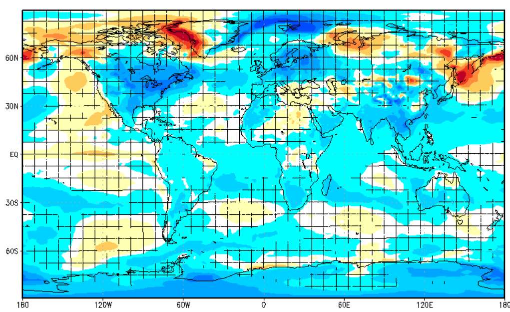

HadGEM2-ES

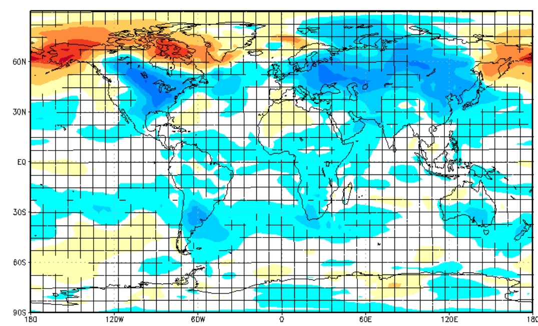

IPSL-CM5A-LR

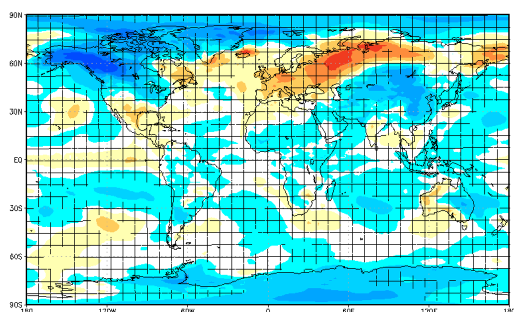

IPSL-CM5A-MR

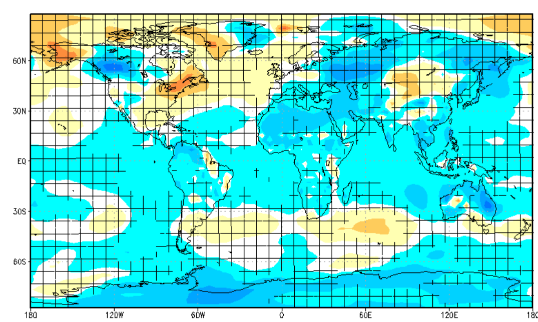

MIROC-ESM

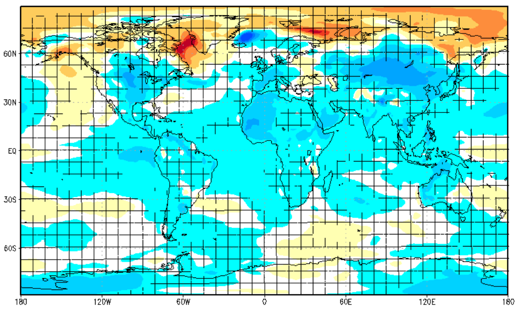

MIROC5

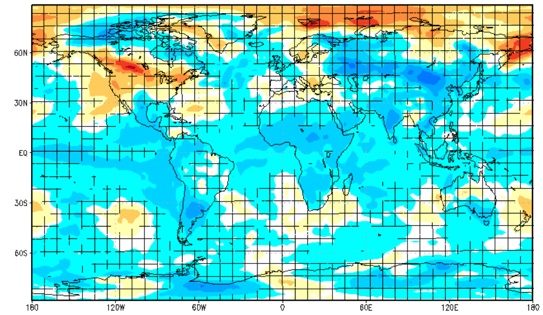

MPI-ESM-LR

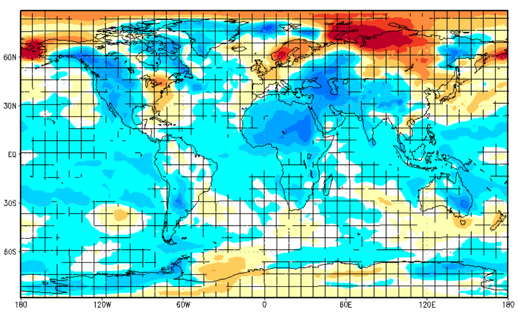

MPI-ESM-MR

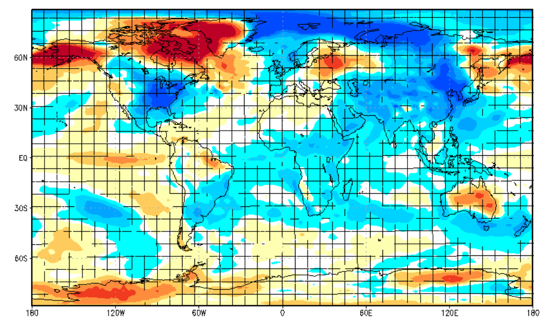

MPI-ESM-P

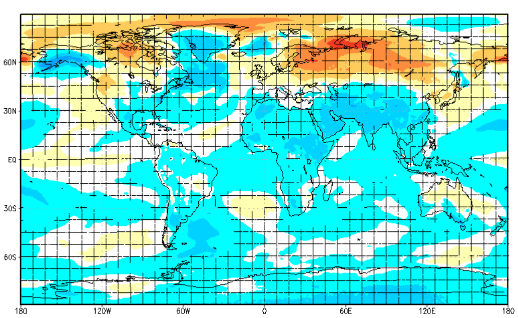

MRI-CGCM3

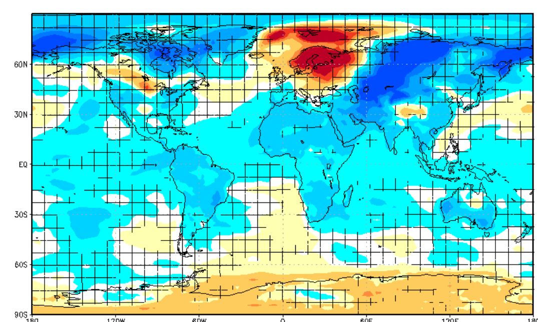

NorESM1-M

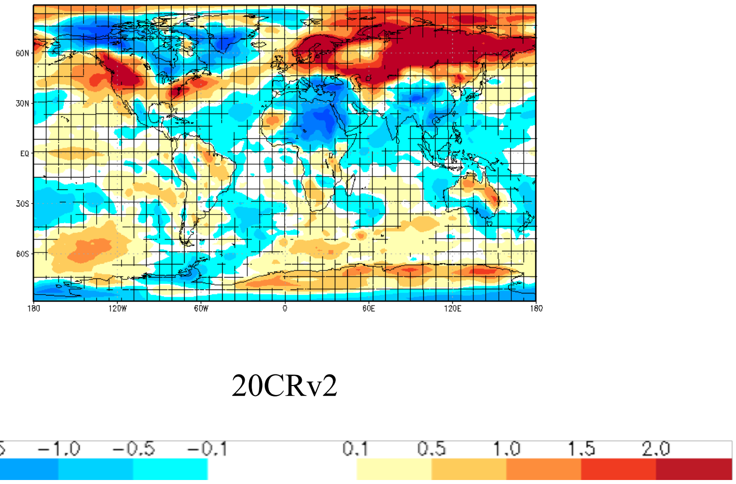

Figure 2.2 Composite surface temperature anomalies with respect to the five years preceding each eruption (K) for the first winter (DJF) after the 1883 Krakatau and 1991 Pinatubo eruptions for CMIP5 individual model means and 20CRv2 reanalysis. Hatching displays areas below 90% significance using a bootstrapping method (n = 5000).

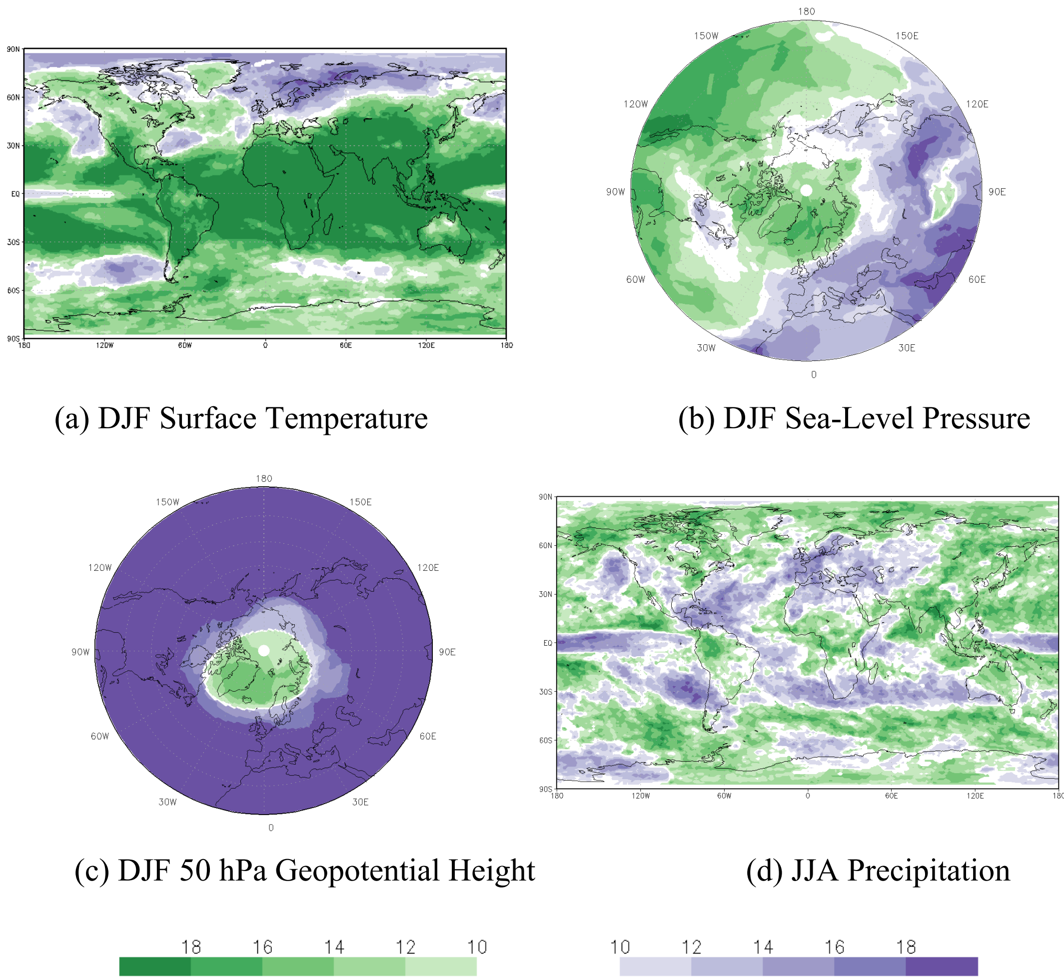

Figure 2.3 CMIP5 multi-model agreement for mean of the simulations of the response to the 1883 Krakatau and 1991 Pinatubo eruptions for each of the 20 models listed in Table 2.1. Purple indicates the number of models that agree on a positive anomaly; green indicates the number of models that agree on a negative anomaly.

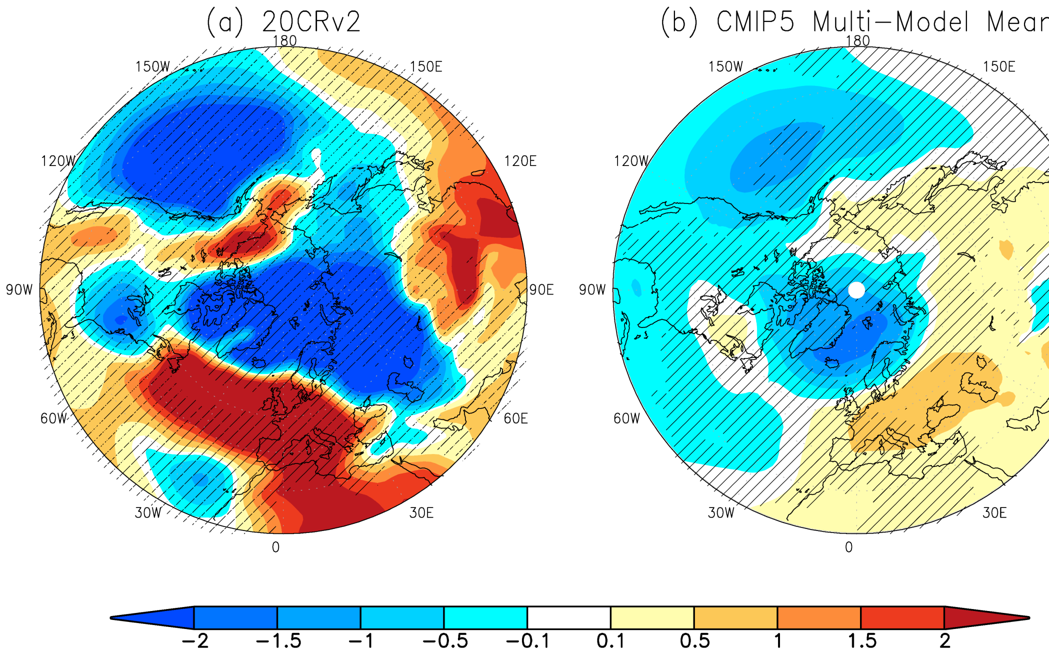

Figure 2.4 Sea level pressure anomalies with respect to the five years preceding each eruption (hPa) for the first winter (DJF) after the 1883 Krakatau and 1991 Pinatubo eruptions for (a) 20CRv2 reanalysis and (b) CMIP5 model mean. Hatching displays (a) areas below 90% significance and (b) areas where fewer than 15 of 20 models agree on the sign of the anomaly.

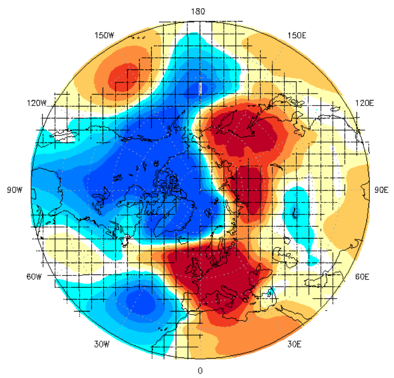

ACCESS1-3

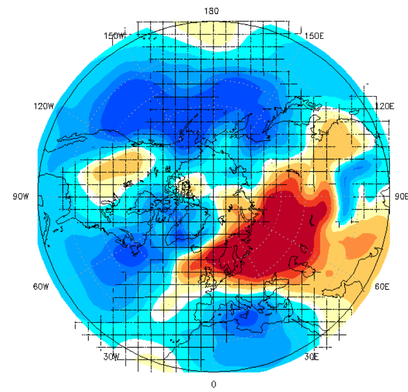

bcc-csm1-1

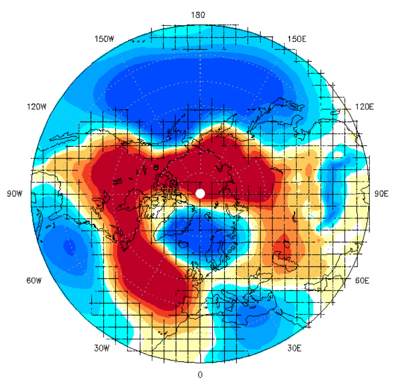

bcc-csm1-1-m

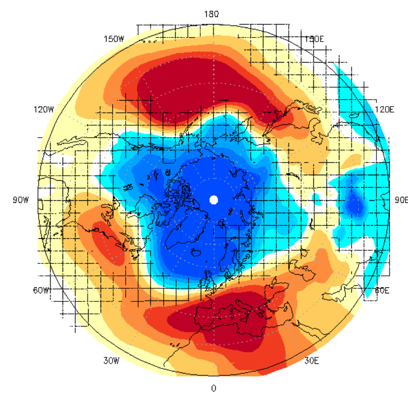

CanESM2

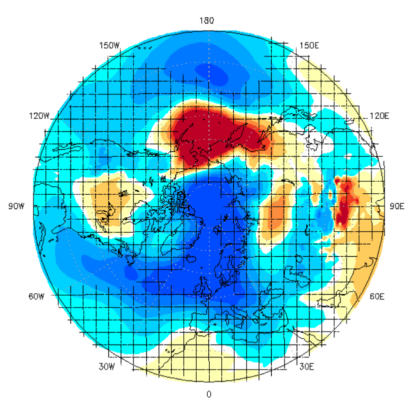

CESM1-CAM5

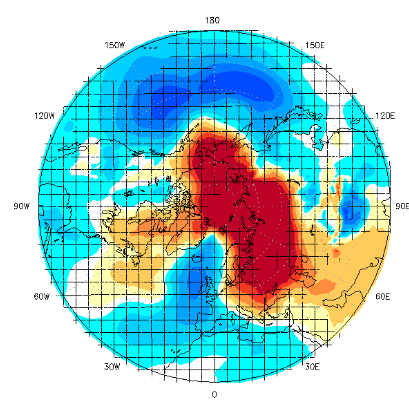

CESM1-FASTCHEM

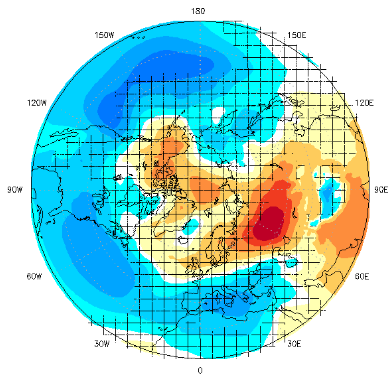

CCSM4

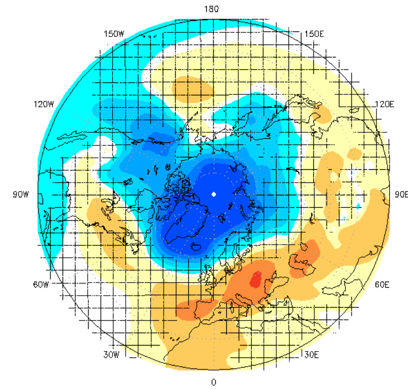

CNRM-CM5

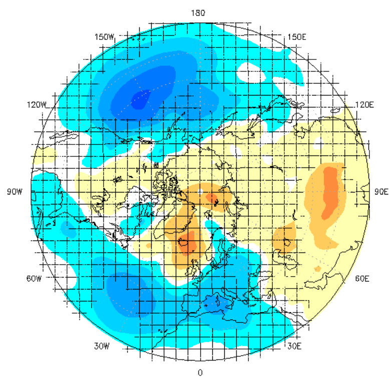

CSIRO-Mk3-6-0

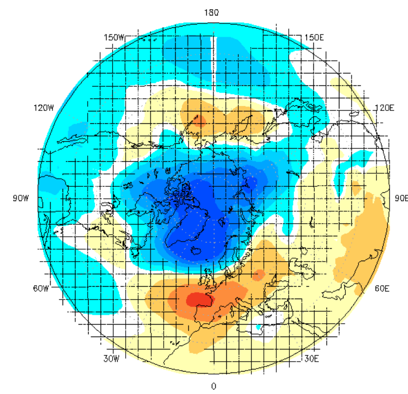

GFDL-CM2p1

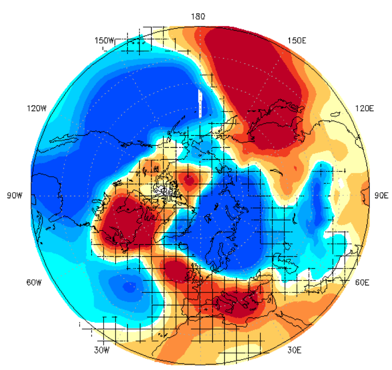

GFDL-CM3

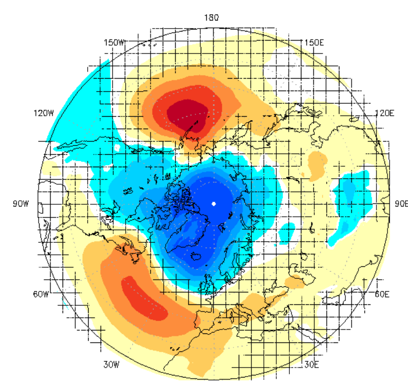

GISS-E2-H

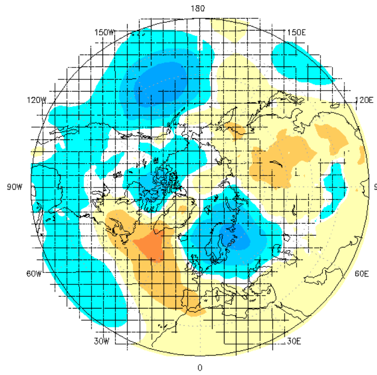

GISS-E2-R

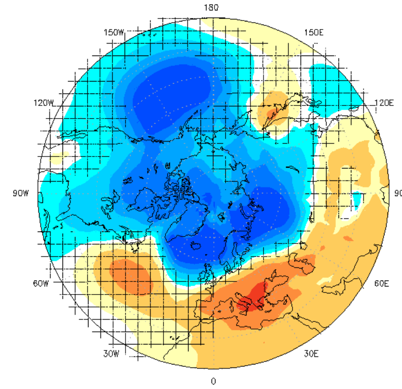

HadCM3

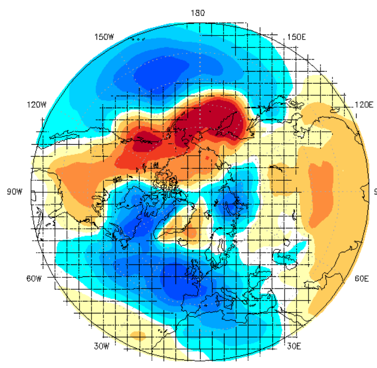

HadGEM2-ES

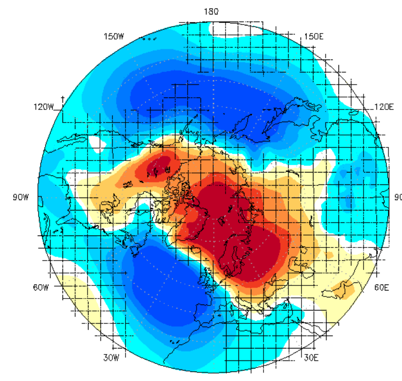

IPSL-CM5A-LR

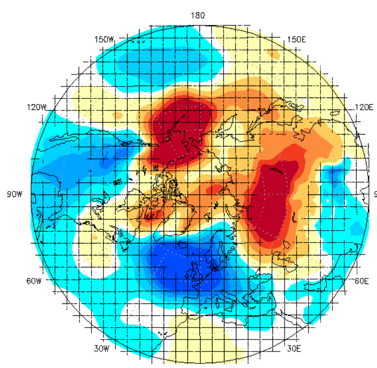

IPSL-CM5A-MR

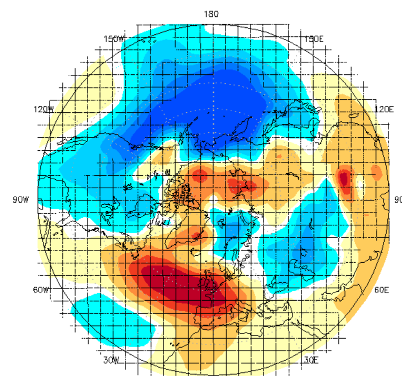

MIROC-ESM

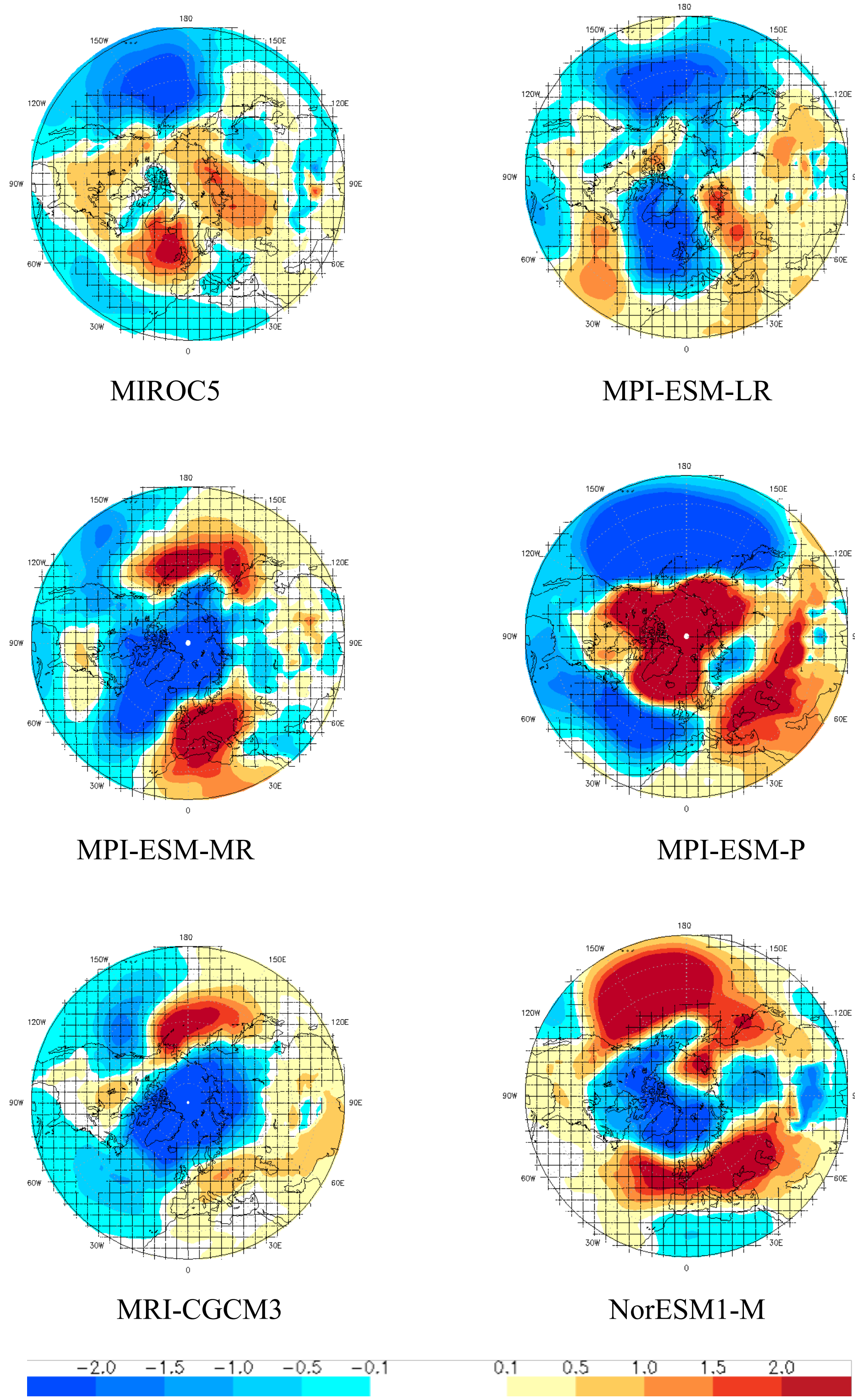
MIROC5
MPI-ESM-LR
MPI-ESM-MR
MPI-ESM-P
MRI-CGCM3
NorESM1-M
−2.0 −1.5 −1.0 −0.5 −0.1 0.1 0.5 1.0 1.5 2.0

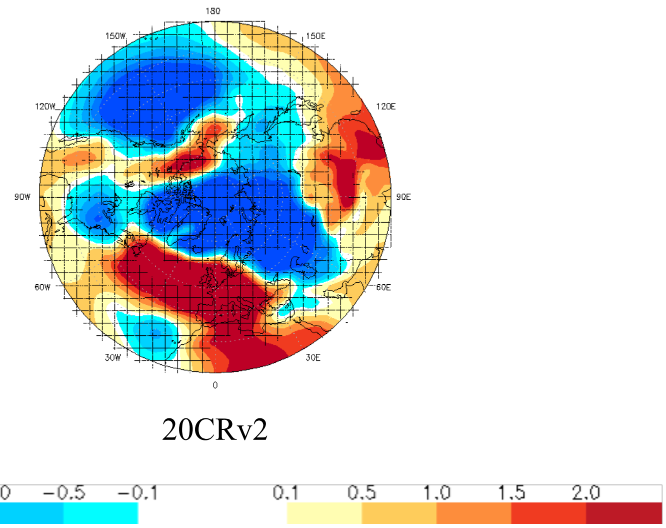

Figure 2.5 Composite sea-level pressure anomalies with respect to the five years preceding each eruption (hPa) for the first winter (DJF) after the 1883 Krakatau and 1991 Pinatubo eruptions for CMIP5 individual model means and 20CRv2 reanalysis. Hatching displays areas below 90% significance using a bootstrapping method (n = 5000).

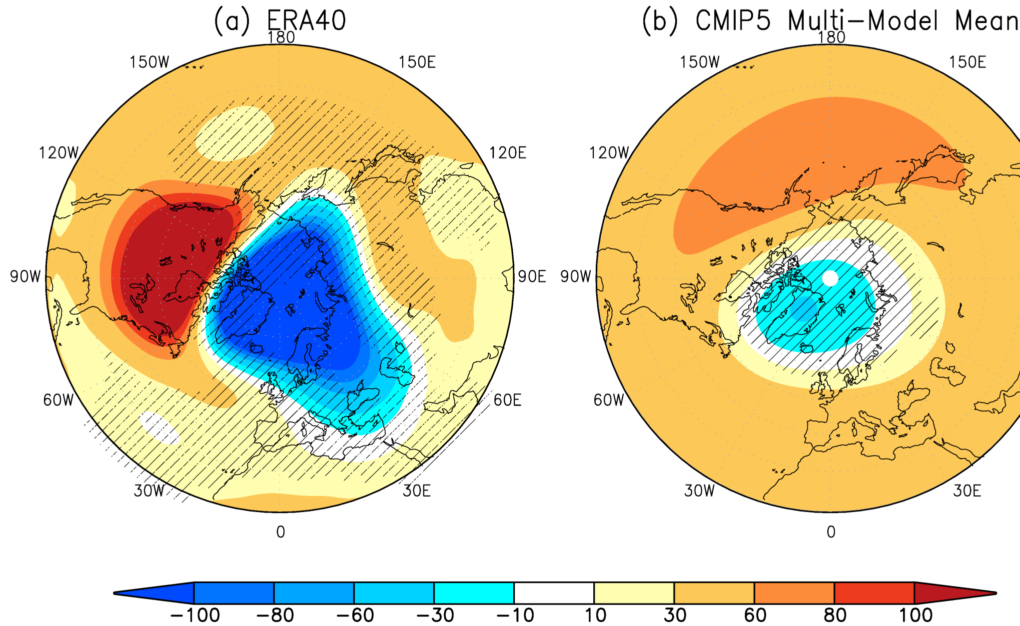

Figure 2.6 Geopotential height anomalies with respect to the five years preceding each eruption at 50 hPa (m) for the first winter (DJF) after the 1982 El Chichón and 1991 Pinatubo eruptions for (a) ERA40 reanalysis and (b) CMIP5 model mean. Hatching displays (a) for areas below 90% significance and (b) areas where fewer than 15 of 20 models agree on the sign of the anomaly.

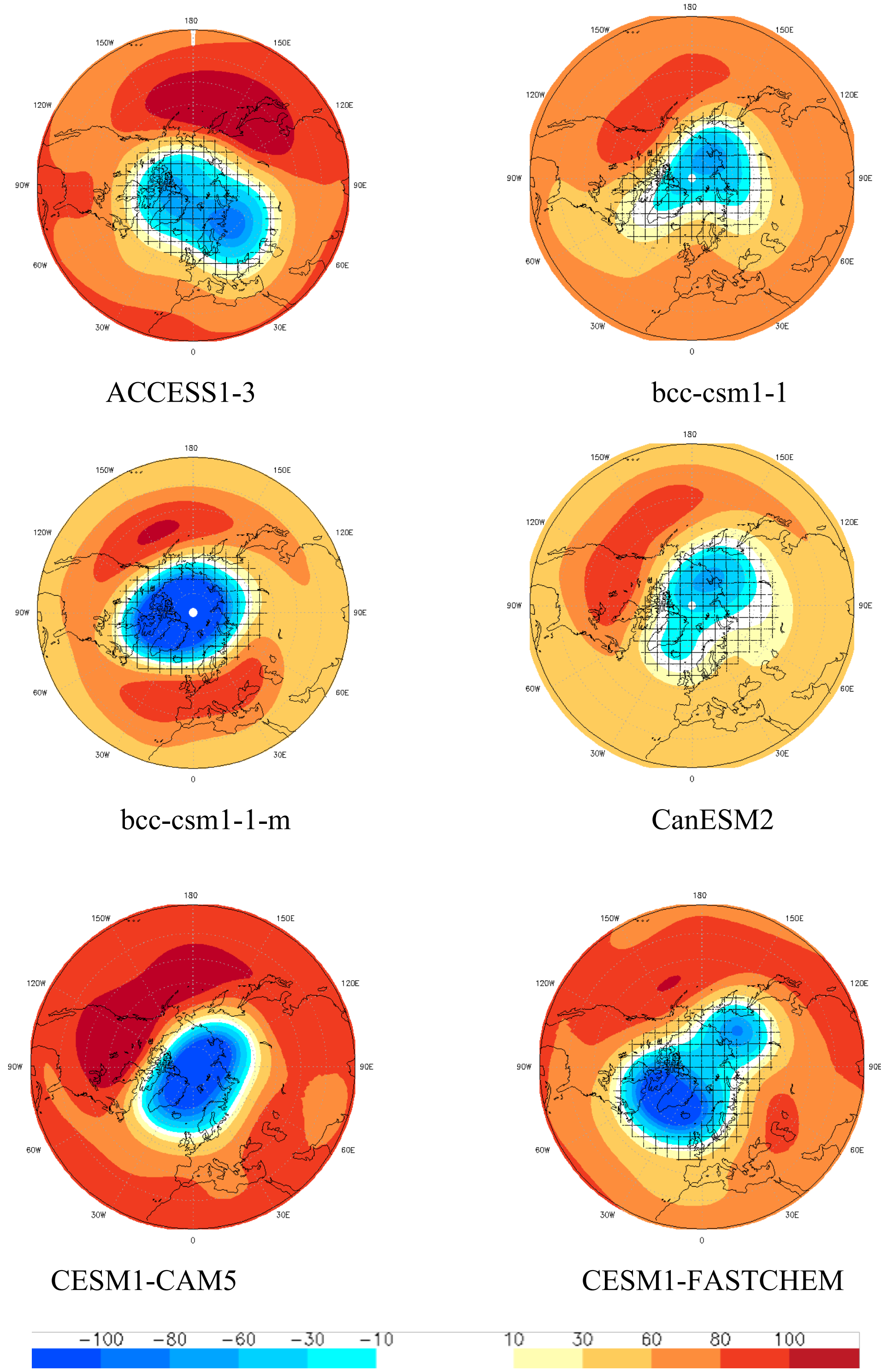
ACCESS1-3
bcc-csm1-1
bcc-csm1-1-m
CanESM2
CESM1-CAM5
CESM1-FASTCHEM
−100 −80 −60 −30 −10 10 30 60 80 100

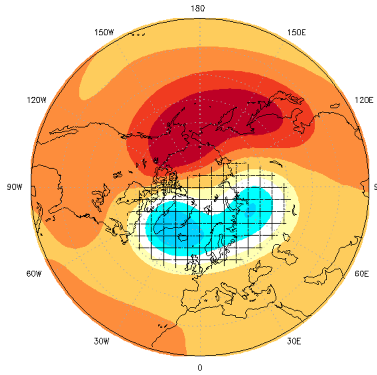

CCSM4

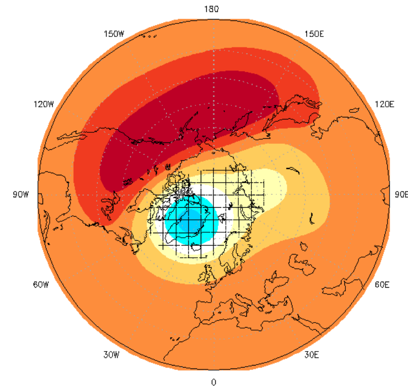

CNRM-CM5

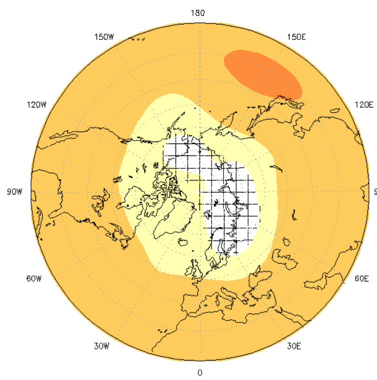

CSIRO-Mk3-6-0

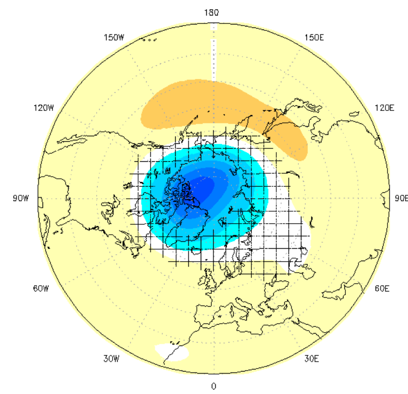

GFDL-CM2p1

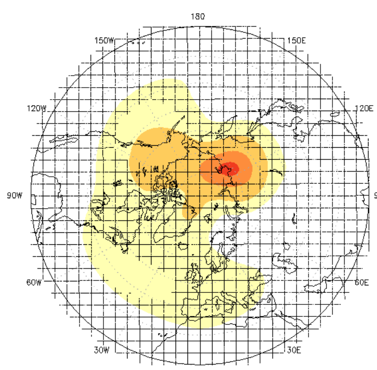

GFDL-CM3

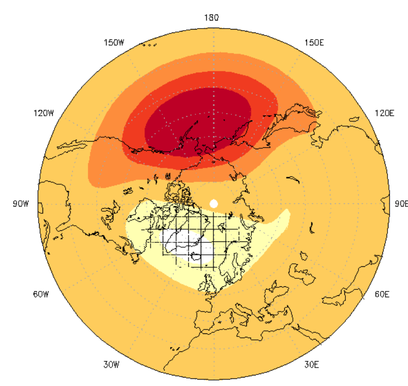

GISS-E2-H

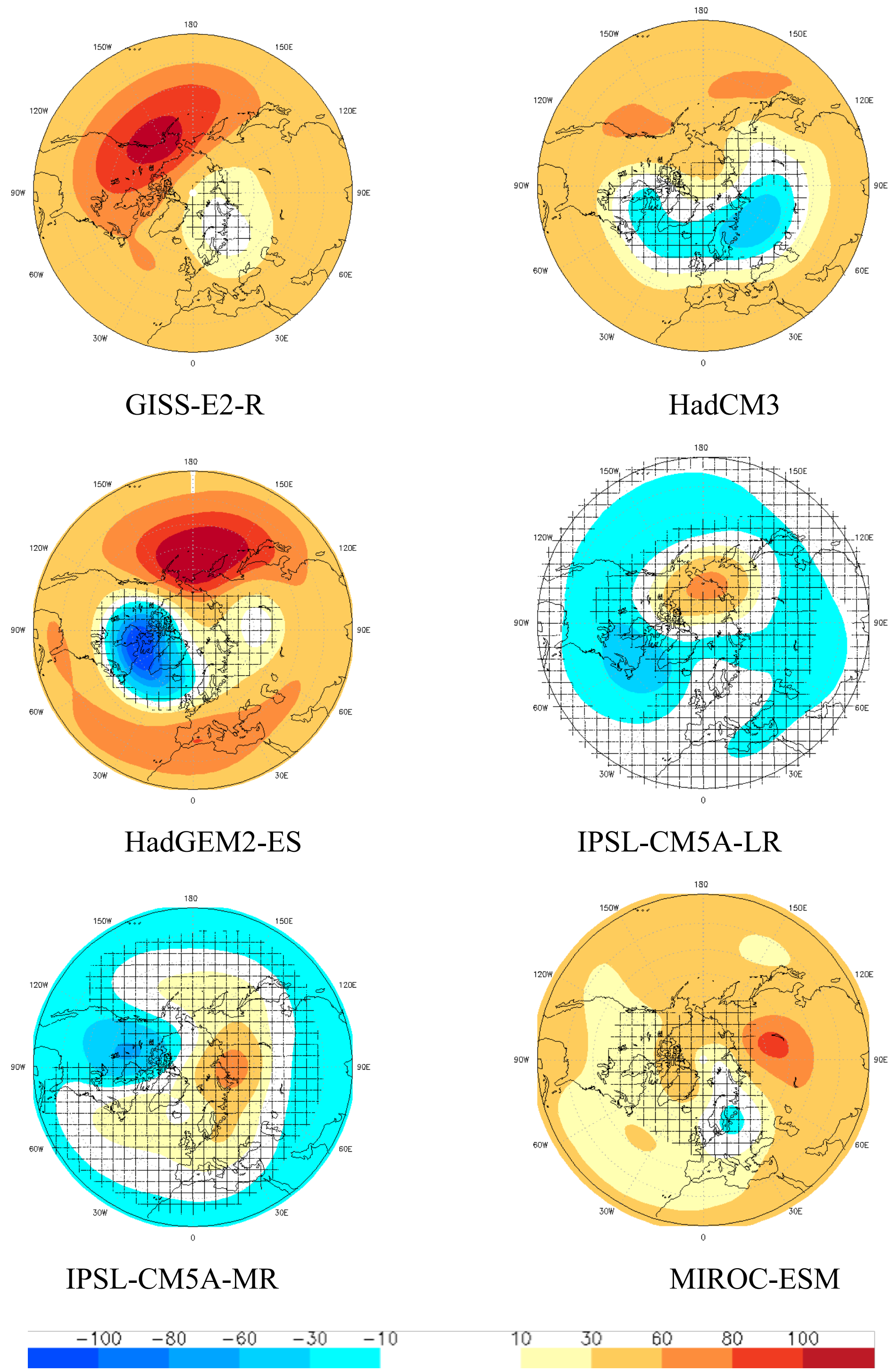
GISS-E2-R
HadCM3
HadGEM2-ES
IPSL-CM5A-LR
IPSL-CM5A-MR
MIROC-ESM
−100 −80 −60 −30 −10
10 30 60 80 100

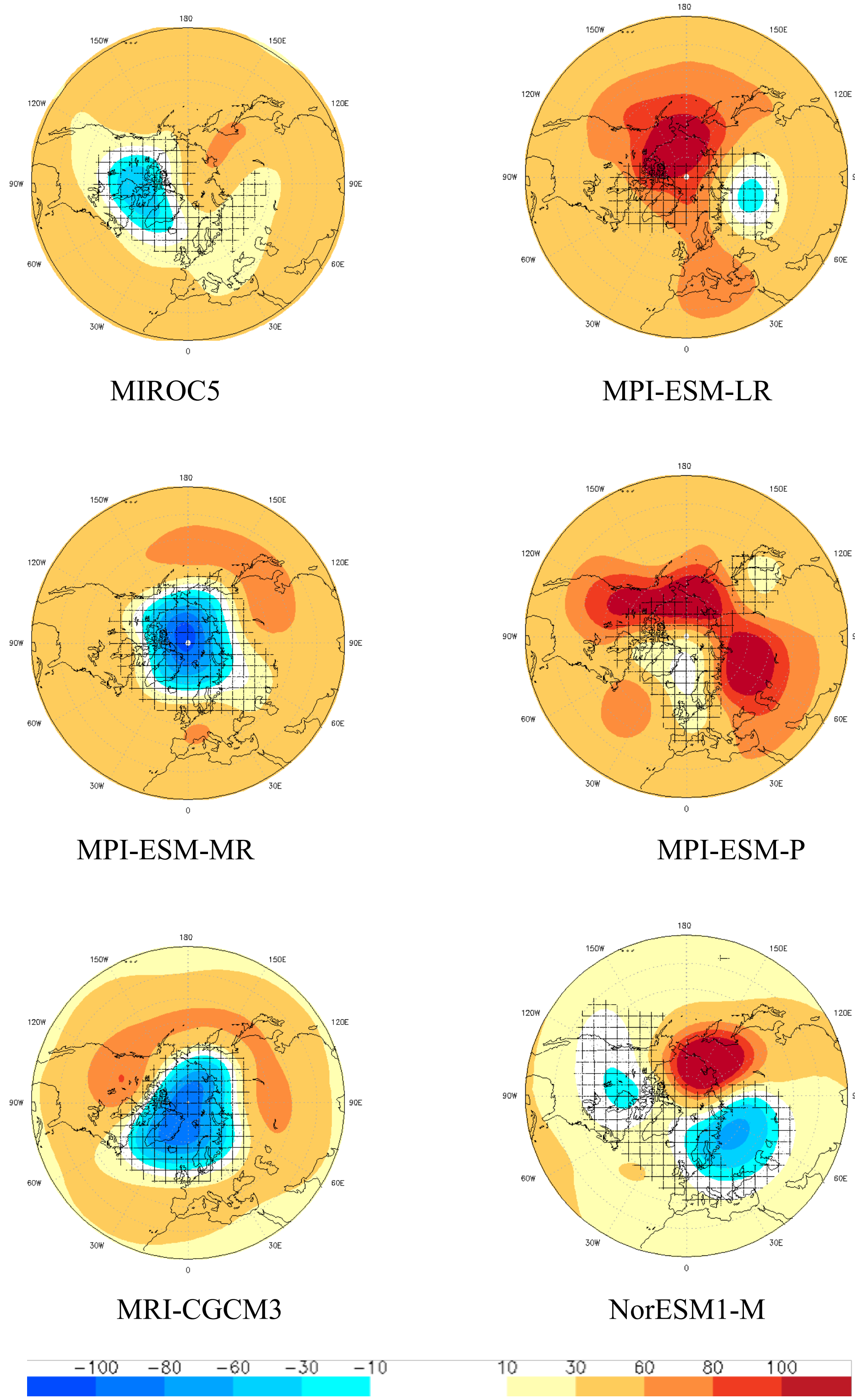
MIROC5
MPI-ESM-LR
MPI-ESM-MR
MPI-ESM-P
MRI-CGCM3
NorESM1-M
−100 −80 −60 −30 −10 10 30 60 80 100

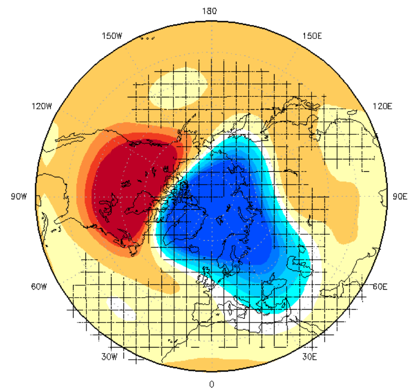

ERA40

Figure 2.7 50 hPa geopotential height anomalies with respect to the five years preceding each eruption (m) for the first winter (DJF) after the 1982 El Chichón and 1991 Pinatubo eruptions for CMIP5 individual model means and ERA40 reanalysis. Hatching displays areas below 90% significance using a bootstrapping method (n = 5000).

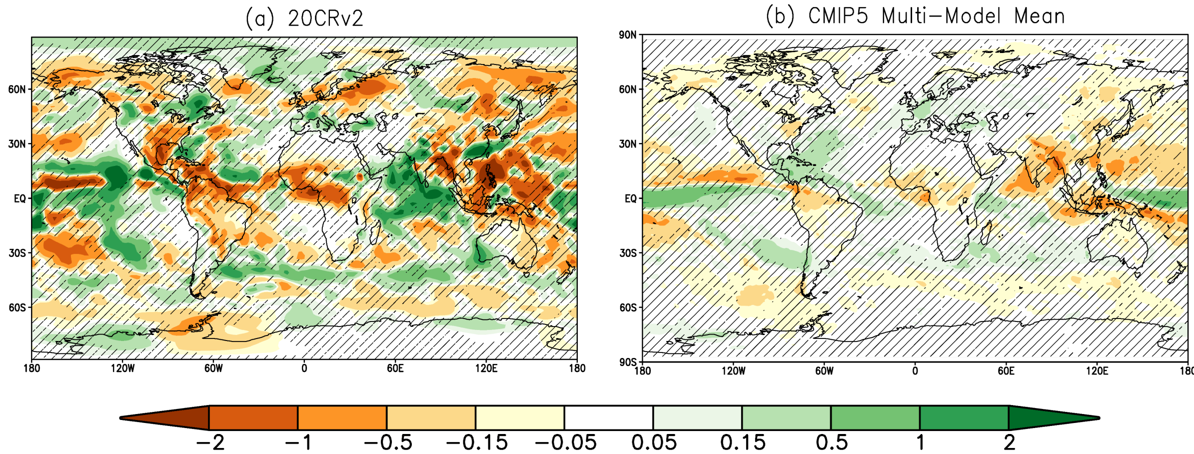

Figure 2.8 Precipitation anomalies with respect to the five years preceding each eruption (mm/day) for the first summer (JJA) after the 1883 Krakatau and 1991 Pinatubo eruptions for (a) 20CRv2 reanalysis and (b) CMIP5 model mean. Hatching displays (a) areas below 90% significance and (b) areas where fewer than 15 of 20 models agree on the sign of the anomaly.

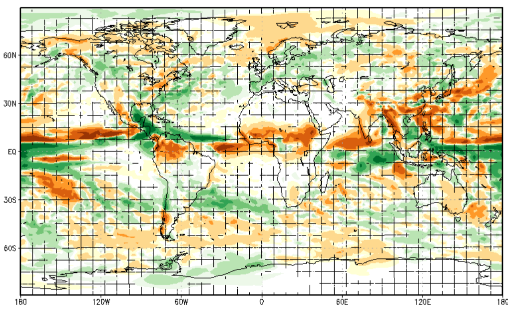

ACCESS1-3

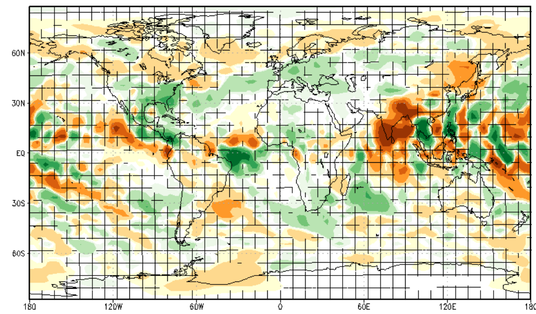

bcc-csm1-1

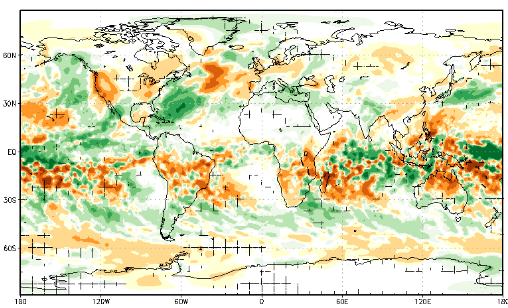

bcc-csm1-1-m

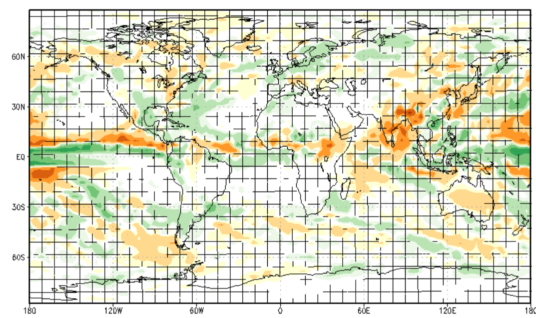

CanESM2

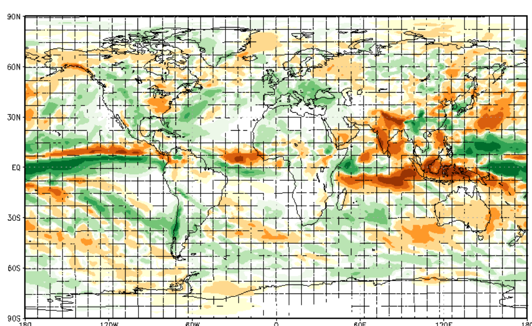

CESM1-CAM5

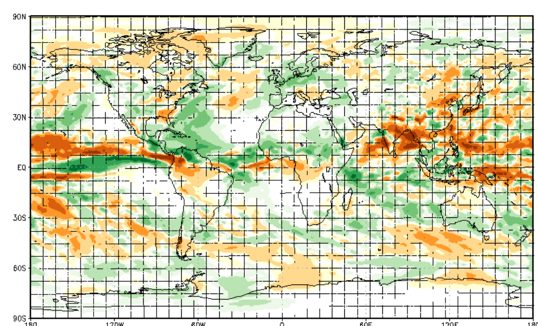

CESM1-FASTCHEM

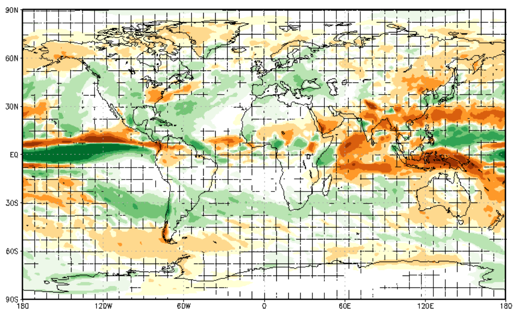

CCSM4

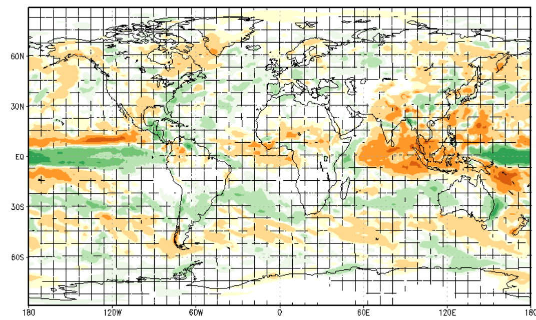

CNRM-CM5

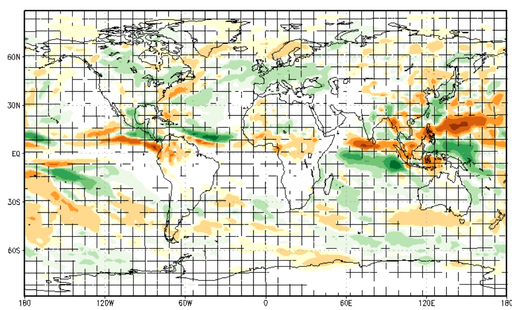

CSIRO-Mk3-6-0

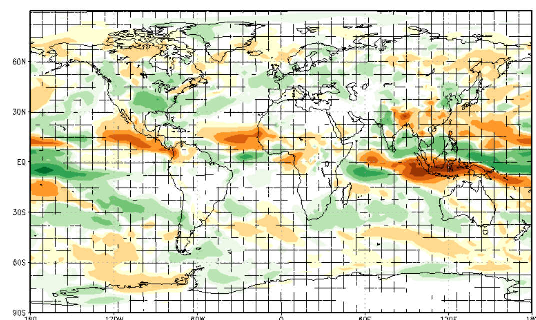

GFDL-CM2p1

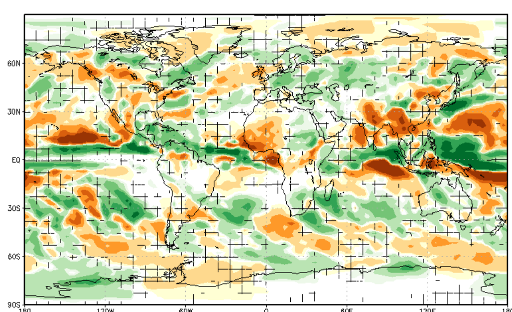

GFDL-CM3

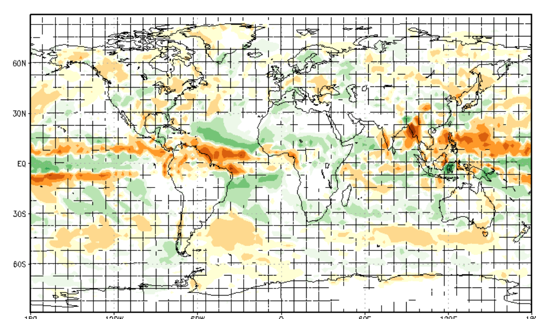

GISS-E2-H

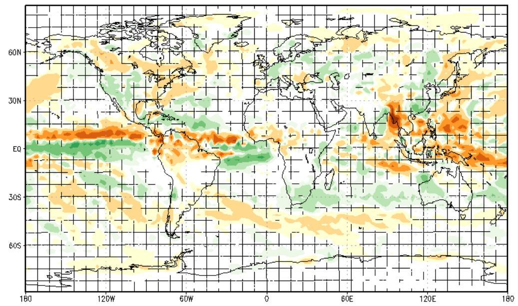

GISS-E2-R

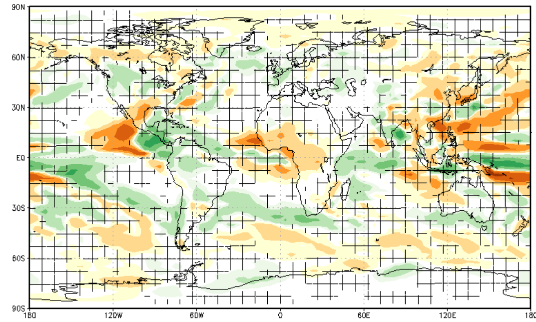

HadCM3

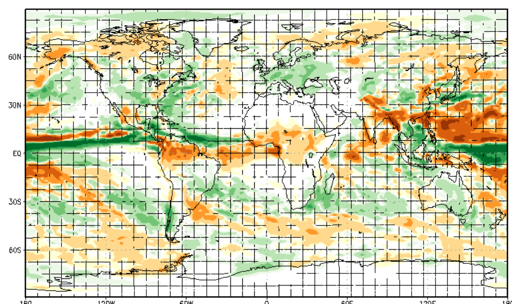

HadGEM2-ES

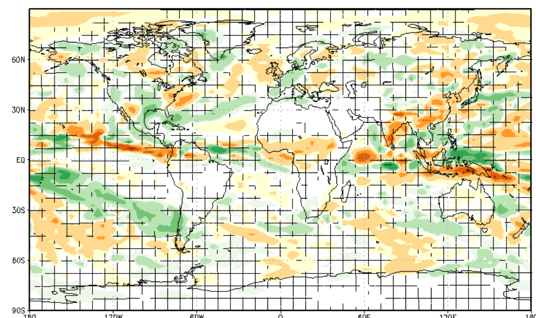

IPSL-CM5A-LR

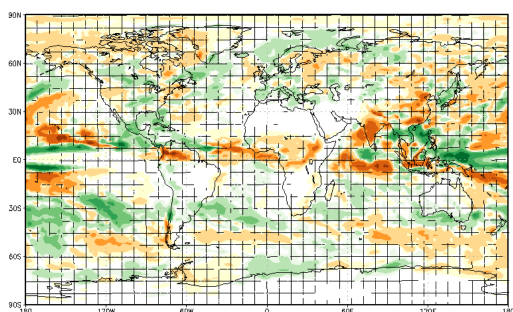

IPSL-CM5A-MR

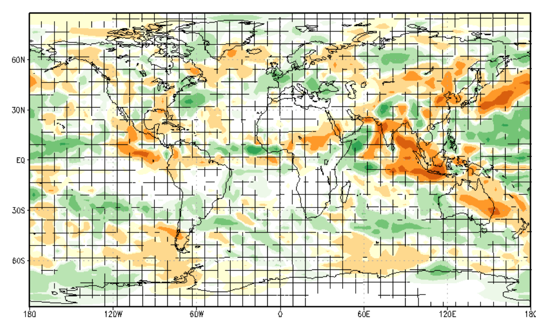

MIROC-ESM

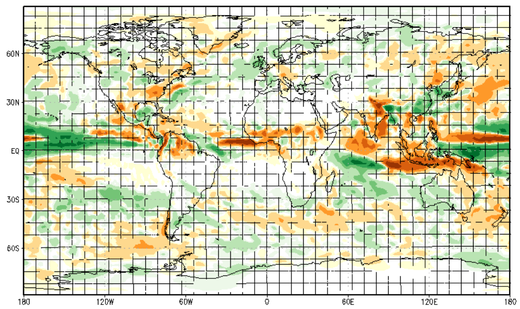

MIROC5

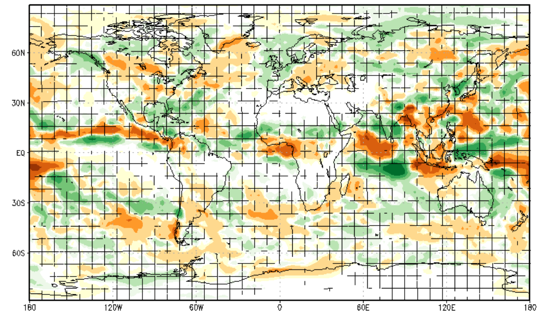

MPI-ESM-LR

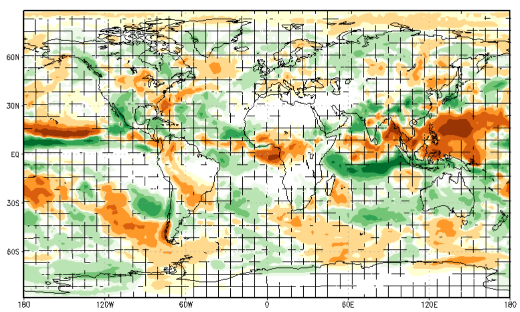

MPI-ESM-MR

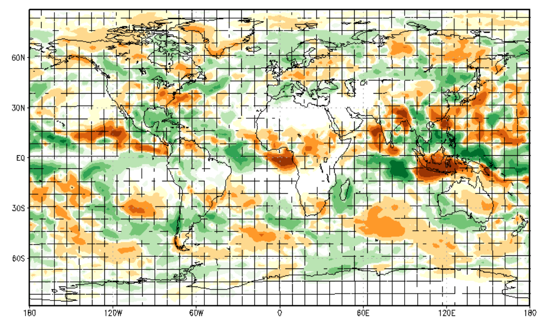

MPI-ESM-P

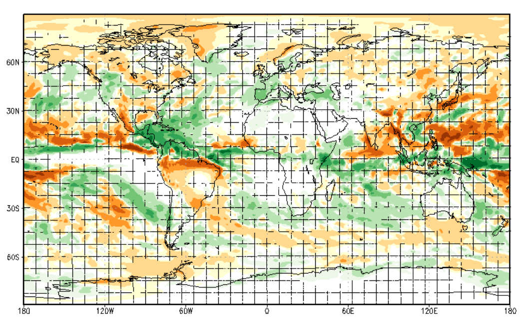

MRI-CGCM3

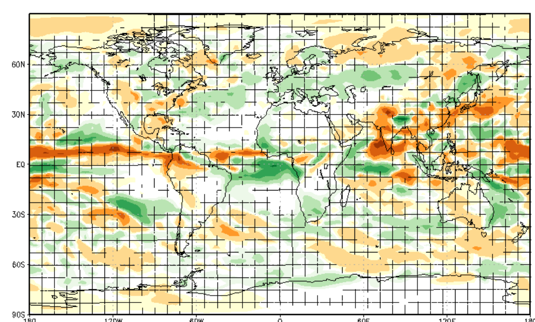

NorESM1-M

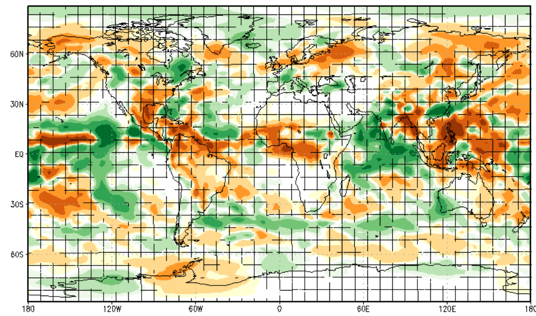

20CRv2

Figure 2.9 Composite precipitation anomalies with respect to the five years preceding each eruption (mm/day) for the first summer (JJA) after the 1883 Krakatau and 1991 Pinatubo eruptions for CMIP5 individual model means and 20CRv2 reanalysis. Hatching displays areas below 90% significance using a bootstrapping method (n = 5000).

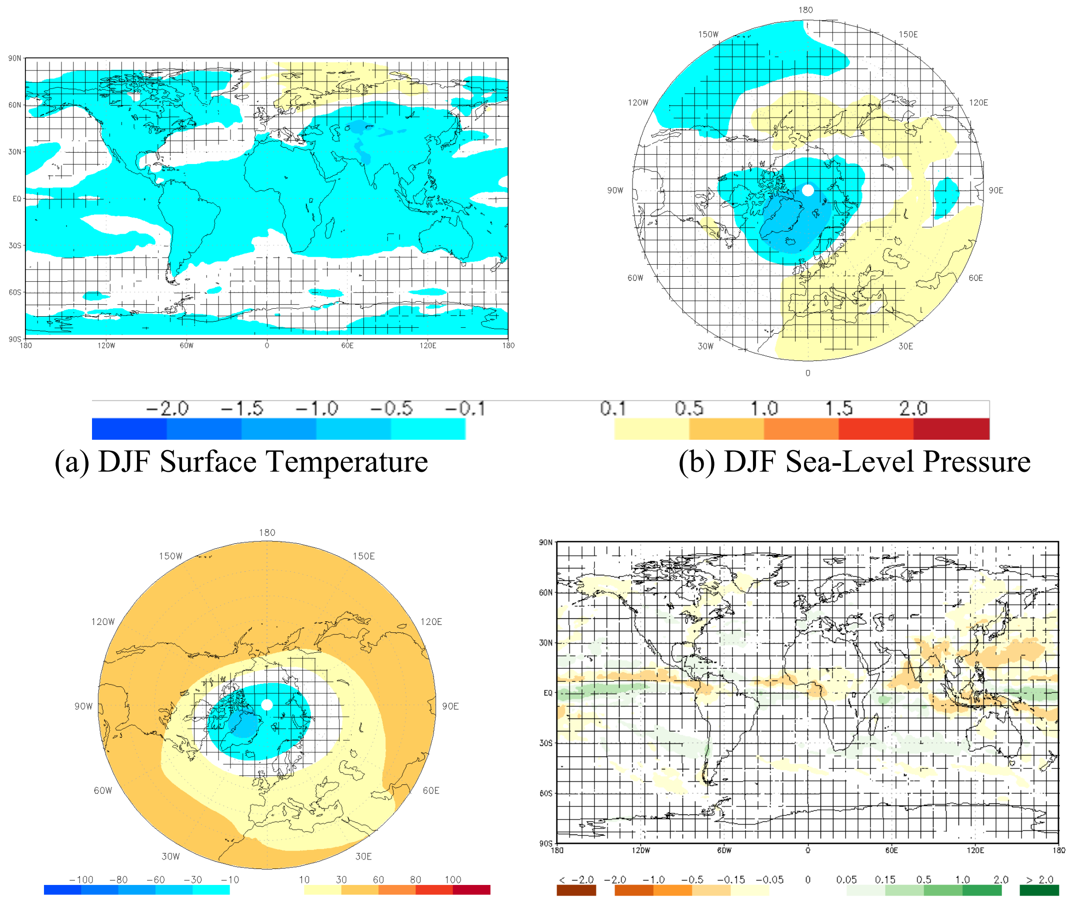

(a) DJF Surface Temperature (b) DJF Sea-Level Pressure

(c) DJF 50 hPa Geopotential Height (d) JJA Precipitation

Figure 2.10 CMIP5 multi-model means of the simulations of the response to the nine eruptions analyzed in *Driscoll et al.* [2012] for each of the 20 models listed in Table 1. Hatching displays areas where fewer than 15 of 20 models agree on the sign of the anomaly.

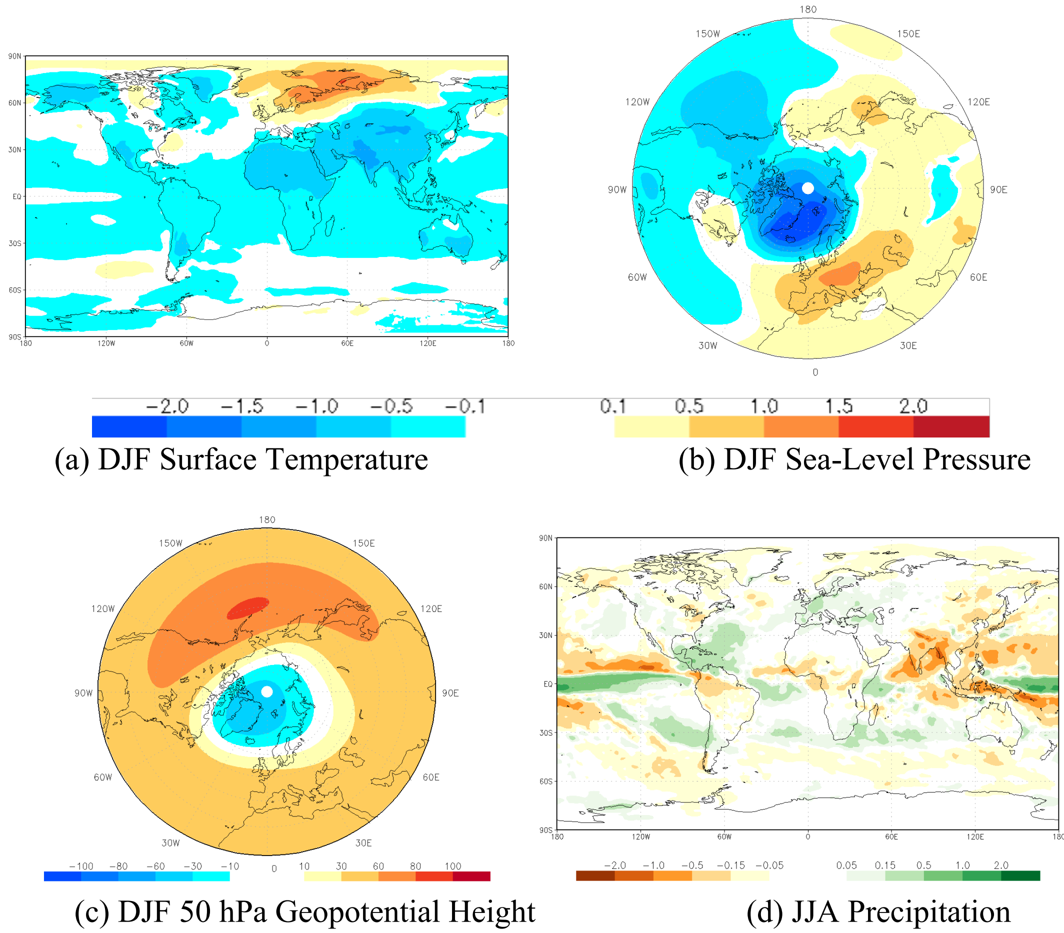

Figure 2.11 CMIP5 multi-model means of the simulations of the response to (a), (b), and (d) the Krakatau and Pinatubo eruptions and to (c) the El Chichón and Pinatubo eruptions for 16 of the 20 models listed in Table 1.

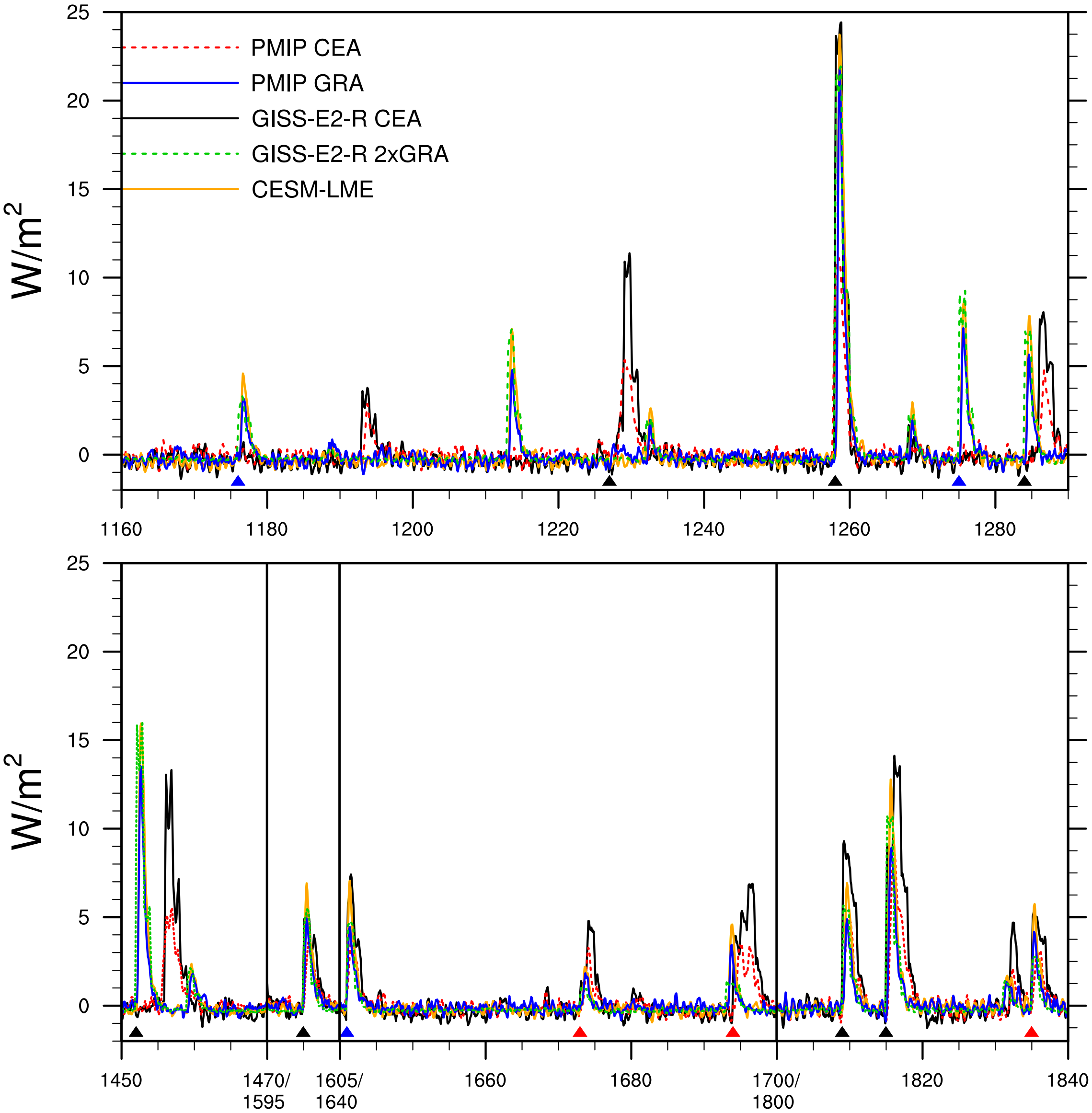

Figure 3.1 Three-month running means of the anomalies in global-averaged reflected solar flux (W m^{-2}) for selected periods. Results plotted for the six ensembles (Table 1) and represent averages over all the individual realizations for each ensemble. GISS-E2-R 2xGRA anomalies are scaled by a factor of 0.25. Blue, red, and black triangles indicate volcanic eruptions analyzed for the GRA forcing only, the CEA forcing only, and for both forcings, respectively.

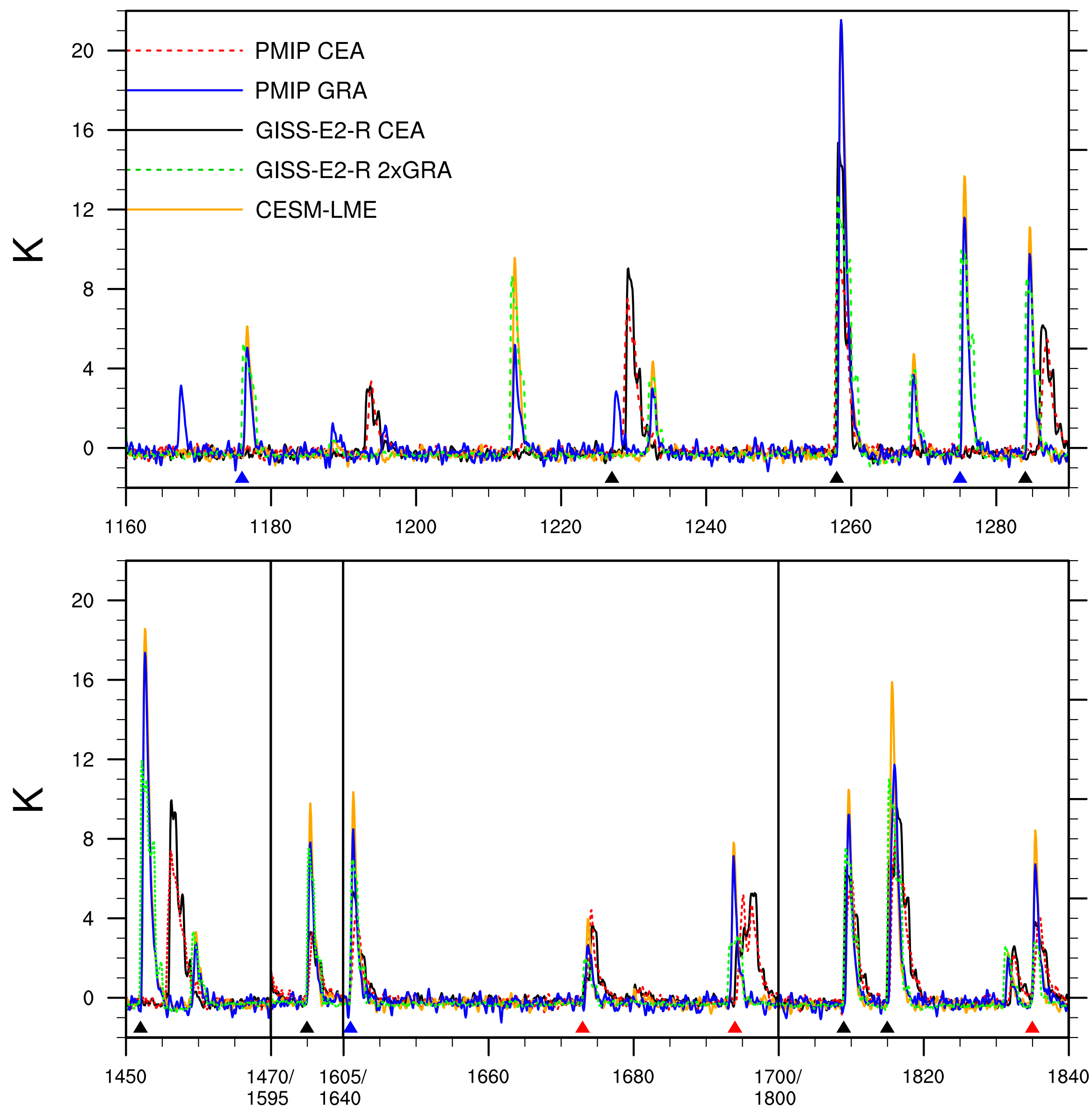

Figure 3.2 Three-month running means of the 50 hPa temperature anomalies (K) averaged between 30°S and 30°N. Results plotted for the six ensembles (Table 1) and represent averages over all the individual realizations for each ensemble. GISS-E2-R 2xGRA anomalies are scaled by a factor of 0.5. Blue, red, and black triangles indicate volcanic eruptions analyzed for the GRA forcing only, the CEA forcing only, and for both forcings, respectively.

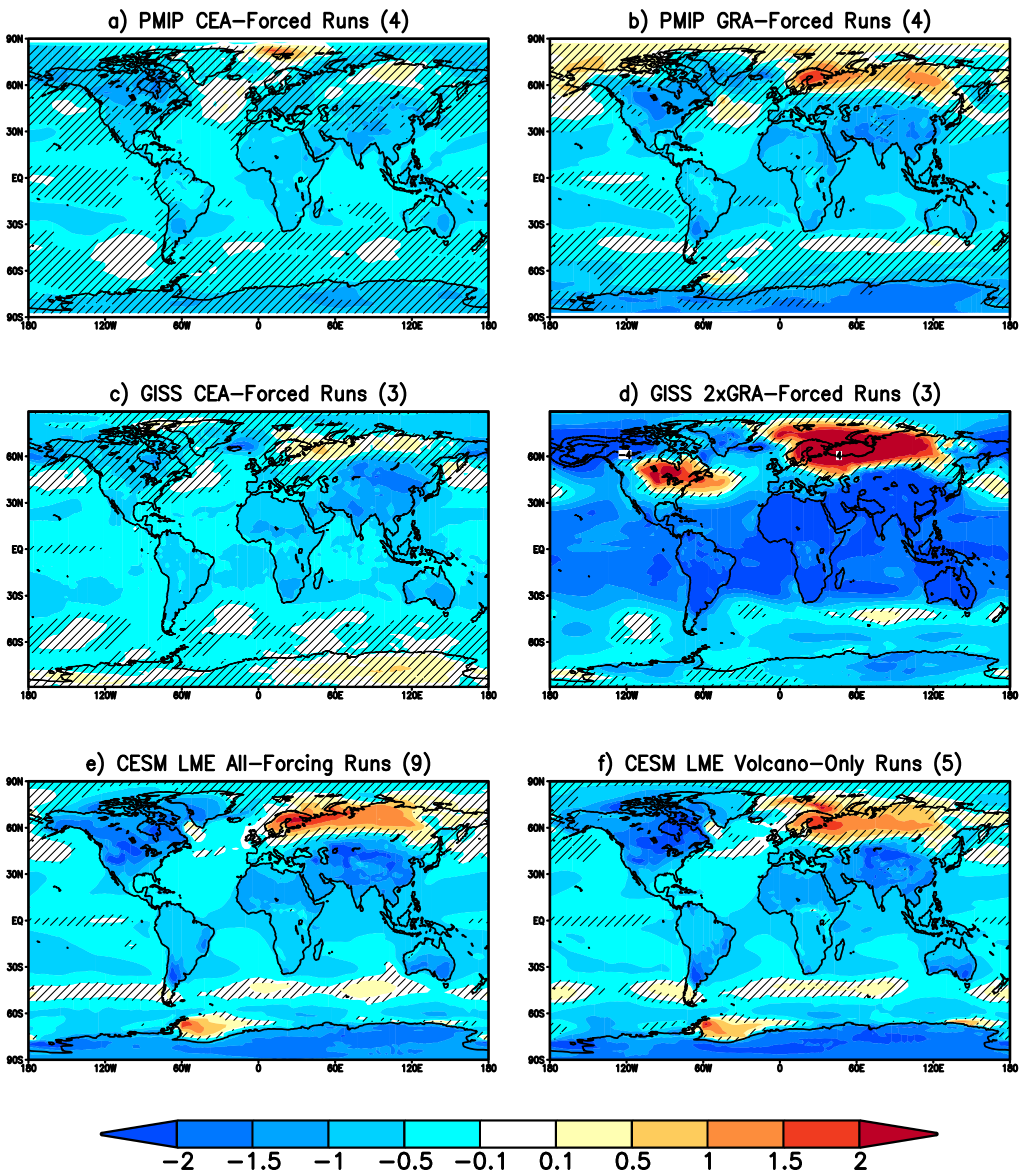

Figure 3.3 Surface temperature anomalies with respect to the five years preceding each eruption (K) for the first winter (DJF) after the ten largest tropical eruptions spanning 850-1850 (Table 4) for (a) CEA-forced PMIP runs, (b) GRA-forced PMIP runs, (c) CEA-forced GISS-E2-R runs, (d) 2xGRA-forced GISS-E2-R runs, (e) all-forcing CESM-LME runs, and (f) volcano-only CESM-LME runs. Hatching displays areas below 95% significance using a two-tailed t-test.

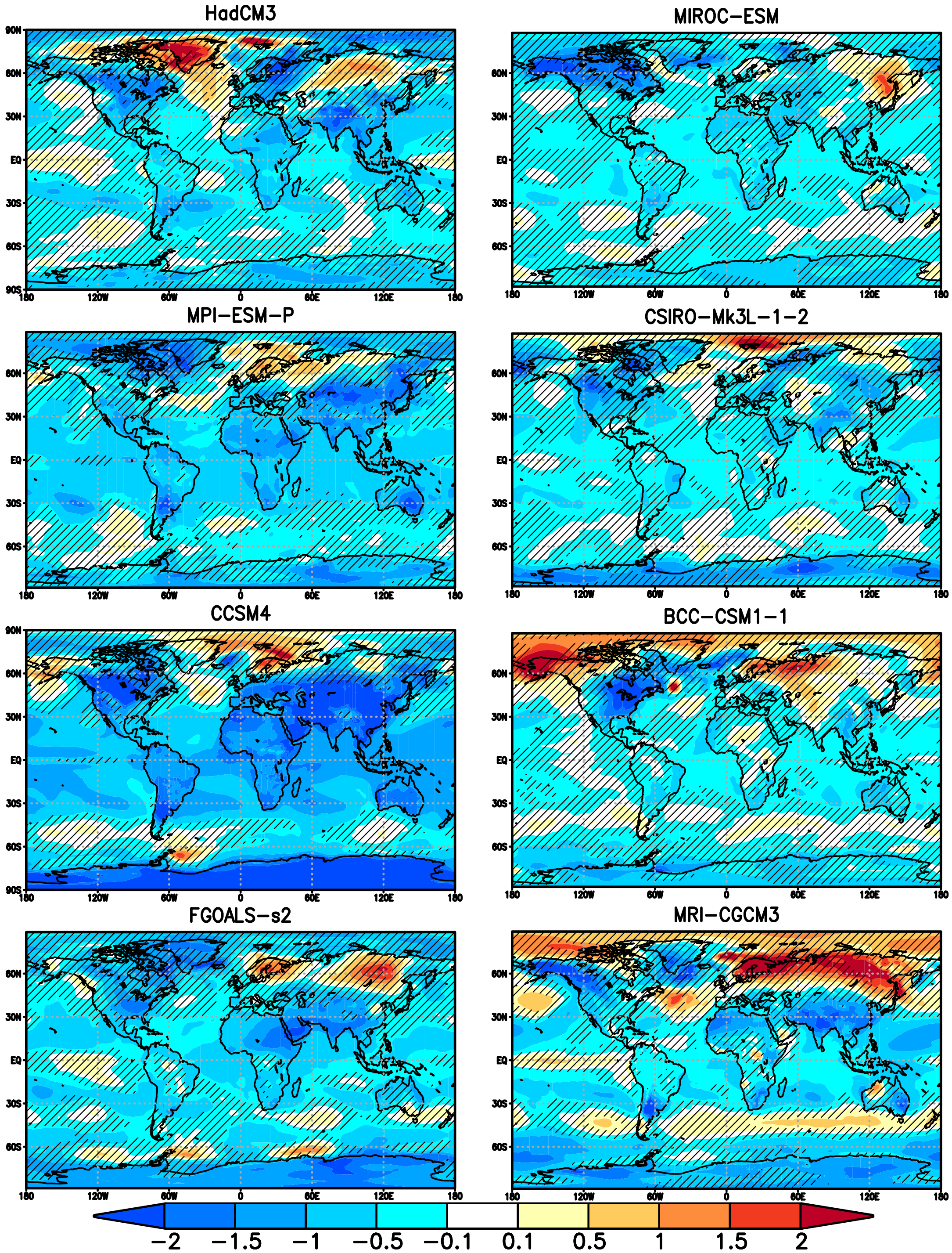

Figure 3.4 Surface temperature anomalies with respect to the five years preceding each eruption (K) for the first winter (DJF) after the ten largest tropical eruptions spanning 850-1850 (Table 4) for individual PMIP model means. Hatching displays areas below 95% significance using a two-tailed t-test. Panels 1-4 are CEA-forced models; 5-8 are GRA-forced models.

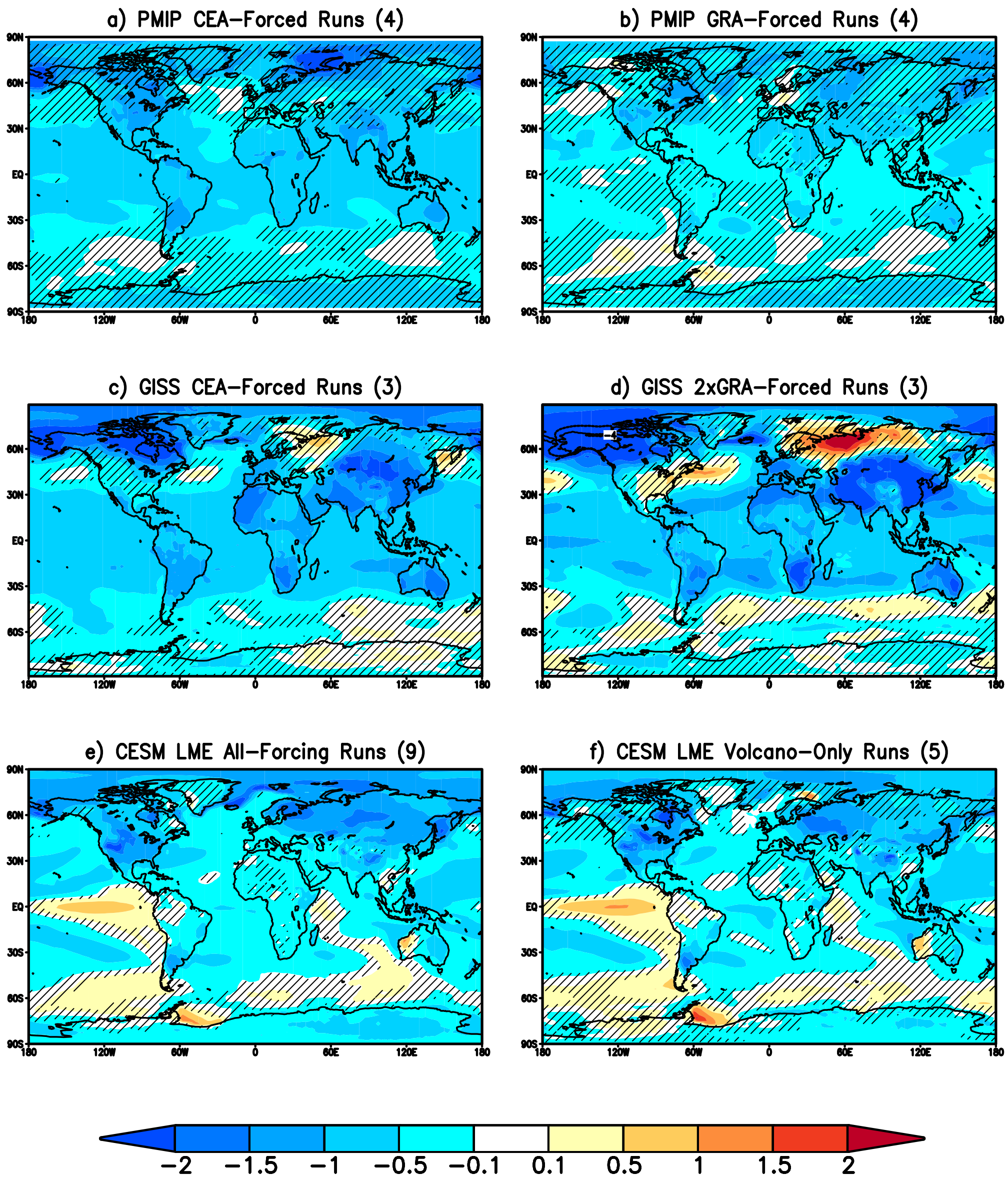

Figure 3.5 Surface temperature anomalies with respect to the five years preceding each eruption (K) for the second winter (DJF) after the ten largest tropical eruptions spanning 850-1850 (Table 4) for (a) CEA-forced PMIP runs, (b) GRA-forced PMIP runs, (c) CEA-forced GISS-E2-R runs, (d) 2xGRA-forced GISS-E2-R runs, (e) all-forcing CESM-LME runs, and (f) volcano-only CESM-LME runs. Hatching displays areas below 95% significance using a two-tailed t-test.

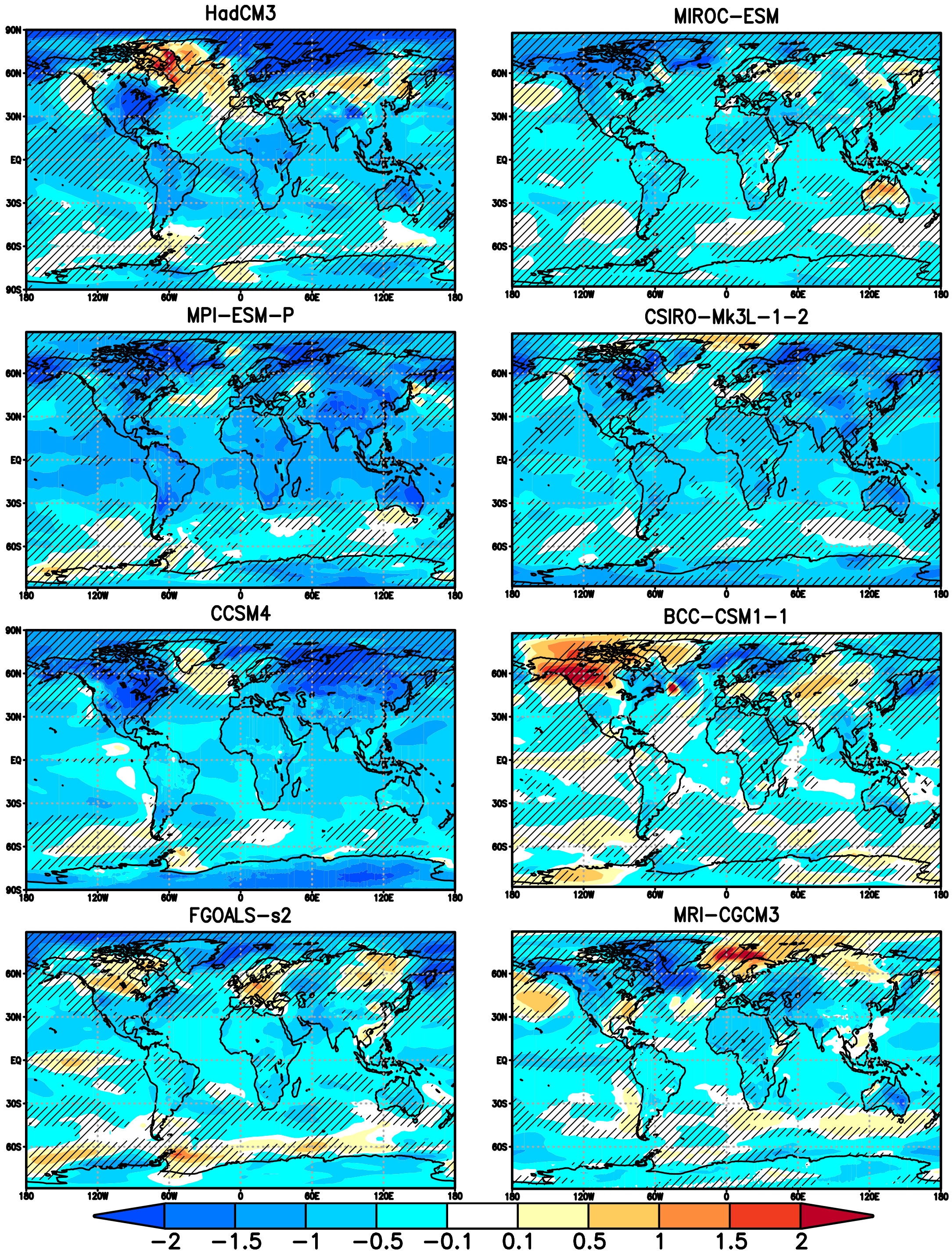

Figure 3.6 Surface temperature anomalies with respect to the five years preceding each eruption (K) for the second winter (DJF) after the ten largest tropical eruptions spanning 850-1850 (Table 4) for individual PMIP model means. Hatching displays areas below 95% significance using a two-tailed t-test. Panels 1-4 are CEA-forced models; 5-8 are GRA-forced models.

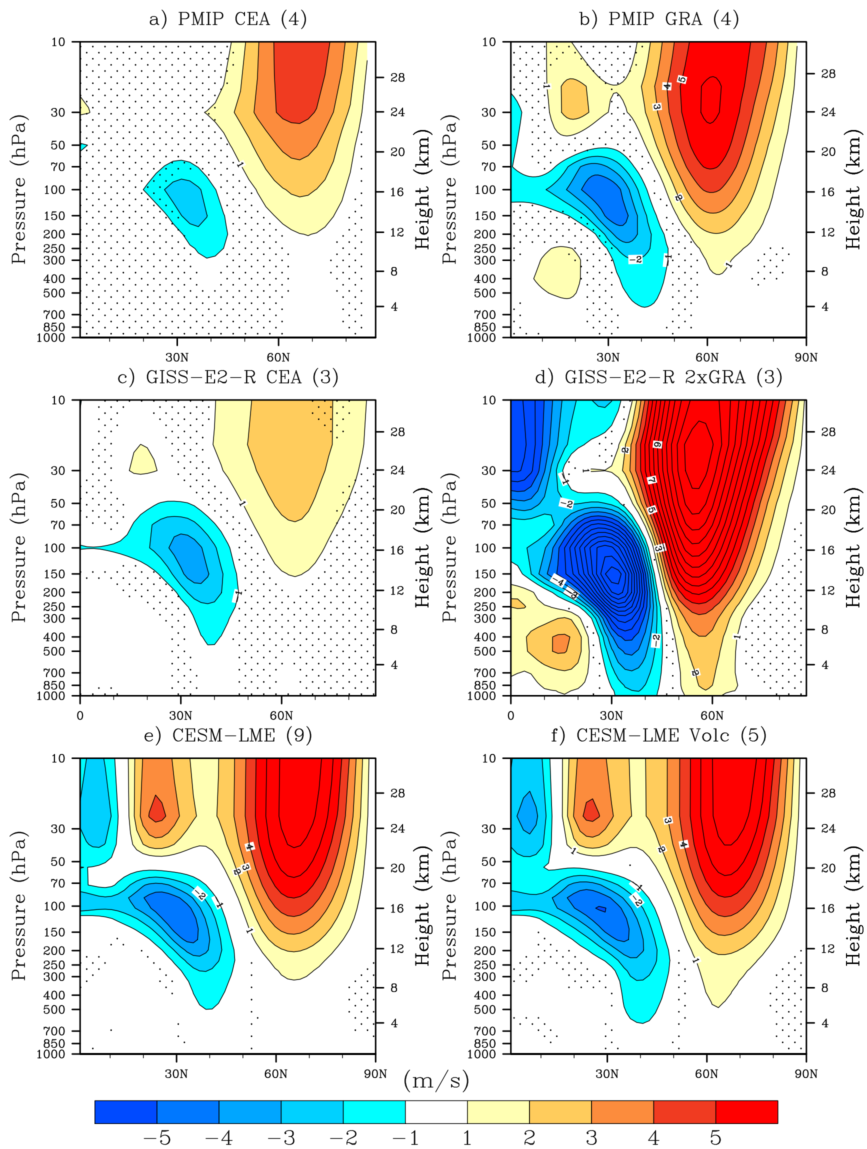

Figure 3.7 NH zonal mean zonal wind anomalies with respect to the five years preceding each eruption (m/s) for the first winter (DJF) after the ten largest tropical eruptions spanning 850-1850 (Table 4) for (a) CEA-forced PMIP runs, (b) GRA-forced PMIP runs, (c) CEA-forced GISS-E2-R runs, (d) 2xGRA-forced GISS-E2-R runs, (e) all-forcing CESM-LME runs, and (f) volcano-only CESM-LME runs. Contours represent 1 m/s intervals; stippling displays areas below 95% significance using a two-tailed t-test.

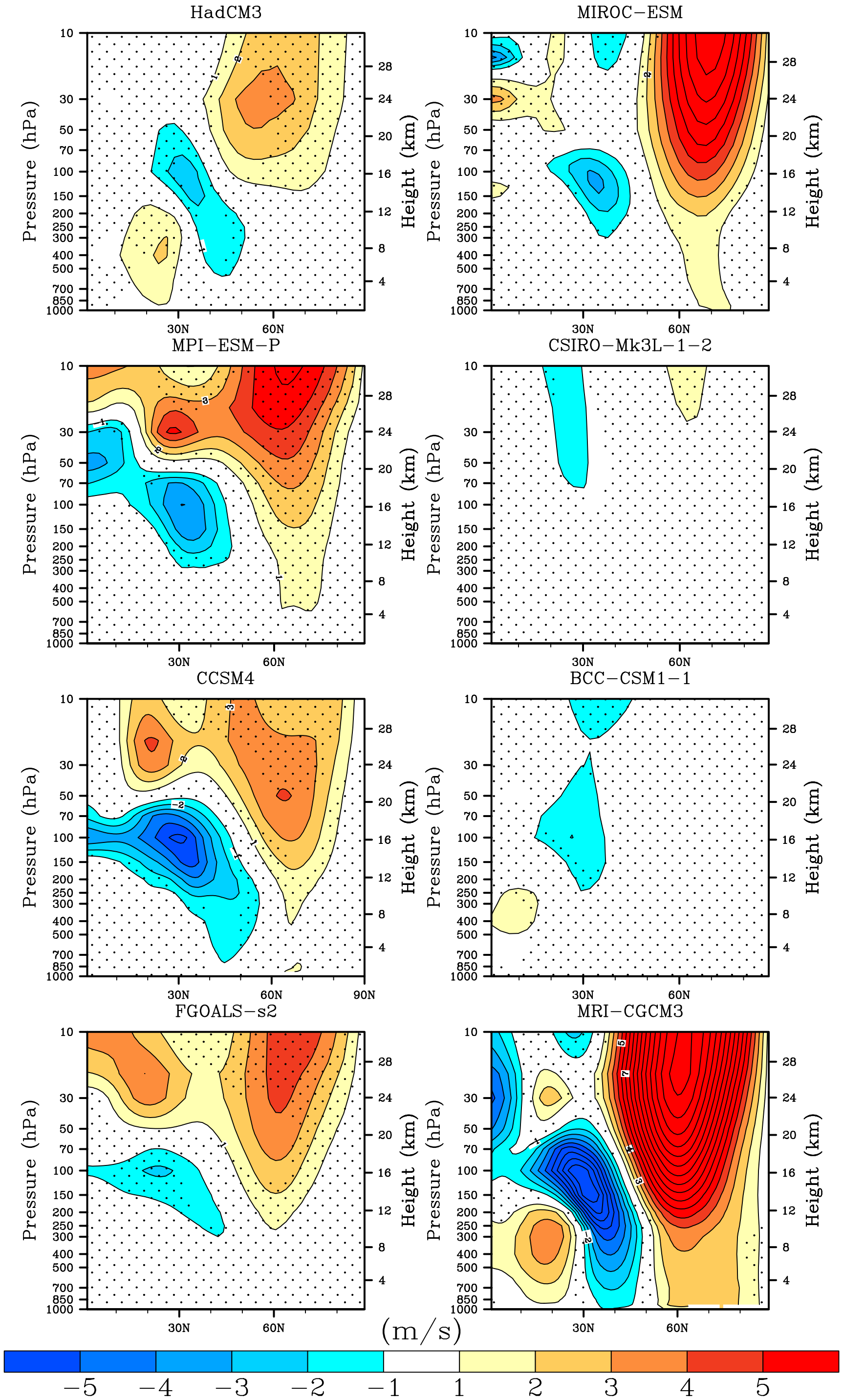

Figure 3.8 NH zonal mean zonal wind anomalies with respect to the five years preceding each eruption (m/s) for the first winter (DJF) after the ten largest tropical eruptions spanning 850-1850 (Table 4) for the individual PMIP model means (Table 2). Contours represent 1 m/s intervals; stippling displays areas below 95% significance using a two-tailed t-test. Panels 1-4 are CEA-forced models; 5-8 are GRA-forced models.

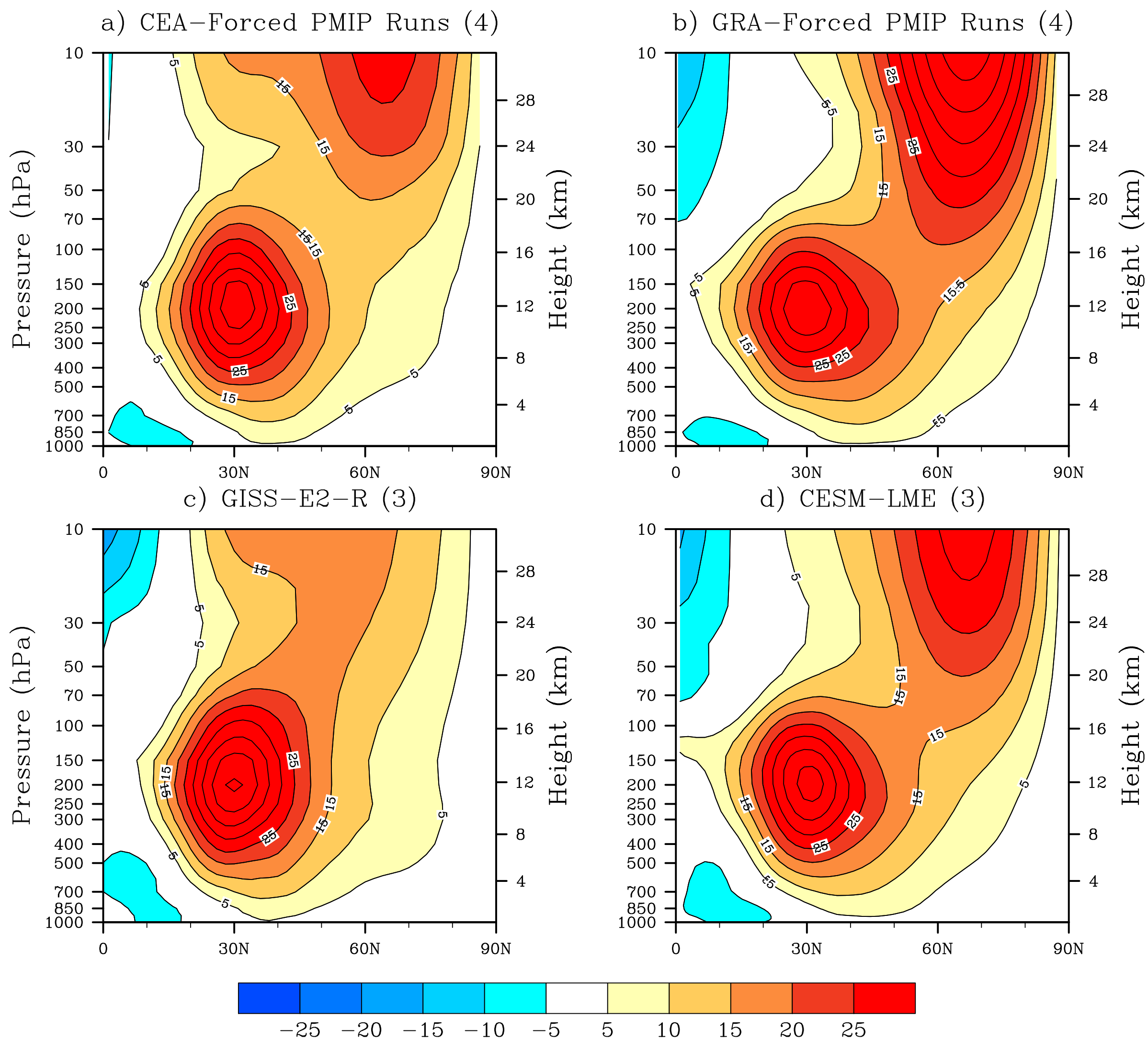

Figure 3.9 NH DJF zonal mean zonal wind climatology for the period 850-1850 for (a) CEA-forced PMIP ensemble, (b) GRA-forced PMIP ensemble, (c) GISS-E2-R, and (d) CESM-LME. Contours represent 5 m/s intervals.

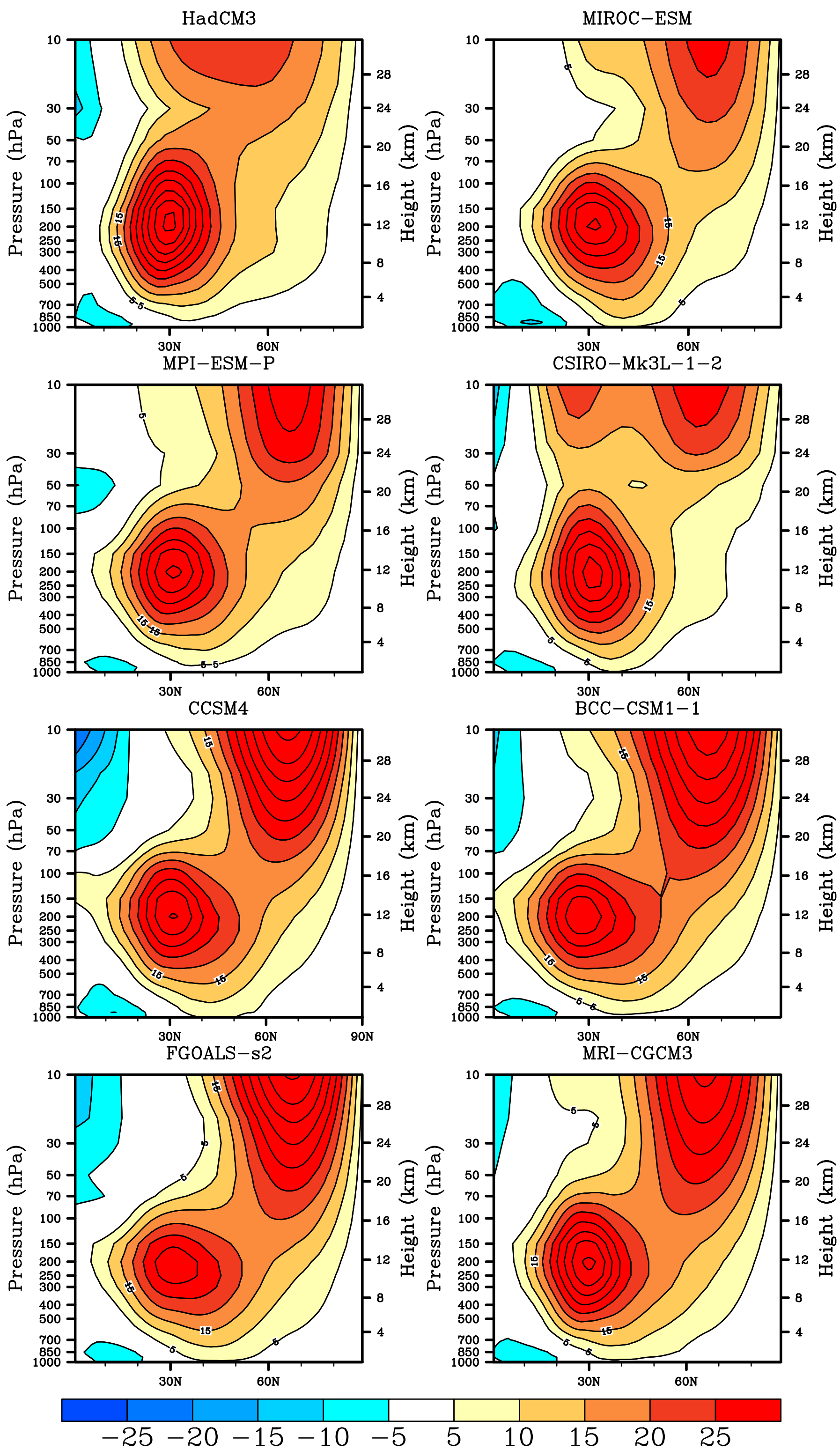

Figure 3.10 NH DJF zonal mean zonal wind climatology for individual PMIP model means for the period 850-1850. Contours represent 5 m/s intervals. Panels 1-4 are CEA-forced models; 5-8 are GRA-forced models.

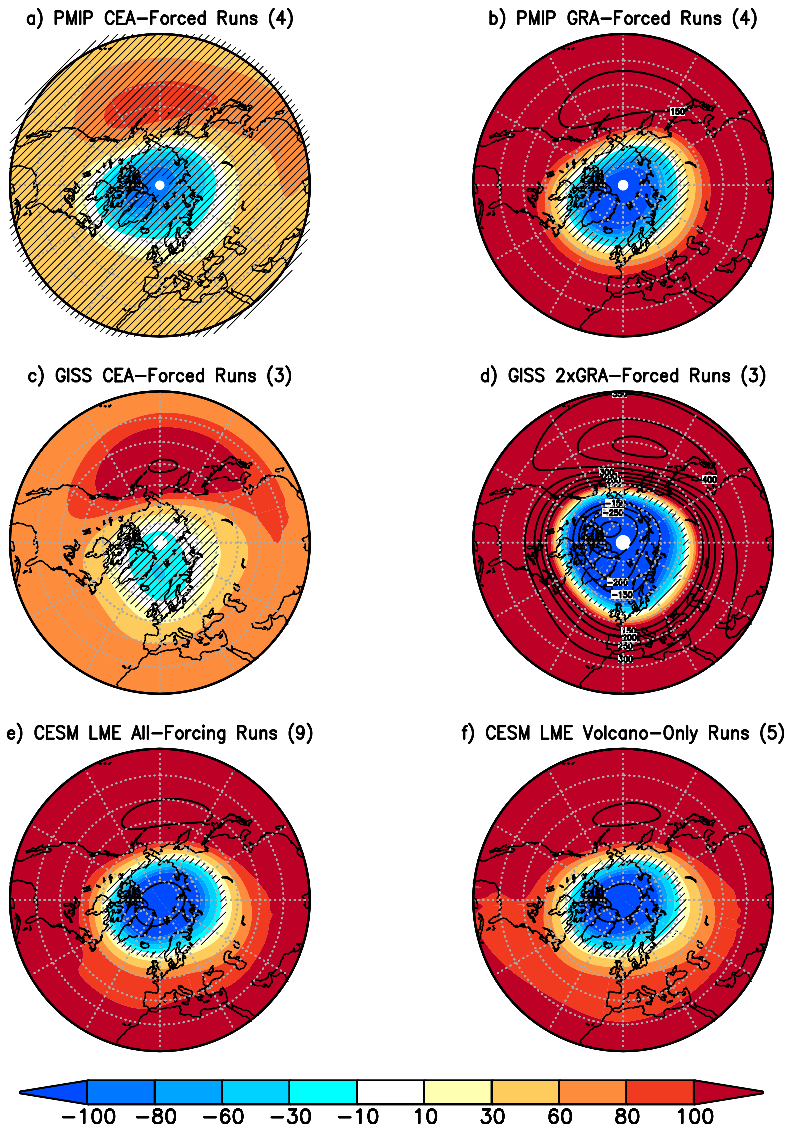

Figure 3.11 50 hPa geopotential height anomalies with respect to the five years preceding each eruption (m) for the first winter (DJF) after the ten largest tropical eruptions spanning 850-1850 (Table 4) for (a) CEA-forced PMIP runs, (b) GRA-forced PMIP runs, (c) CEA-forced GISS-E2-R runs, (d) 2xGRA-forced GISS-E2-R runs, (e) all-forcing CESM-LME runs, and (f) volcano-only CESM-LME runs. Hatching displays areas below 95% significance using a two-tailed t-test.

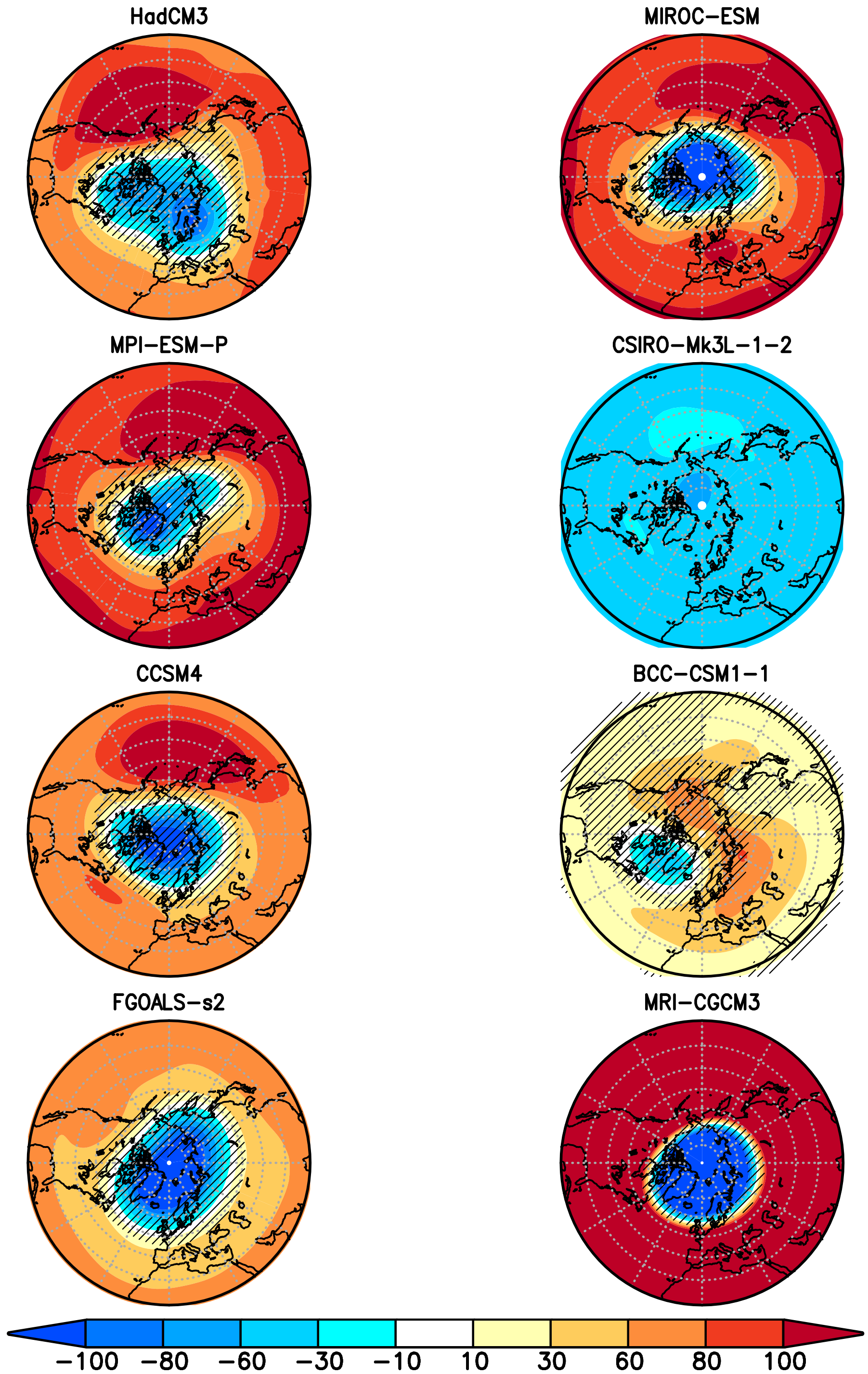

Figure 3.12 50-hPa geopotential height anomalies with respect to the five years preceding each eruption (m) for the first winter (DJF) after the ten largest tropical eruptions spanning 850-1850 (Table 4) for individual PMIP model means. Hatching displays areas below 95% significance using a two-tailed t-test. Panels 1-4 are CEA-forced models; 5-8 are GRA-forced models.

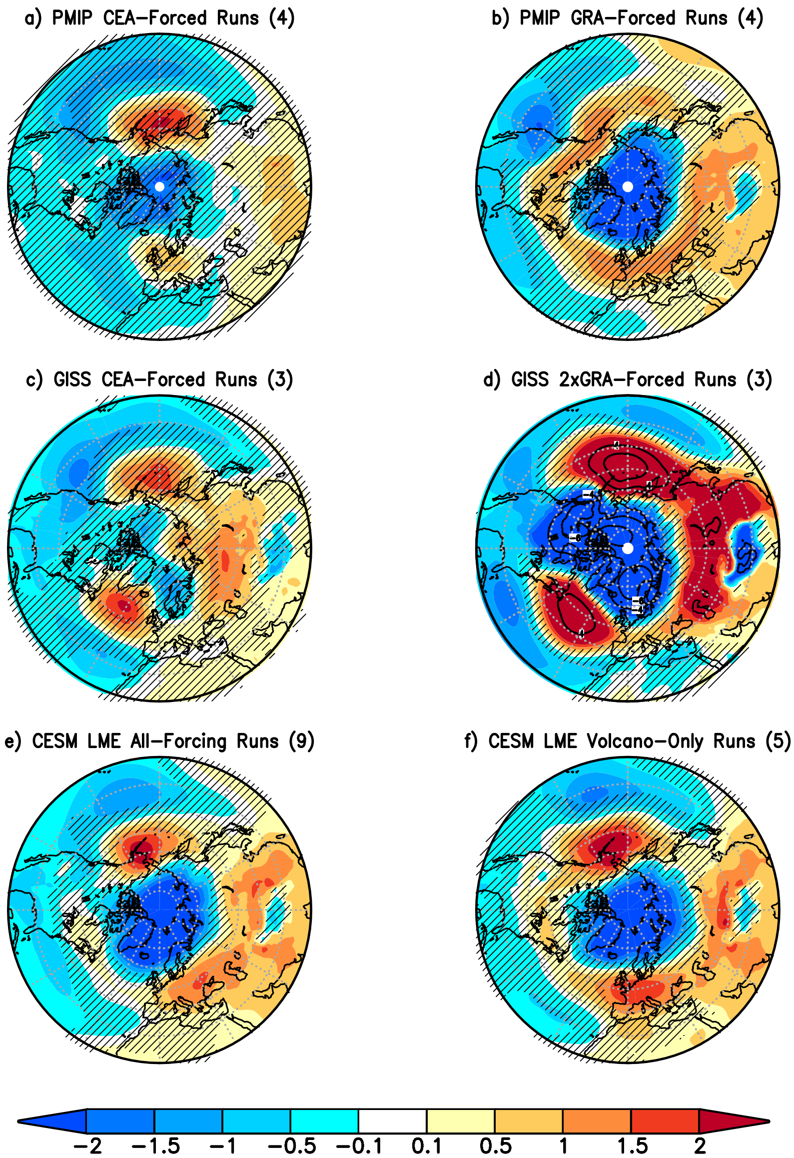

Figure 3.13 Sea level pressure anomalies with respect to the five years preceding each eruption (hPa) for the first winter (DJF) after the ten largest tropical eruptions spanning 850-1850 (Table 4) for (a) CEA-forced PMIP runs, (b) GRA-forced PMIP runs, (c) CEA-forced GISS-E2-R runs, (d) 2xGRA-forced GISS-E2-R runs, (e) all-forcing CESM-LME runs, and (f) volcano-only CESM-LME runs. Hatching displays areas below 95% significance using a two-tailed t-test.

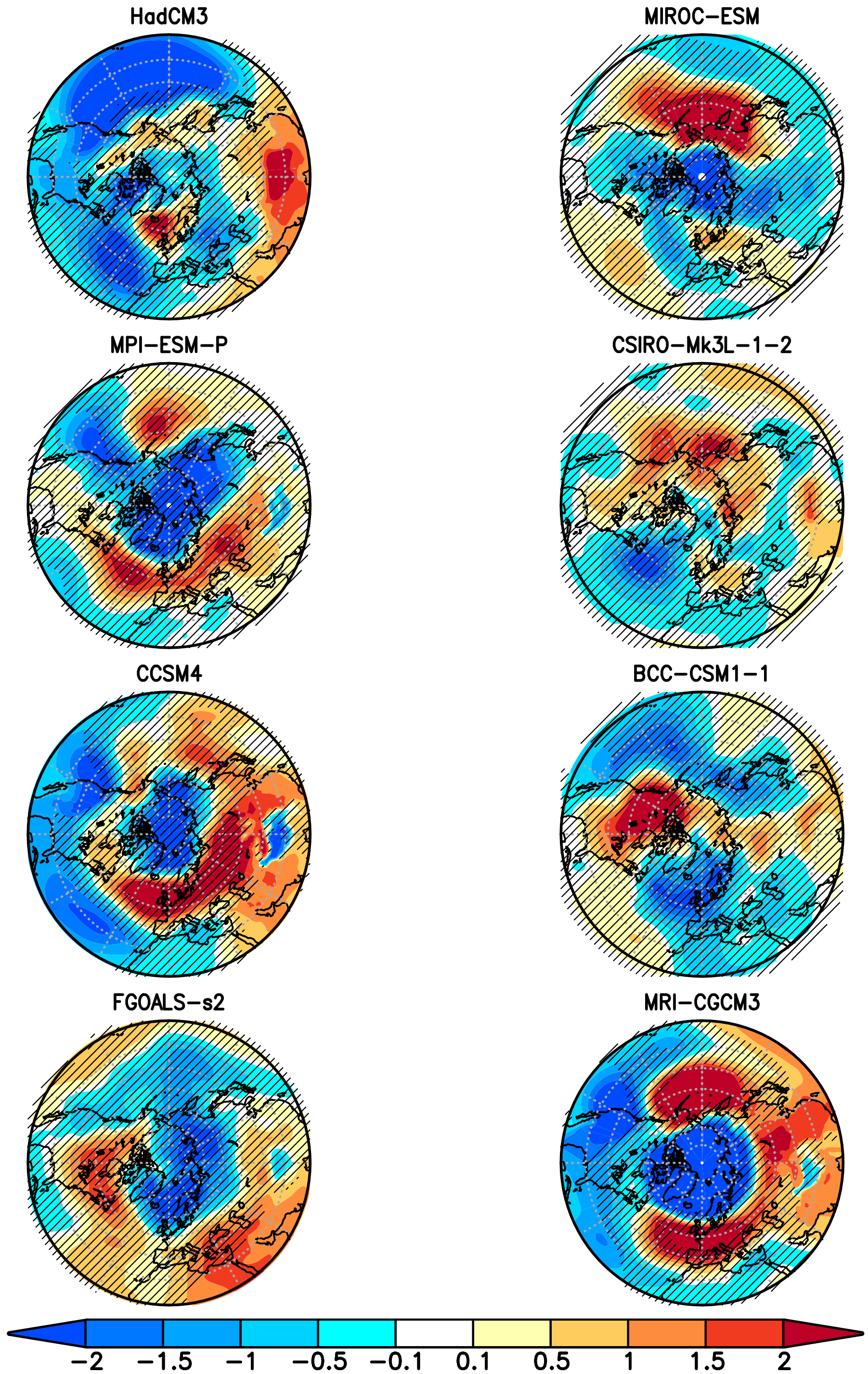

Figure 3.14 Sea level pressure anomalies with respect to the five years preceding each eruption (hPa) for the first winter (DJF) after the ten largest tropical eruptions spanning 850-1850 (Table 4) for individual PMIP model means. Hatching displays areas below 95% significance using a two-tailed t-test. Panels 1-4 are CEA-forced models; 5-8 are GRA-forced models.

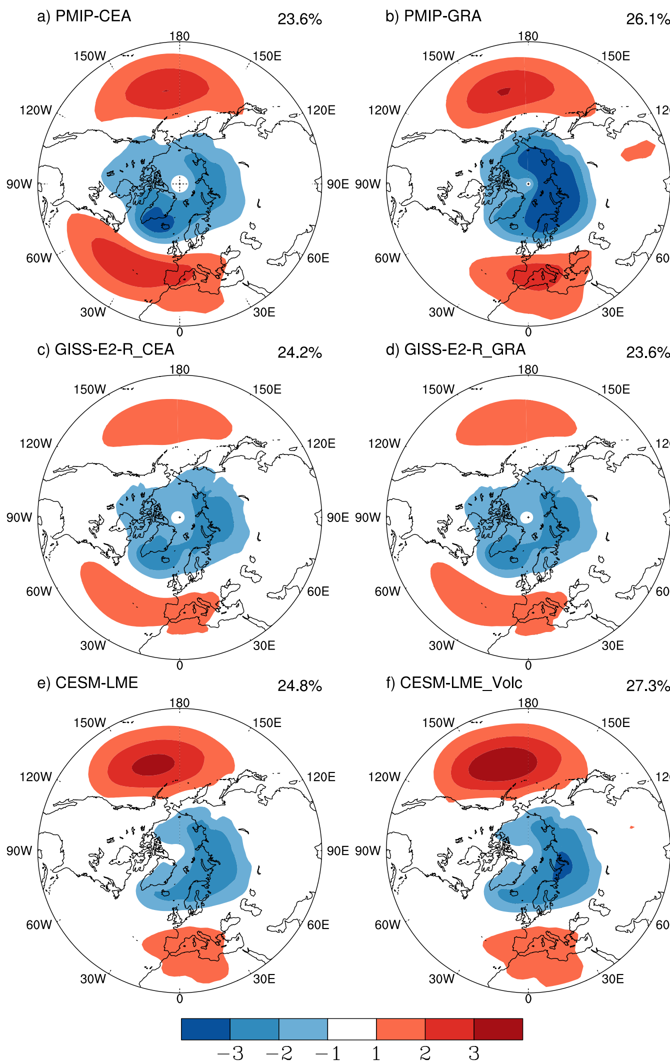

Figure 3.15 Leading EOF of the monthly winter (DJF) mean sea level pressure anomaly over the north of 20°N for each ensemble mean over the period 850-1850. EOF values are expressed as hPa. In the top right corner of each plot is indicated the percentage of variance explained by the first EOF.

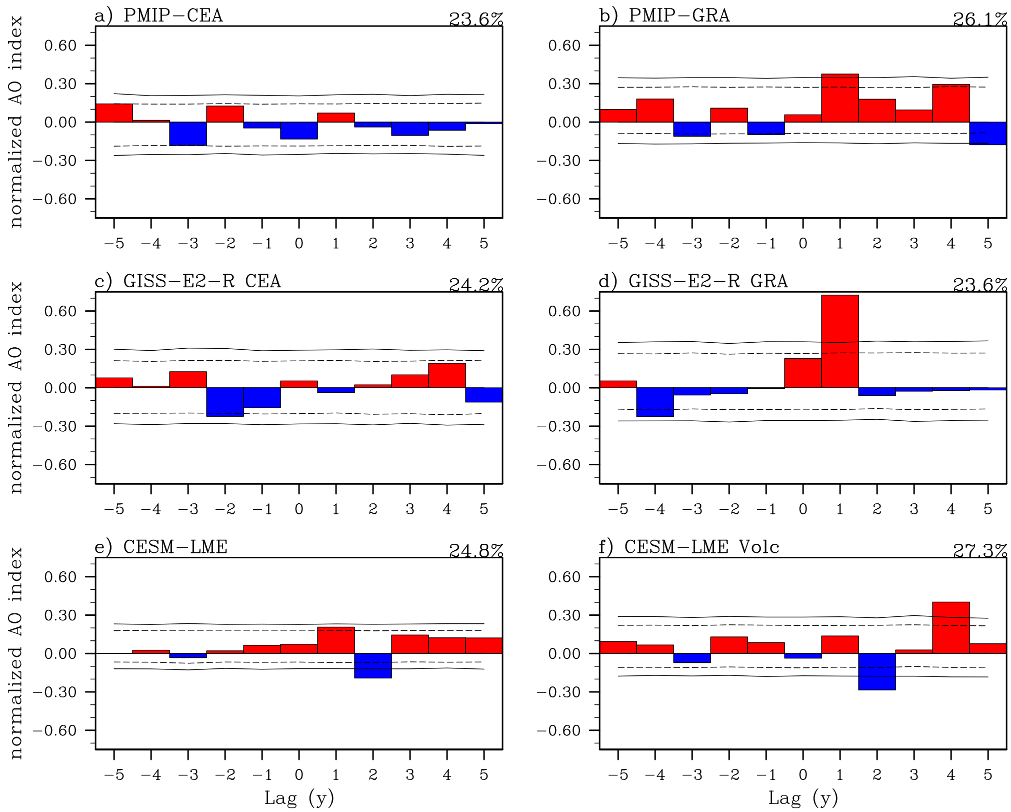

Figure 3.16 Superposed epoch analysis for the winter (DJF) AO index for the six ensembles for the 10 eruptions listed in Table 4. The average over 10 volcanic eruptions is shown at different lag time. Lag 1 indicates the first winter after a volcanic eruption. In the top right corner of each plot is indicated the percentage of variance explained by the first EOF. Dotted horizontal lines show the 5th and 95th percentiles of the bootstrap distribution; solid horizontal lines show the 1st and 99th percentiles.

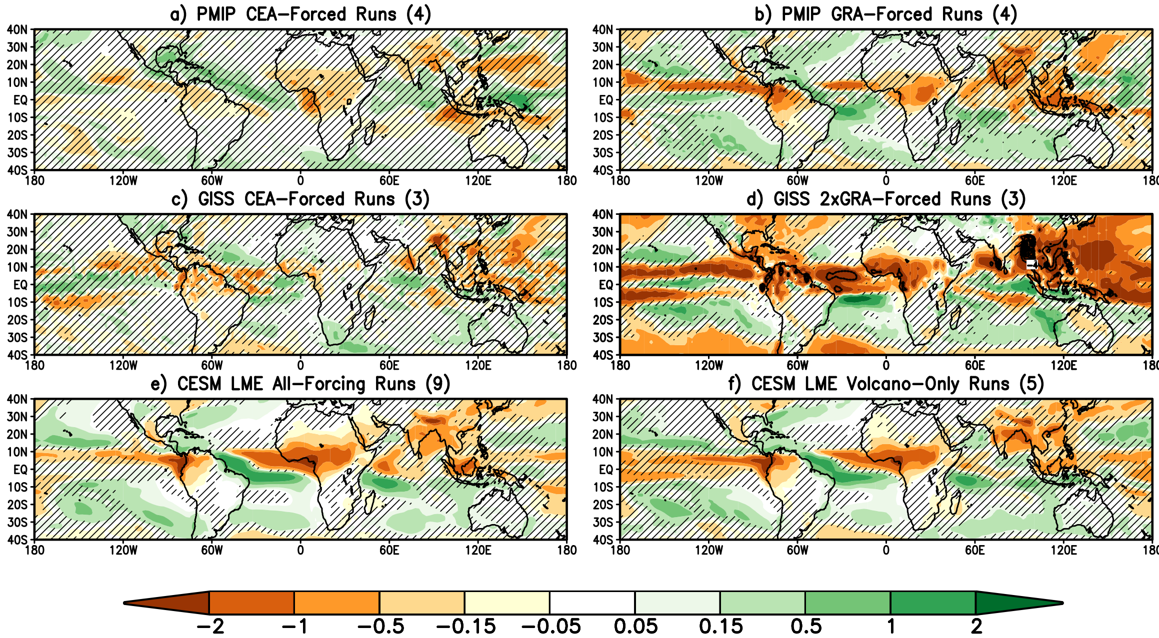

Figure 3.17 Precipitation anomalies with respect to the five years preceding each eruption (mm/d) for the first summer (JJA) after the ten largest tropical eruptions spanning 850-1850 (Table 4) for (a) CEA-forced PMIP runs, (b) GRA-forced PMIP runs, (c) CEA-forced GISS-E2-R runs, (d) 2xGRA-forced GISS-E2-R runs, (e) all-forcing CESM-LME runs, and (f) volcano-only CESM-LME runs. Hatching displays areas below 95% significance using a two-tailed t-test.

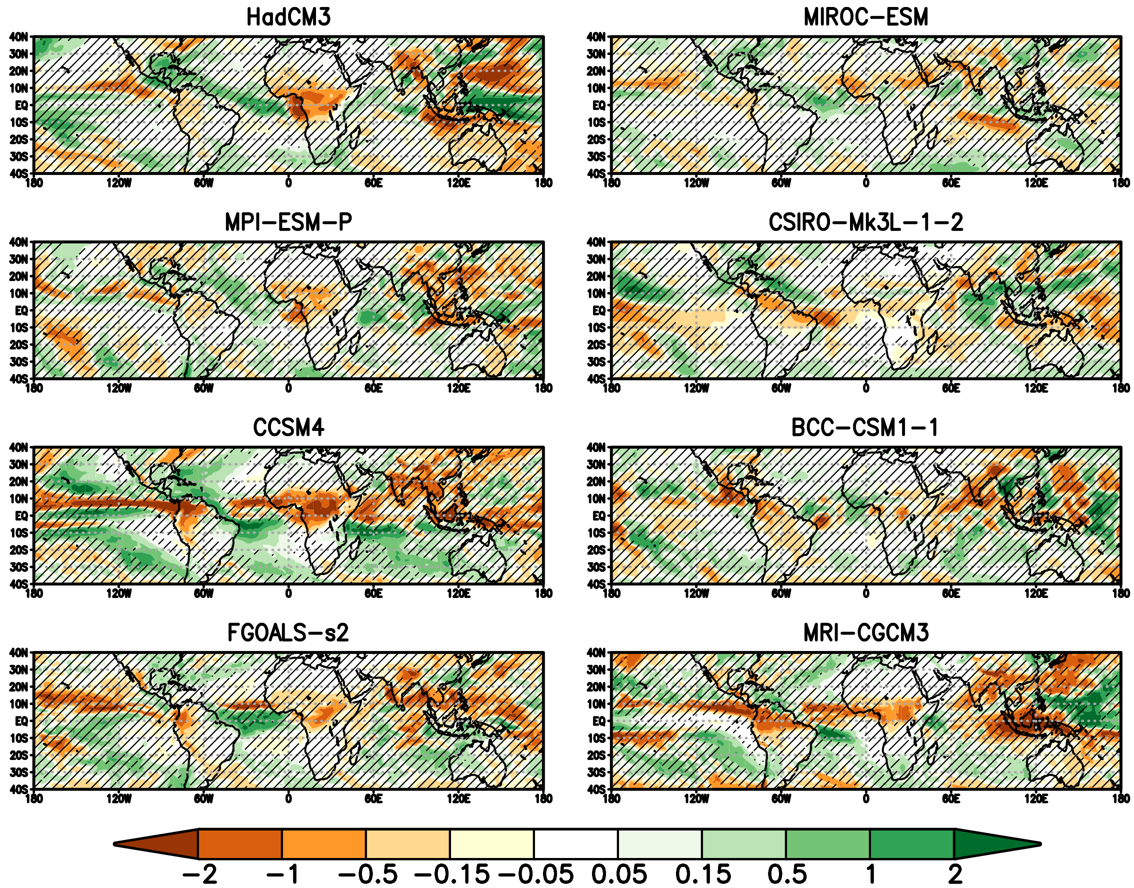

Figure 3.18 Precipitation anomalies with respect to the five years preceding each eruption (mm/d) for the first summer (JJA) after the ten largest tropical eruptions spanning 850-1850 (Table 4) for individual PMIP model means. Hatching displays areas below 95% significance using a two-tailed t-test. Panels 1-4 are CEA-forced models; 5-8 are GRA-forced models.

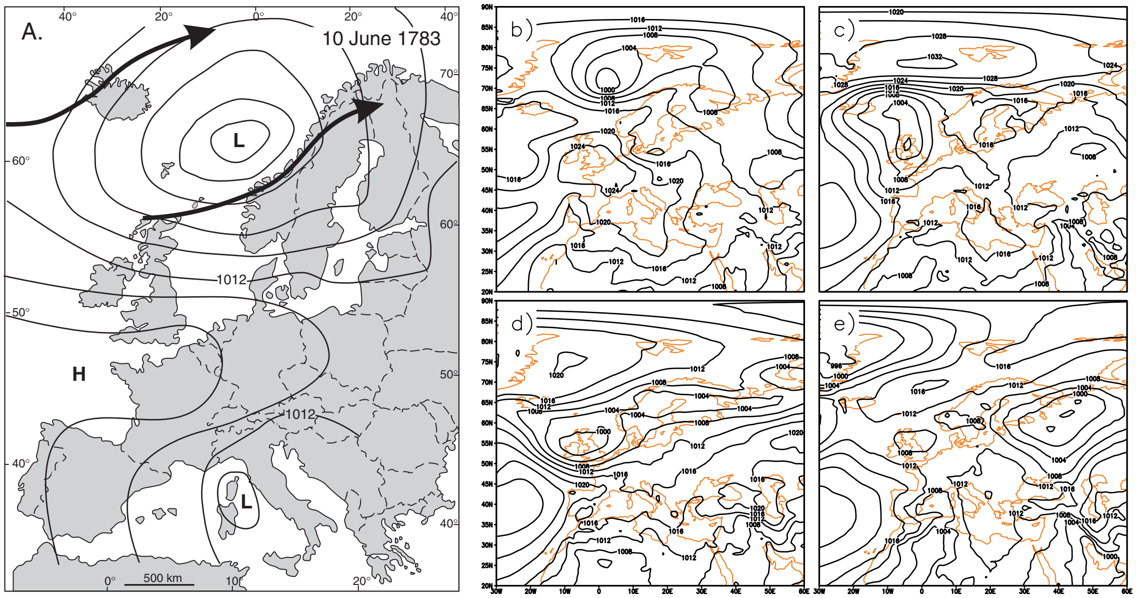

Figure 4.1 Sea level pressure maps for: (a) 8–12 June 1783 drawn from *Kington* [1988] (Figure 6a, *Thordarson and Self* [2003]) and (b)-(e) 8 June 1783 from initial conditions for the CESM1(WACCM) simulations, showing the circulation patterns over Europe.

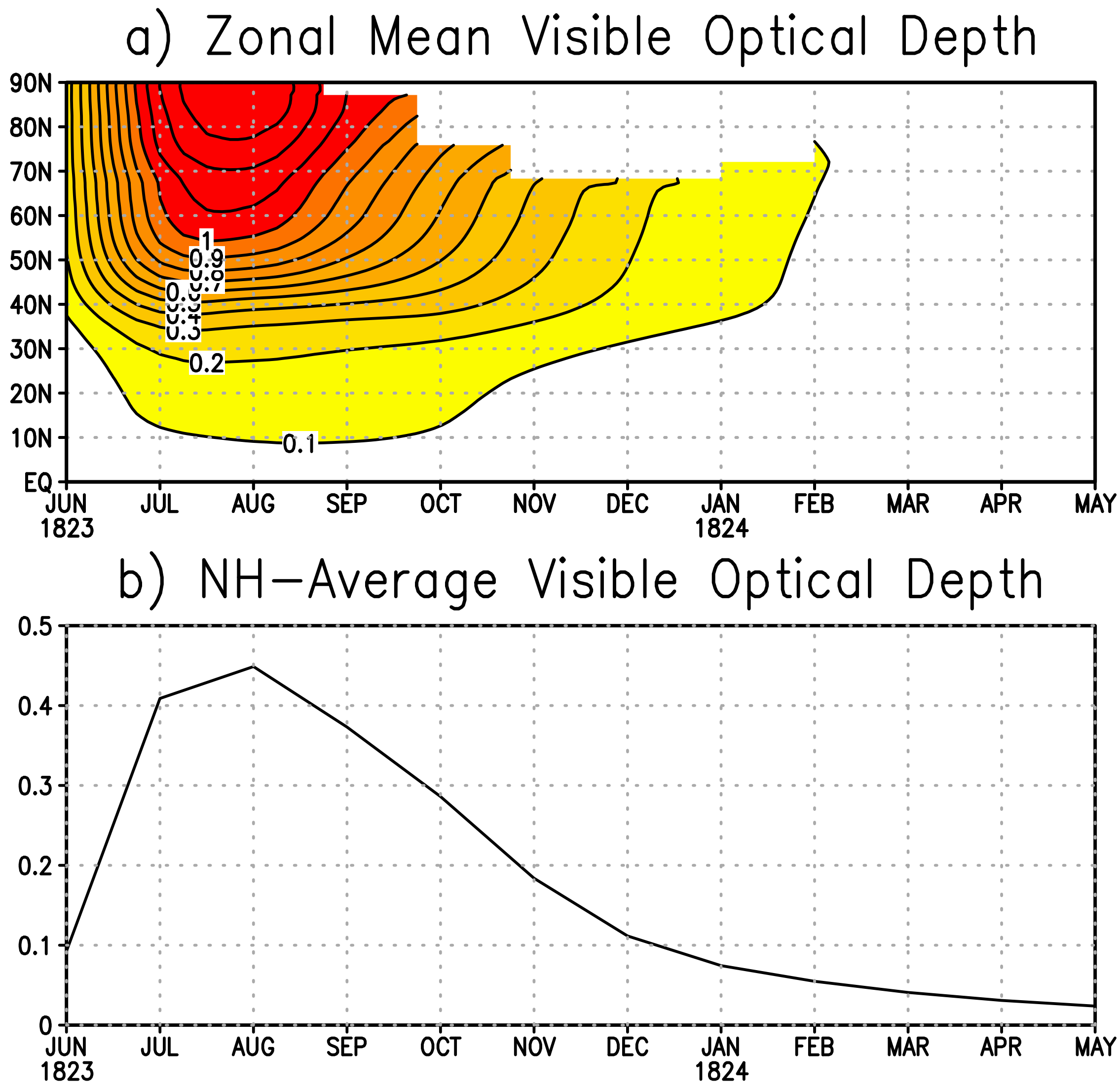

Figure 4.2 (a) Zonal mean and (b) NH-mean sulfate aerosol optical depth for the Laki ensemble from June 1783 to May 1784.

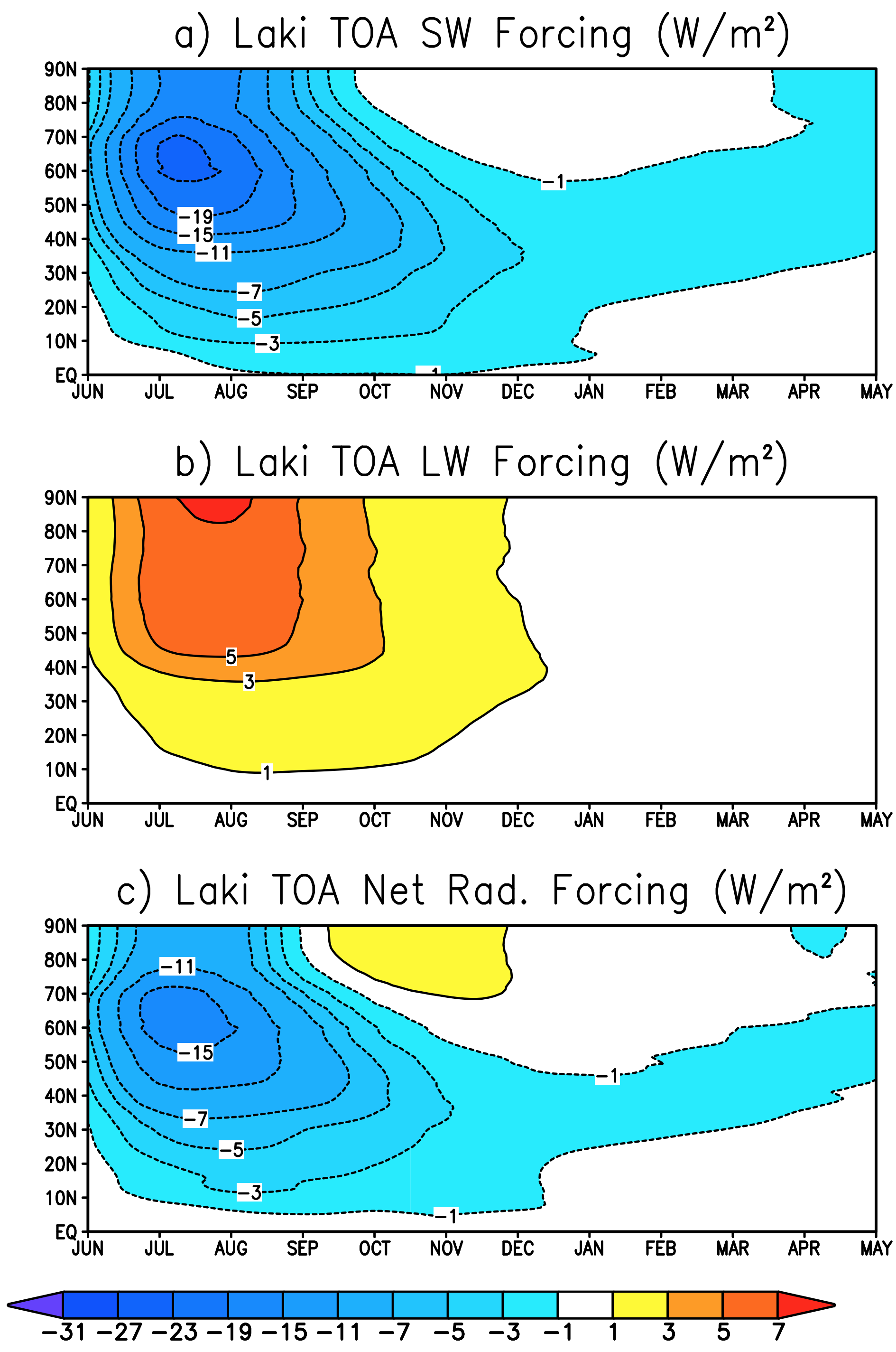

Figure 4.3 Zonal-average Northern Hemisphere top-of-atmosphere radiative forcing (W/m^2) for the Laki ensemble for (a) shortwave, (b) longwave, and (c) net.

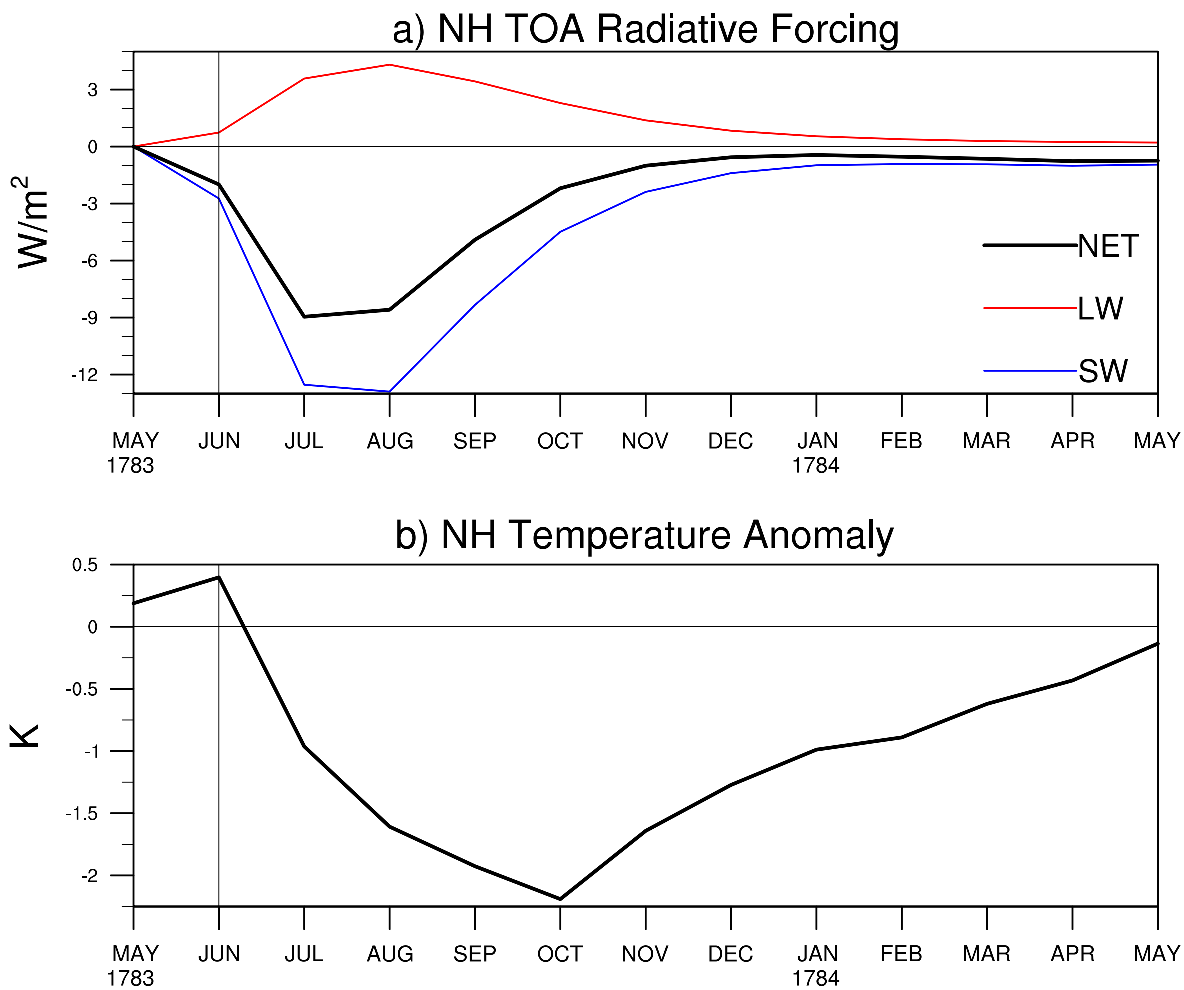

Figure 4.4 Ensemble mean change in (a) NH radiative forcing for shortwave (red), longwave (blue) and net (black), and (b) NH surface temperature.

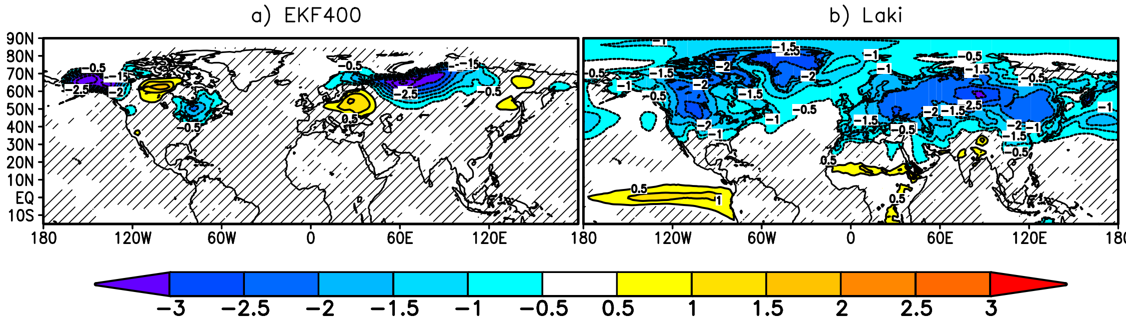

Figure 4.5 JJA 1783 surface temperature anomalies (K) for (a) EKF400 reanalysis and (b) average of Laki ensemble. Anomalies are calculated with respect to the five years before the eruption. Hatching represents areas < 95% significance using a two-tailed Student's t-test.

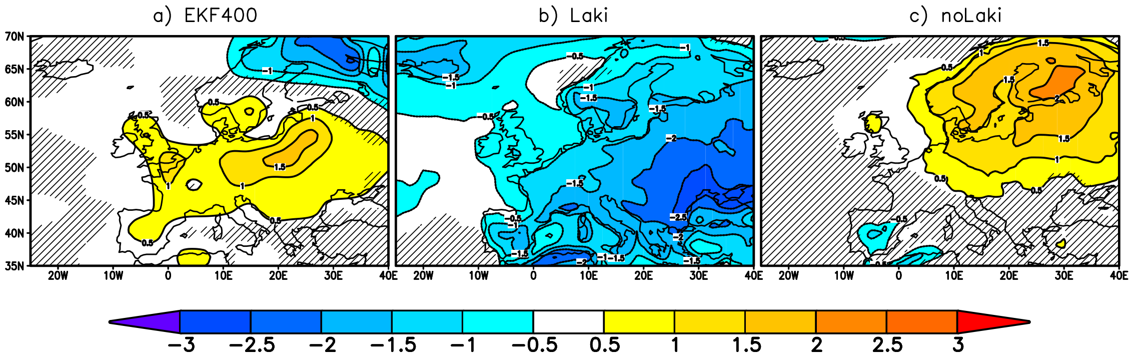

Figure 4.6 July 1783 European surface temperature anomalies (K) for (a) EKF400 reanalysis, (b) Laki ensemble average, and (c) noLaki ensemble average. Anomalies are calculated with respect to the five years before the eruption. Hatching represents areas < 95% significance using a two-tailed Student's *t*-test.

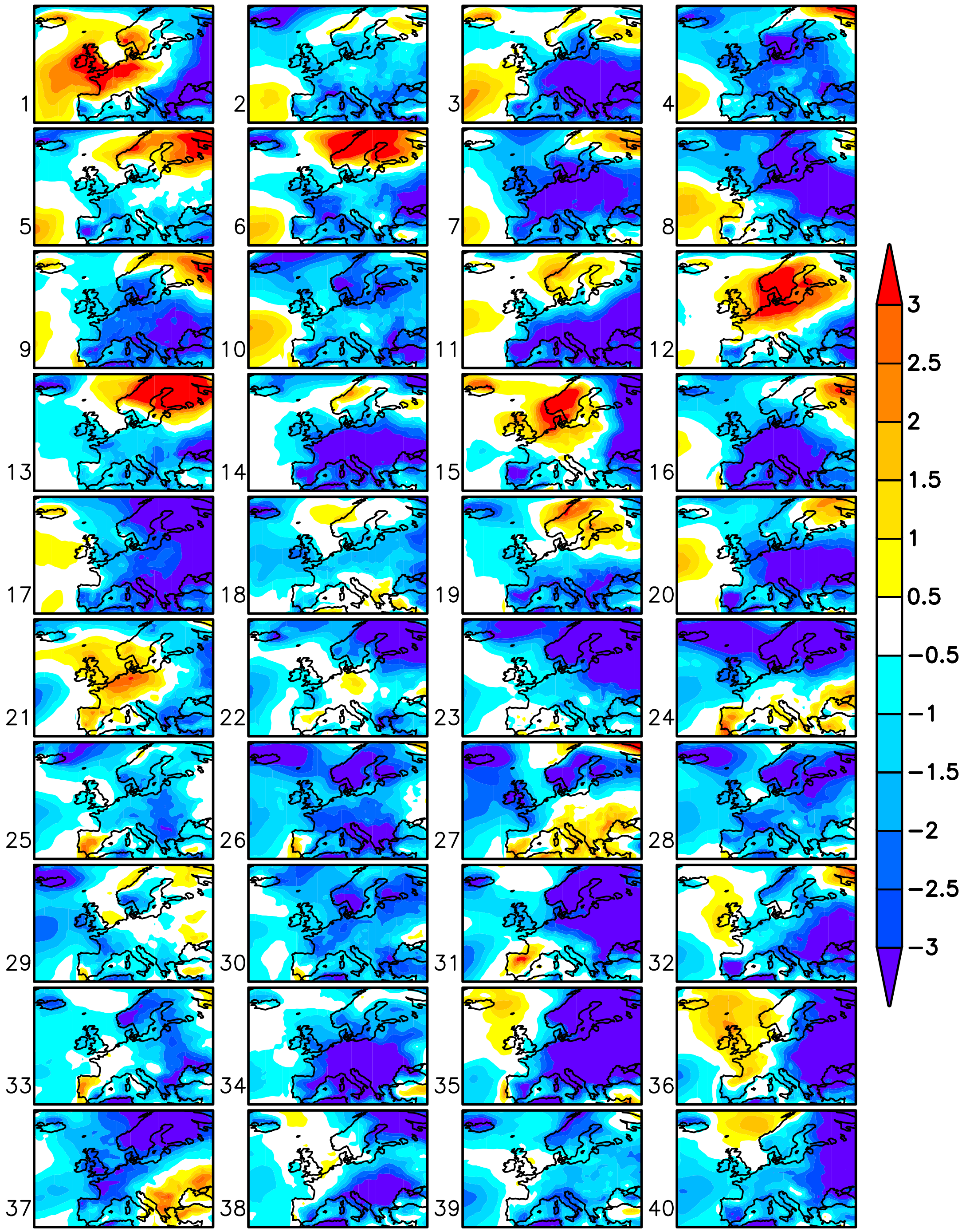

Figure 4.7 July 1783 European surface temperature anomalies (K) for individual Laki simulations. Each set of 10 simulations (i.e., 1-10, 11-20, 21-30, and 31-40) is initialized by perturbing a different set of initial conditions. Anomalies are calculated with respect to the five years before the eruption.

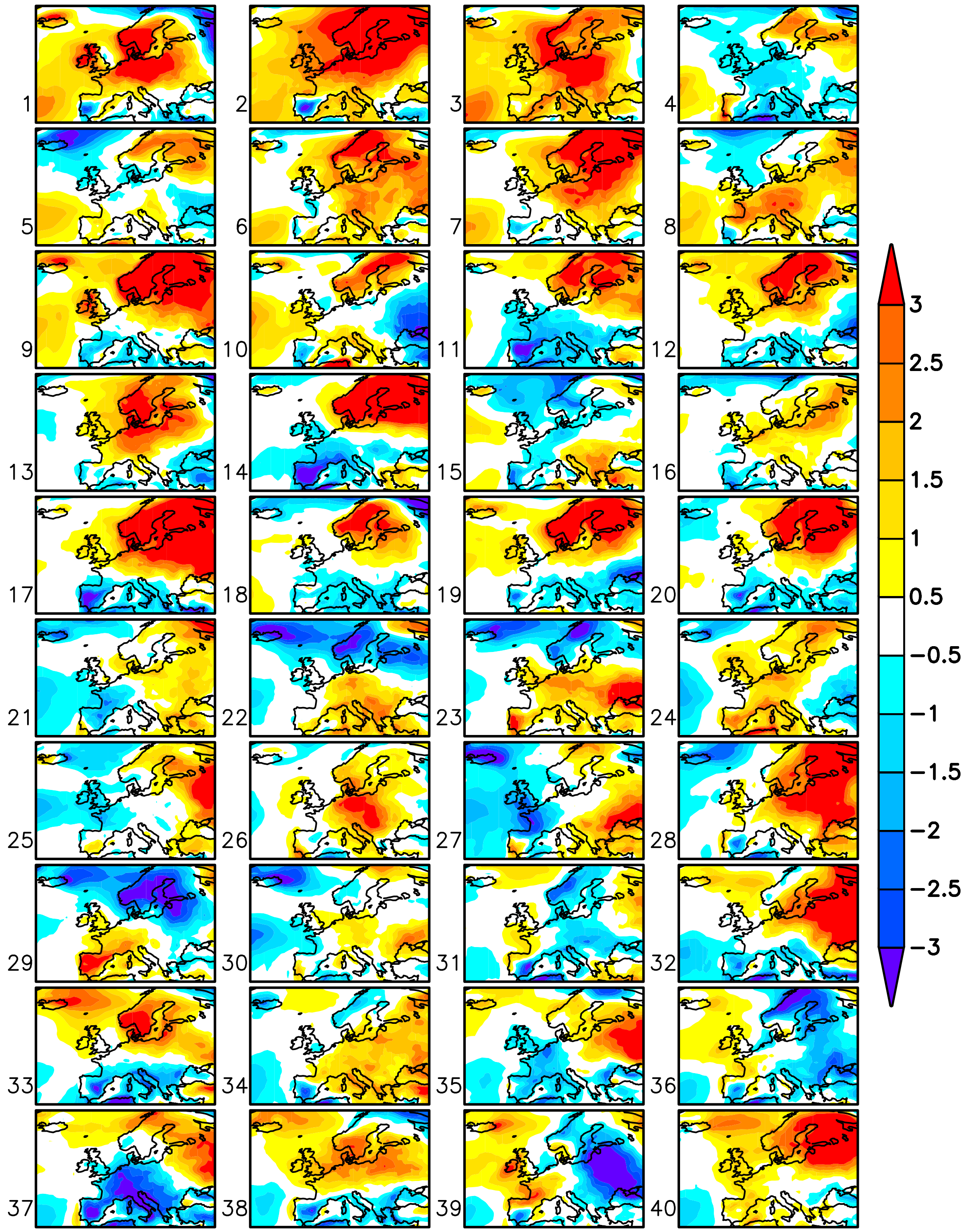

Figure 4.8 July 1783 European surface temperature anomalies (K) for individual noLaki simulations. Each set of 10 simulations (i.e., 1-10, 11-20, 21-30, and 31-40) is initialized by perturbing a different set of initial conditions. Anomalies are calculated with respect to the five years before the eruption.

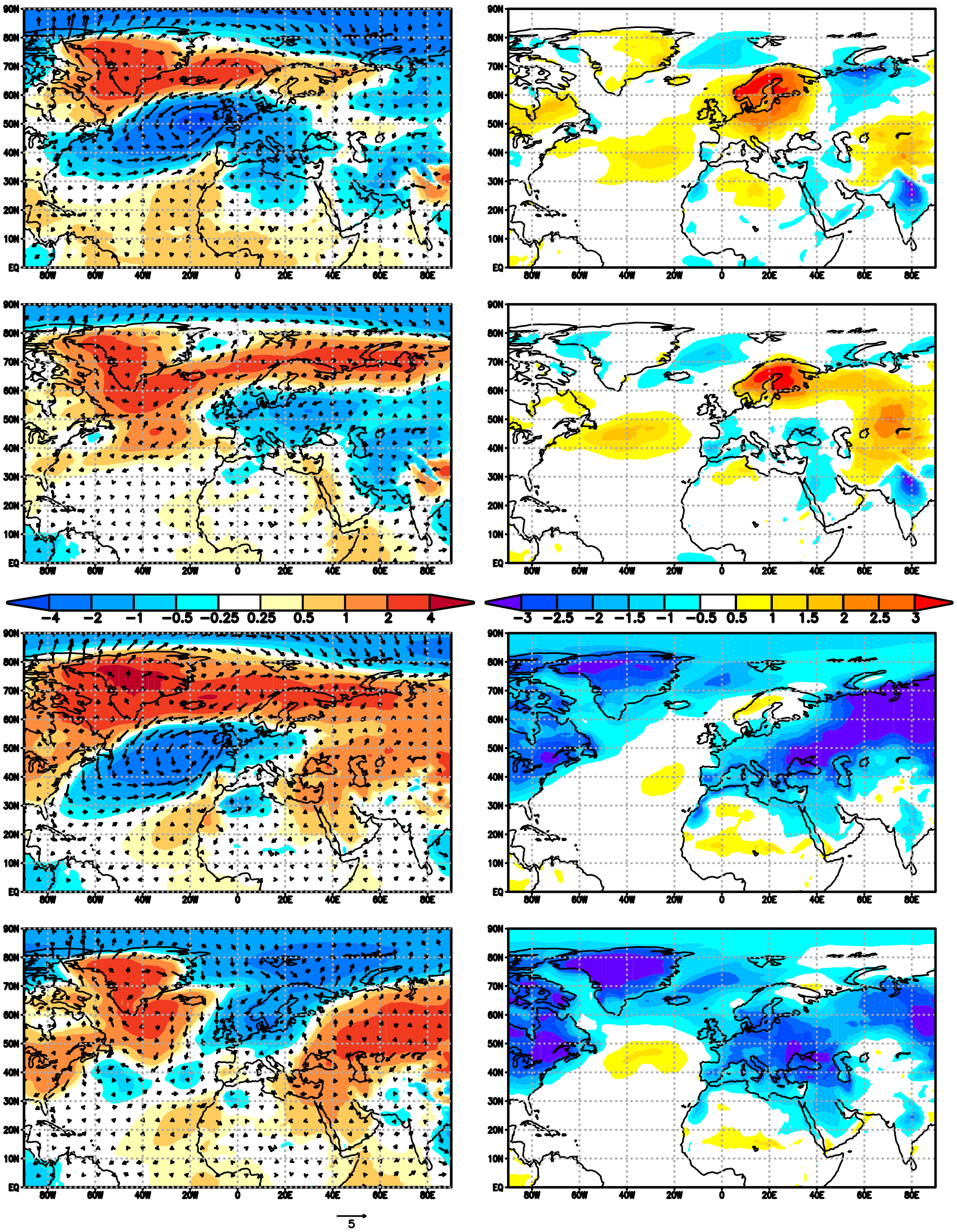

Figure 4.9 July 1783 sea level pressure anomalies (hPa) and surface wind anomalies (m/s, left) and surface air temperature anomalies (K, right) for averages of different simulations. From top to bottom: noLaki simulations with North Atlantic cyclone; noLaki simulations without North Atlantic cyclone; Laki simulations with North Atlantic cyclone; Laki simulations without North Atlantic cyclone.

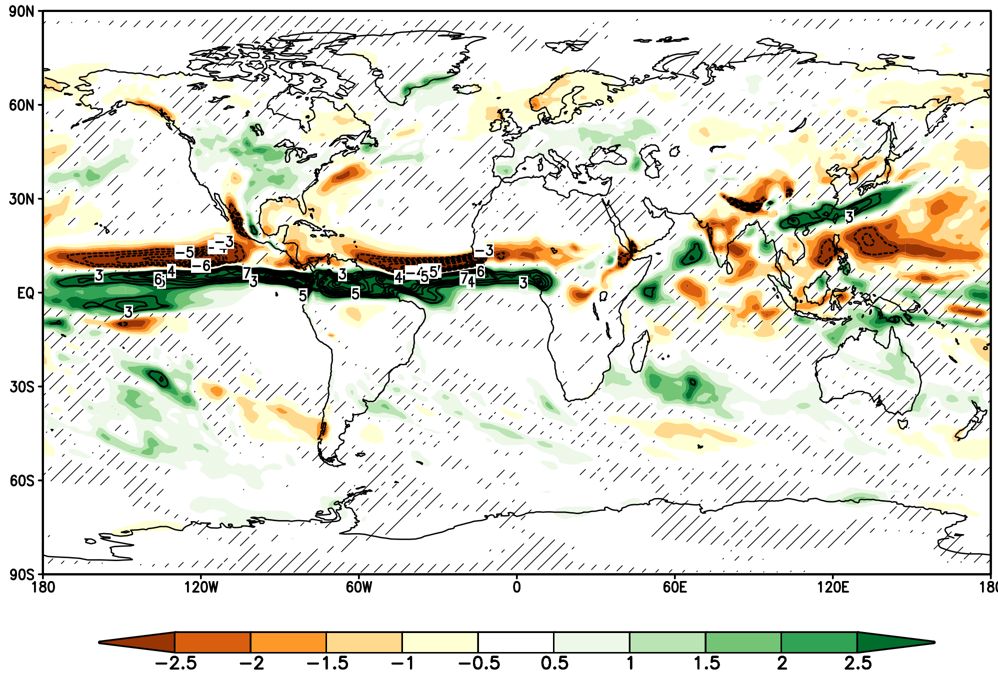

Figure 4.10 JJA 1783 precipitation anomalies (mm/d) for the Laki ensemble average. Anomalies are calculated with respect to the five years before the eruption. Hatching represents areas < 95% significance using a two-tailed Student's *t*-test.

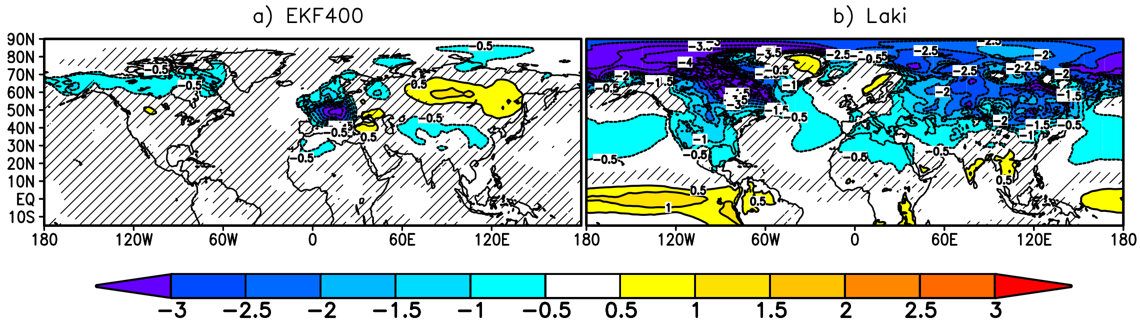

Figure 4.11 DJF 1783-1784 surface temperature anomalies (K) for (a) EKF400 reanalysis and (b) Laki ensemble average. Anomalies are calculated with respect to the five years before the eruption. Hatching represents areas < 95% significance using a two-tailed Student's *t*-test.

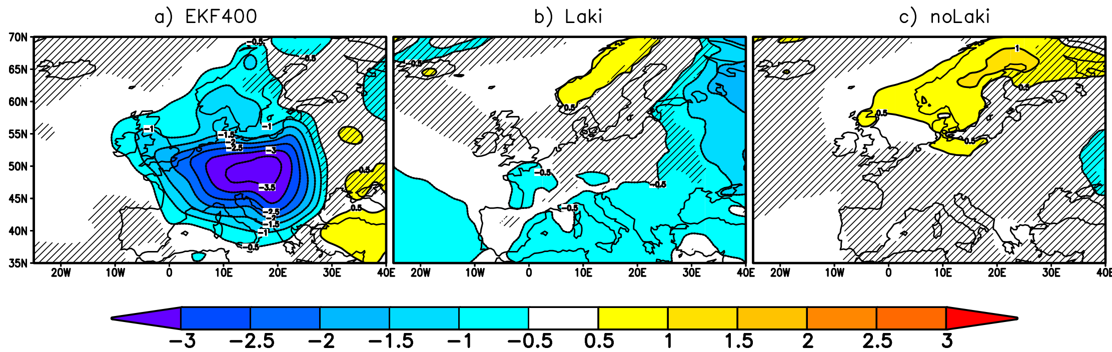

Figure 4.12 DJF 1783-1784 European surface temperature anomalies (K) for (a) EKF400 reanalysis, (b) Laki ensemble average, and (c) noLaki ensemble average. Anomalies are calculated with respect to the five years before the eruption. Hatching represents areas < 95% significance using a two-tailed Student's *t*-test.

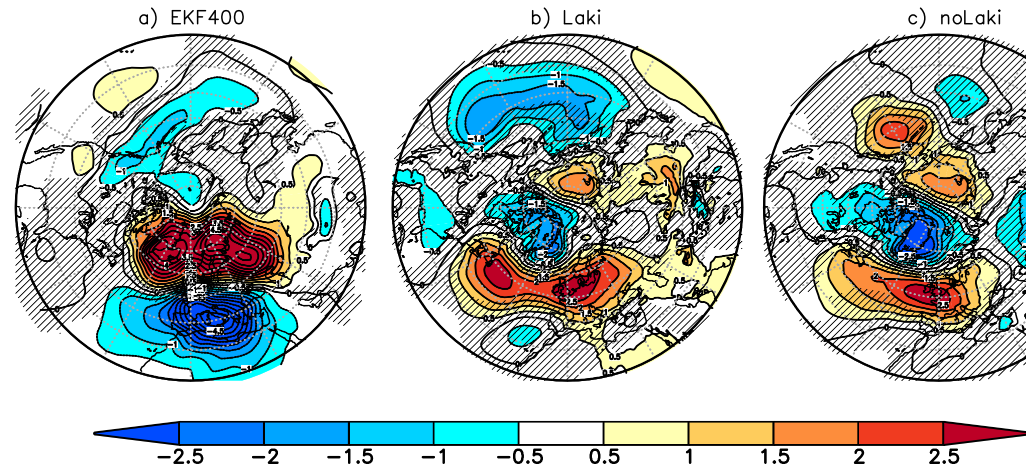

Figure 4.13 DJF 1783-1784 Northern Hemisphere sea level pressure anomalies (hPa) for (a) EKF400 reanalysis, (b) Laki ensemble average, and (c) noLaki ensemble average. Anomalies are calculated with respect to the five years before the eruption. Hatching represents areas < 95% significance using a two-tailed Student's *t*-test.

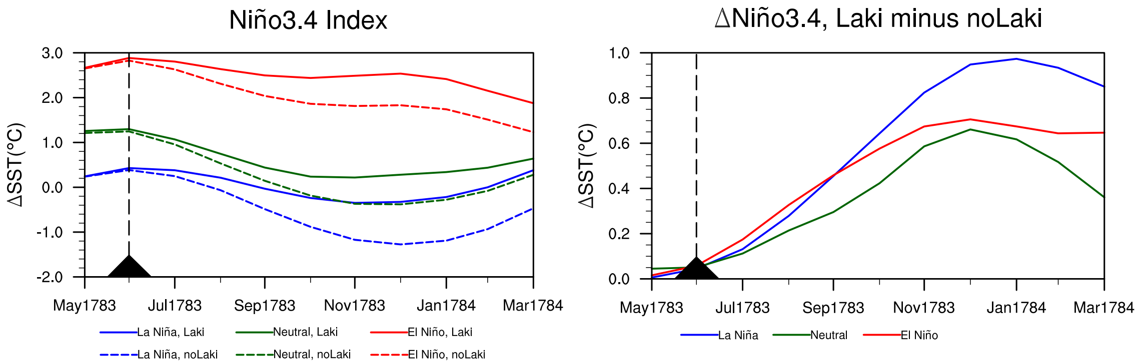

Figure 4.14 Left: Niño3.4 indices for the noLaki (dotted lines) and Laki (solid lines) ensembles for La Niña (blue), neutral (green), and El Niño initial conditions. Right: Laki minus noLaki Nino 3.4 indices for La Niña (blue), neutral (green), and El Niño initial conditions.